Impacts of Zonal Asymmetry on Southern Ocean Dynamics and Biogeochemistry

Thesis by
Lilian Aja Dove

In Partial Fulfillment of the Requirements for the
Degree of
Doctor of Philosophy

CALIFORNIA INSTITUTE OF TECHNOLOGY
Pasadena, California

2023
Defended May 22, 2023

Lilian Aja Dove
ORCID: 0000-0001-8346-0034

I may not reach the heights I seek,
My untried strength may fail me;
Or, half-way up the mountain peak
Fierce tempests may assail me.
But though that place I never gain,
Herein lies comfort for my pain—
I will be worthy of it.
Ella Wheeler Whilcox, 1888

"When we hit our lowest point, we are open to the greatest change."
Avatar Aang, *Legend of Korra*, Book 1, Episode 12

ACKNOWLEDGEMENTS

Mom and Dad: From day one, you have encouraged me to reach my goals and take up the space I deserve. Thank you for always believing in me and being my number one supporters.

Eva Dove, Patrick Yun, Maizie Dove-Yun, and Stella Dove-Yun: You gave me a home when I didn't have one and I wouldn't be finishing this degree without you. Thank you for always giving me unconditional love, comfort, and joy.

Deep Mukherji: You make me a better person and I am so lucky to get to share in your gentleness, humor, and passion. Thank you for putting up with my bad jokes, always being my safety net, and encouraging me to push boundaries.

Nimbus Dove: I had no idea how much I needed you until you arrived in my life. Thank you for grounding me, for giving me a purpose on days where getting out of bed was hard, and for always being unapologetically you.

Andy Thompson: I often wonder why you took the risk of working with a random woman who had never done physical oceanography before, but I'm very grateful you did. Thank you for your patience and generosity, for challenging me to test my limits, and for being a role model on how to be an educator, mentor, parent, and colleague all at once.

Jess Adkins, Ruby Fu, Michelle Gierach, and Alison Gray: Thank you for being on my thesis committee and for providing guidance on my science and career.

Bronagh Glaser, Julie Lee, Nora Oshima, Jen Shechet, Mauricio Villagran, and Julia Zuckerman: Everything I have done at Caltech would not have been possible without you. You've celebrated with me at my highs and supported me at my lows, and you have all gone above and beyond to make my work possible.

Sara Murphy and Clare Singer: Words cannot describe how unbelievably grateful I am to have been in a cohort with two of the most resilient, kind, and brilliant women I know. Both of you are angels in my life and if I had to do this all over again, I know I could do it because I had y'all by my side.

Ellen Robo: You are the best sounding board anyone could ask for. Our Sunday crosswords are a highlight of my week and I am so grateful that while our paths diverged, our connection grows stronger every year.

Harrison Parker: One way to build a really strong and really weird relationship with someone is to have a gossip session with them at 8 am, 5 days a week, for 5 years. I am beyond grateful to have shared every (EVERY) hurdle and celebration with you. Thank you for continually helping me become a better educator and for being married to the coolest person I know, Jackie Lopez Parker.

Reina Buenconsejo, Polina Khapikova, Ren Marquez, and Newton Nguyen: I learn something from every conversation and coffee we share. I am so grateful to have shared time with such thoughtful, giving, and funny people like each of you.

Mar Flexas: Thank you for always believing in me even when my belief in myself was nowhere to be found. You have made me a better scientist and person and you always take me seriously, even when I am convinced I don't deserve that grace. I am extremely lucky to have you in my life.

Hannah Allen, Zach Erickson, Kelsey Moore, Giuliana Viglione, and Earle Wilson: Thank you for being the additional big siblings I never knew I needed. Each of you is such a force for good in my life and all I can hope is that I can be as much of a guiding light to others as you have been for me.

Freya Morris and Cullen Quine: Y'all are a delight to come home to. Avocado House, Pancake House, Cat House - whatever we are, I'm glad it was with you.

Bailey Armos, Mike Kovatch, Gabe Matthias, Isa Rosso, Natalie Swaim, and Sidney Wayne: I have been beyond lucky to sail (or almost sail) with each of you and I am grateful for the humor and good company on each night shift (and day of stranding in Cabo Verde). What an honor it is to not only have the best job in the world but to get to do it with the best people.

Taylor Cason and Ellie Flint: Getting to be your mentor was such a blessing and I am so proud of the scientists you are! Thank you for working with me and for being willing to go on coding deep dives, especially when I didn't know what I was doing.

Kate Farris, Jacqui Liu, Allen Park, and Juju Wang: It's beyond amazing to have a group of friends that I can rely on for anything despite living across the country. Thank you for the laughs, puzzles, and spontaneity.

Haroula Baliaka, Kat Ball, Sophia Charan, Danielle Draper, Josh Laughner, Ben Schulze, Ariana Tribby, Ryan Ward, and Maria Yu: Thank you for having always accepted me as one of the atmospheric chemists. I appreciate every coffee run, lunchtime conversation, and hot take.

And to the locations that have given me comfort in the last five years: 85C Bakery, Float Coffee Shop, Pasadena Public Libraries, Philz Coffee, Tea Spots, Vroman's Bookstore, the RVIB *Nathaniel B. Palmer*, and the RV *Roger Revelle*.

ABSTRACT

The Southern Ocean is a key region for the ventilation and formation of intermediate and deep water masses. Interactions of the Southern Ocean's Antarctic Circumpolar Current (ACC) with bathymetry can result in the diversion and compaction of frontal currents, resulting in standing meanders associated with enhanced mesoscale eddy kinetic energy (EKE) and submesoscale vertical velocities. As a result, standing meanders are thought to shape uptake and sequestration of heat and carbon across the ACC. In this thesis, I use observations from remote sensing and various autonomous underwater vehicles to investigate how physical mechanisms, from the submesoscale to the basin scale, shape the biogeochemical properties and tracer distributions of the Southern Ocean.

Processes at the ocean's submesoscale can play a vital role in exchanging water across the base of the mixed layer, contributing to water mass ventilation. Data from over 20,000 profiles from biogeochemical-Argo floats across the ACC highlight that the high EKE regions associated with standing meanders have relatively reduced apparent oxygen utilization (AOU) values below the base of the mixed layer. This result, as well as larger AOU variance in deep potential density classes, suggests there is enhanced ventilation occurring in standing meanders. Further investigation suggests the observed increased ventilation is due to both along-isopycnal stirring and enhanced exchange across the base of the mixed layer by vertical velocities at the submesoscale, highlighting the importance of standing meanders in shaping temporal and spatial variability of biogeochemical cycles and air-sea exchange.

Observations with horizontal scales of 2-4 kilometers in the standing meander associated with Crozet Plateau show that submesoscale processes are indeed ubiquitous. In this region, processes on the submesoscale to mesoscale spectrum play a role in enhancing surface frontal gradients and heightening tracer variability at depth. A separate field program provided novel observations at the submesoscale in Drake Passage during wintertime. The Polar Front, one of the major fronts of the ACC, is shown to be eddy-suppressing, suggesting that along-isopycnal submesoscale processes contribute to ventilation at the front. These spatial variations in stratification may additionally impact carbon fluxes between the atmosphere, surface mixed layer, and interior ocean. This thesis presents evidence that ventilation is a heterogeneous process across the Southern Ocean, with contributions from processes at physical scales that are undersampled by current observational programs.

PUBLISHED CONTENT AND CONTRIBUTIONS

Balwada, D., Gray, A. R., Dove, L. A., & Thompson, A. F. (in revision). Tracer stirring and variability in the Antarctic Circumpolar Current near the Southwest Indian Ridge. *Journal of Geophysical Research: Oceans*. doi: 10.22541/essoar.167839945.50522830/v1.

L.A.D. quality controlled the data and contributed to data analysis.

Thompson, A. F., Dove, L. A., Flint, E., Lacour, L. & Boyd P. W. (in review). Interactions between multiple physical particle injection pumps in the Southern Ocean. *Global Biogeochemical Cycles*. doi: 10.22541/essoar.168057558.87192564/v1.

L.A.D. assisted in data collection, quality controlled the data, and contributed to data analysis.

Erickson, Z. K., Fields, E., Johnson, L., Thompson, A. F., Dove, L. A., D'Asaro, E. A., & Siegel, D. A. (in review). Eddy tracking from in situ and satellite observations. *Journal of Geophysical Research: Oceans*. doi: 10.22541/essoar.167979672.22588418/v1.

L.A.D. contributed to data analysis.

Swart, S., du Plessis, M. D., Nicholson, S. A., Monteiro, P. M. S., Dove, L. A., Thomalla, S., Thompson, A. F., Biddle, L. C., Edholm, J. M., Giddy, I., Heywood, K. J., Lee, C., Mahadevan, A., Shilling, G. & Buss de Souza, R. (2023). The Southern Ocean mixed layer and its boundary fluxes: Finescale observational progress and future research priorities. *Philosophical Transactions of the Royal Society A*. doi: 10.1098/rsta.2022.0058.

L.A.D. contributed to writing section 3.

Dove, L. A., Viglione, G.A., Thompson, A.F., Flexas, M. M., Cason, T. R., & Sprintall, J. (2023). Controls on wintertime ventilation in southern Drake Passage. *Geophysical Research Letters* 50.5. doi: 10.1029/2022GL102550.

L.A.D. contributed to data analysis and to writing the manuscript.

Dove, L. A., Balwada, D., Thompson, A. F., & Gray, A. R. (2022). Enhanced ventilation in energetic regions of the Antarctic Circumpolar Current. *Geophysical Research Letters* 49.13. doi: 10.1029/2021GL097574.

L.A.D. conceived the project, quality controlled and analyzed the data, and wrote the manuscript.

Dove, L. A., Thompson, A. F., Balwada, D., & Gray, A. R. (2021). Observational evidence of ventilation hotspots in the Southern Ocean. *Journal of Geophysical Research: Oceans* 126.7. doi: 10.1029/2021JC017178.

L.A.D. assisted in data collection, quality controlled and analyzed the data, and wrote the manuscript.

TABLE OF CONTENTS

LIST OF ILLUSTRATIONS

Chapter 1

INTRODUCTION

1.1 Motivation

The ocean is one of the primary sinks of carbon dioxide released through human activities such as fossil fuel burning and cement production. On yearly and decadal timescales, the ocean absorbs roughly one quarter of anthropogenic carbon dioxide emissions, regulating the rise of carbon dioxide in the atmosphere (Friedlingstein et al., 2022). Observing and quantifying how carbon and other tracers exchange between the atmosphere, surface ocean, and interior ocean, where properties can be sequestered long-term, is necessary for constraining Earth's carbon budget. Approaching this question requires an understanding of the intricate interactions between fluid dynamics and biogeochemistry of the ocean.

The Southern Ocean surrounds the Antarctic continent and exerts a strong leverage on Earth's climate as the primary site of both deep water ventilation at the ocean surface and subduction of newly formed intermediate water masses (Talley, 2013). The circulation of the Southern Ocean is dominated by the mostly unobstructed eastward flow of the Antarctic Circumpolar Current (ACC). Isopycnals, or surfaces of constant density, of the ACC tilt upwards towards the Antarctic continent, allowing for the adiabatic upwelling of Circumpolar Deep Water that has been sequestered from the surface for O(100-1000 years). At the surface, these old waters exchange heat and gases with the atmosphere, outgassing natural carbon stocks and acting as a sink for anthropogenic CO_2 (Gruber et al., 2019; Landschützer et al., 2015; Sallée et al., 2012). The adiabatic ventilation of deep waters allows the Southern Ocean to have an outsized impact on the climate; despite making up approximately 30% of the surface area of the global ocean, the Southern Ocean south of 30°S has taken up 40% of anthropogenic carbon (Gruber et al., 2019).

Despite its importance, the Southern Ocean remains undersampled and fluxes of climatologically-important tracers such as heat and CO_2 remain underconstrained. Observations in the Southern Ocean have historically been both spatially and temporally sparse, contributing to disagreements between carbon uptake estimates in models and observations (Gruber et al., 2019), a lack of documentation of tracer distributions across the ACC, and limitations in attribution to specific processes

that explain these discrepancies. Recent work by the Southern Ocean Carbon and Climate Observations and Modeling program (SOCCOM, Claustre et al., 2020), the Southern Ocean Observing System program (SOOS, Rintoul et al., 2012), Southern Ocean Time Series mooring (SOTS, Shadwick et al., 2015; Trull et al., 2019), and several other sustained projects have resulted in increased coverage of the Southern Ocean. The combination of increased observations (*in situ* and satellite) and numerical models is necessary to close budgets and develop a fundamental understanding of the coupled dynamical and biogeochemical processes in the Southern Ocean.

1.2 Beyond a Zonally Symmetric Framework of the Southern Ocean

Traditionally, a zonal-mean framework has been employed to describe the circulation and resulting tracer distributions and ventilation across the Southern Ocean (Marshall and Speer, 2012; Morrison et al., 2022). However, this framework presents limitations in describing how localized dynamical processes may impact tracer distributions and air-sea exchange of biogeochemical tracers.

At its largest scales, the ACC is comprised of a series of eastward-flowing frontal jets that are typically efficient water mass barriers (Figure 1.1; Chapman et al., 2020; Orsi et al., 1995; Sokolov and Rintoul, 2009). These frontal flows are accompanied by strongly tilting density surfaces in thermal wind balance that sustain a vigorous mesoscale eddy field (Rintoul and Naveira Garabato, 2013). Standing meanders of fronts form in the ACC where these jets interact with major bathymetric features, such as plateaus (*e.g.*, Kerguelen Plateau) and rises (*e.g.*, the East Pacific Rise). In these locations, standing meanders form when fronts are diverted northward to preserve potential vorticity as a result of the shoaling topography (Rintoul, 2018; Thompson and Naveira Garabato, 2014; Yung et al., 2022). These flow-topography interactions can cause transport barriers to become "leaky" (Dufour et al., 2015; Naveira Garabato et al., 2011) as well as enhance eddy kinetic energy (EKE; Gille and Kelly, 1996; Lu and Speer, 2010; Witter and Chelton, 1998), vertical momentum transport (Thompson and Naveira Garabato, 2014), lateral tracer transport (Abernathey and Cessi, 2014; Dufour et al., 2015; Roach et al., 2016; Thompson and Sallée, 2012), upwelling (Brady et al., 2021; Tamsitt et al., 2017; Viglione and Thompson, 2016), and subduction (Bachman and Klocker, 2020; Llort et al., 2018).

ACC standing meanders are characterized by enhanced EKE and strain rates due to persistent conditions favorable for baroclinic and barotropic instabilities (Lu et al., 2016; Youngs et al., 2017). The imprint of coherent eddies on tracer structure, for

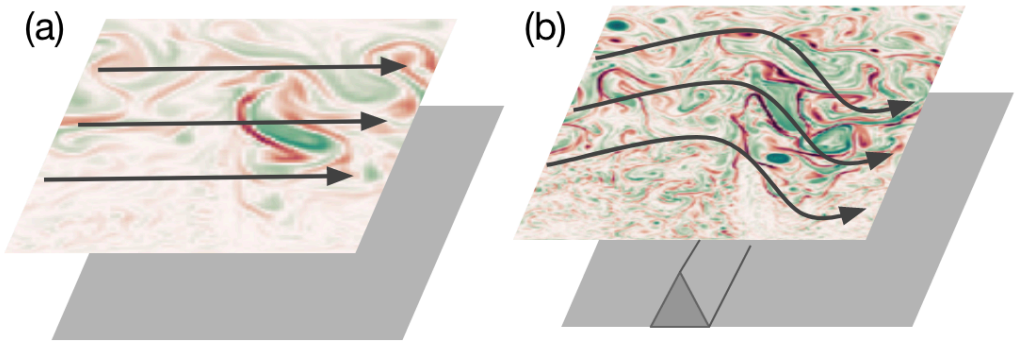

Figure 1.1: Schematic of surface vorticity given two bathymetric cases.

Surface relative vorticity and stylized bathymetry in cases with (a) flat bathymetry (b) a bathymetric ridge. Gray arrows represent the mean flow of the ACC fronts. Surface vorticity data taken from Balwada, Xiao, et al., 2021, with vorticity normalized by the Coriolis frequency.

example, surface chlorophyll, occurs over horizontal scales of O(100 km) (Figure 1.2a,b). These eddies typically have a vertical extent of O(2,000 m) and stir tracers below the mixed layer in the interior (Balwada, LaCasce, et al., 2021; Balwada et al., 2016). In the Southern Ocean, where the background ispoycnals are tilted to depth towards the equator, stirring along isopycnals enhanced by mesoscale eddies can provide a pathway for transporting tracers across the pycnocline (Uchida et al., 2019).

Near the surface, mesoscale eddies have an inlay of submesoscale O(1–10 km, 1 h-10 days) currents, which are often visible as cusps and filaments in surface tracers (Figure 1.2c,d). Unlike the geostrophically balanced mesoscale, submesoscale processes are characterized by Rossby numbers of O(1), dynamical regimes where rotation and inertial forces are of comparable importance. These smaller-scale motions are energized by the production of surface buoyancy gradients through mesoscale frontogenesis (Adams et al., 2017; Klein and Lapeyre, 2009) and by the formation of submesoscale eddies through mixed layer baroclinic instabilities (Boccaletti et al., 2007) or through wind-front interactions (Thomas et al., 2008) that give rise to large mixed layer lateral density gradients. Submesoscale currents are generally associated with elevated vertical velocities and restratification tendencies in the mixed layer (McWilliams, 2016; Su et al., 2018; Taylor and Thompson, 2023), altering the upper-ocean stratification and exchange between the mixed layer and the thermocline (Archer et al., 2020; Klein and Lapeyre, 2009). Strong vertical

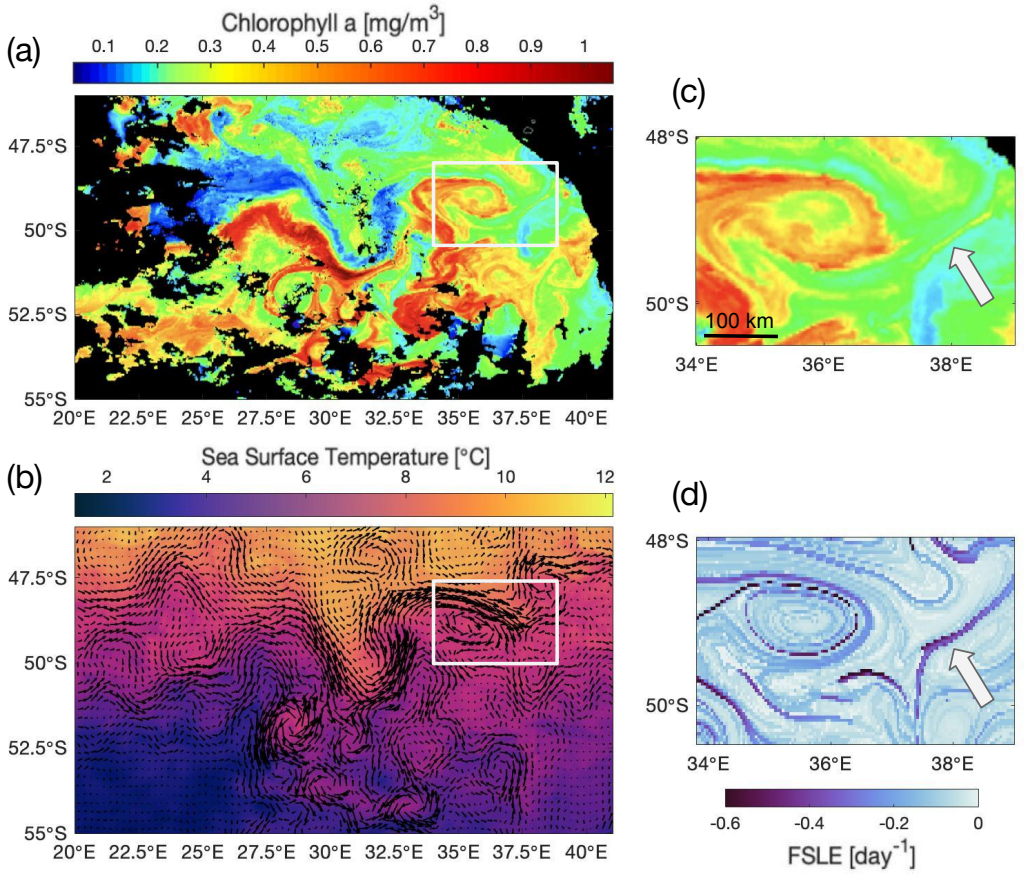

Figure 1.2: Physical scales of variability in a standing meander.

(a) Chlorophyll-a (ocean color, [mg m^{-3}]) on December 30, 2018 from Terra/Aqua-MODIS. Regions covered by clouds are colored black. The white dotted line designates the track of GO-SHIP I06S cruise and the white box denotes the region in (c) and (d). (b) Sea surface temperature [°C] on December 30, 2018 with geostrophic velocity vectors. (c) Detail of panel (a) with white arrow pointing towards a submesoscale filament. (d) Finite size Lyapunov exponent (FSLE; [$days^{-1}$]) for the boxed region in (a). White arrow points towards the same filament in (c). FSLE acts as a proxy for strain and identifies the direction of horizontal stretching.

velocities may penetrate up to a few 100 m below the base of mixed layer (Siegelman et al., 2020), playing a role in transporting material across the base of the mixed layer and connecting the surface ocean to the mesoscale-dominated interior.

1.3 Heterogeneous Ventilation and Carbon Export

The vertical transport of tracers is crucial for the production and export of organic carbon, ventilation of the subsurface ocean, and modulation of air-sea exchange (Abernathey and Ferreira, 2015; Bachman and Klocker, 2020; Balwada, Xiao,

et al., 2021; Freilich and Mahadevan, 2021). The enhancement of mesoscale and submesoscale processes in standing meanders of the ACC result in enhanced capacity for submesoscale transport of tracers across the base of the mixed layer (Balwada et al., 2018; Lévy et al., 2018; Uchida et al., 2020) and can have an outsized impact on ventilation (Naveira Garabato et al., 2011; Rintoul, 2018; Tamsitt et al., 2016; Viglione et al., 2018). Standing meanders have also been identified as regions where old CDW waters enriched in dissolved inorganic carbon are preferentially transported to the surface ocean (Brady et al., 2021; Tamsitt et al., 2017), which can potentially create localized regions of enhanced air-sea gas exchange.

In addition to dissolved tracers, enhanced vertical exchange can also impact particulate tracers, such as particulate organic matter (POC). Export production, the flux of net primary production across the base of the ocean's euphotic zone, is a critical step for the sequestration of carbon from the atmosphere into the deep ocean (Buesseler and Boyd, 2009; Lévy et al., 2013). Observations collected over the past decade provide convincing evidence that the vertical carbon flux associated with gravitational sinking of organic matter alone is insufficient to close the carbon budget (Boyd et al., 2019; Lévy et al., 2013; Schlitzer, 2002). At least regionally, physical processes that advect and stir surface properties to depth make a non-negligible contribution to the biological pump (Boyd et al., 2019; Buesseler and Boyd, 2009; Lévy et al., 2012). Ecological processes (*e.g.*, diel migration) and physical processes (*e.g.*, mixed layer depth variability and motions realated to lateral buoyancy gradients) have both been highlighted as potential mechanisms for enhancing carbon export fluxes. How processes on the submesoscale-mesoscale spectrum contribute to export production is an active direction of investigation through field campaigns (Ruiz et al., 2019; Siegel et al., 2023) and numerical modeling (Mahadevan and Tandon, 2006; Taylor, 2018).

Non-gravitational carbon export can occur via subduction processes at frontal zones due to along-isopyncal stirring along sloped isopycnals (Uchida et al., 2019) and strong vertical velocities associated with lateral density gradients (Klein and Lapeyre, 2009). The energetic eddy field, generally reduced pycnocline stratification, and large phytoplankton blooms precondition the Southern Ocean to export from submesoscale processes (Llort et al., 2018; Omand et al., 2015).

1.4 Observations from Autonomous Vehicles and Satellites

Seagliders

The complexity and small spatial scale of submesoscale motions are not only a challenge for numerical models, but also pose a challenge for observational oceanography (Heywood et al., 2014). Processes on scales of O(1-10 km) are not amenable to study by ship or moorings. Seagliders, hereafter gliders, are autonomous underwater vehicles with low power consumption that allows for months-long, high-resolution sampling (Eriksen et al., 2001; Rudnick and Cole, 2011; Rudnick et al., 2004).

Glider motion is controlled by a buoyancy bladder, which controls the instrument's depth in the water column; a rudder and wings, which control its horizontal movement; and a battery, which acts as an adjustable ballast to control the the vehicle's attitude. Data is typically transmitted back to a ground-based basestation through the Iridium satellite constellation each time the glider surfaces. Gliders can dive up to 1000 meters following a V-shaped pathway. A typical dive to 1000 meters takes approximately 4 hours, with the horizontal distance covered depending on the strength of the background flow and the desired position of the next surfacing.

Gliders can carry a range of sensors to detect physical and biogeochemical tracers. Standard sensors on glider datasets present in this thesis include temperature, salinity, dissolved oxygen, chlorophyll fluorescence, and optical backscatter. Optical backscatter is a measure of suspended particle concentrations in the water column and can be measured at different wavelengths. Optical backscatter sensors consist of an infrared light-emitting diode and a photodetector. Light is emitted by the diode and scattered back to the photodiode by particles in the water, producing a voltage response in the sensor.

Biogeochemical-Argo floats

Argo floats are another form of autonomous underwater vehicle that have greatly expanded the available tracer distribution of temperature and salinity data across the global ocean in the last 25 years (Riser et al., 2016). More recently, Biogeochemical-Argo (BGC-Argo) floats have expanded the available tracers beyond the traditional physical oceanic tracers and into biogeochemical properties. The SOCCOM program has played a vital role in increasing the BGC-Argo population of the Southern Ocean (Claustre et al., 2020; Johnson et al., 2017), deploying over 150 BGC-Argo floats south of 30°S since 2015.

BGC-Argo floats are battery-powered and dive and surface by changing their buoy-

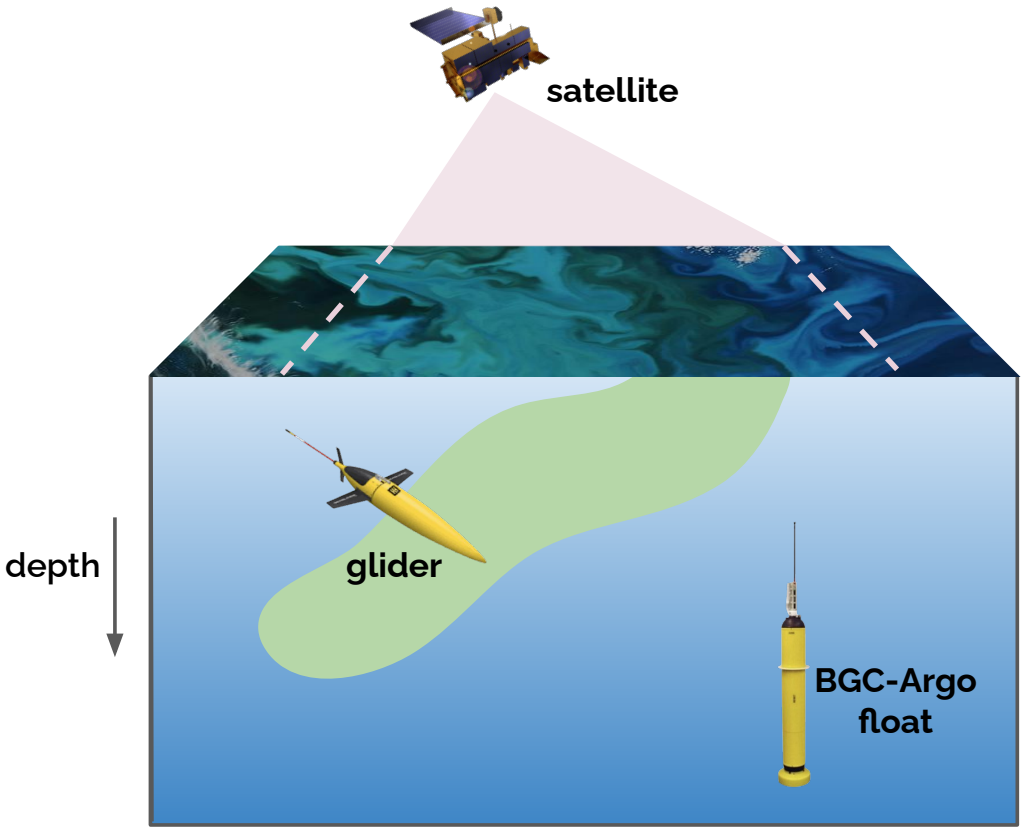

Figure 1.3: Schematic of instrumentation

ancy using a buoyancy bladder, like gliders. A typical float cycle has the vehicle descending to 1000 meters depth and drifting for 10 days, then diving to 2000 m before returning to the surface. As the floats ascend, they collect data which they transmit via Iridium communications satellites. Unlike a glider, BGC-Argo floats are quasi-Lagrangian, meaning they travel with the prevailing current at 1000 meters and cannot be piloted in a desired direction. The lifetime of a BGC-Argo float is 3-5 years. BGC-Argo floats measure the same tracers as gliders (temperature, salinity, dissolved oxygen, chlorophyll fluorescence, and optical backscatter) and fully-instrumented floats can also measure pH and nitrate.

Satellite altimetry

Remote sensing by satellites provides daily estimates of sea surface height (SSH). SSH is composed of both sea level anomaly (SLA), the time-varying aspect of SSH, absolute dynamic topography (ADT), the sum of the time-mean dynamic topography and the time-varying SLA. Using SLA and assuming geostrophic balance allows for

the calculation of zonal and meridional geostrophic velocities. Eddy kinetic energy (EKE) can be calculated as EKE= $\frac{1}{2}\sqrt{\overline{u'^2} + \overline{v'^2}}$, where u' and v' are the zonal and meridional eddy geostrophic velocities estimated from the time-varying sea surface height (SSH) anomaly field, and $\overline{(.)}$ represents a time average.

Finite-size Lyapunov Exponents (FSLE)

FSLEs describe the orientation and timescale of strain fields by quantifying stretching and compression (d'Ovidio et al., 2004; d'Ovidio et al., 2010) and are calculated from SSH-derived mesoscale flow fields. They are a Lagrangian diagnostic, and for a given flow field are defined as the separation growth rate for particle pairs, $\lambda(d_0, d_f) = \frac{1}{\tau} log(\frac{d_f}{d_0})$, where d_0 and d_f are the initial and final separation distances and τ is the first time where separation distance d_f is reached.

Recent publications demonstrate that maximum stretching FSLEs have an empirical relationship to the magnitude of lateral density gradients (Siegelman et al., 2020). Specifically, density anomalies are physically aligned with FSLEs, so larger magnitude FSLEs are correlated with stronger lateral density gradients. While measuring lateral density gradients can be achieved with high temporal and spatial resolution measurements, such observations are sparse in the Southern Ocean. Therefore, FSLEs provide a useful proxy to visualize surface frontogenesis. Additionally, Siegelman et al., 2020 demonstrated that the relationship between FSLEs and lateral density gradients may extend below the mixed layer in the Southern Ocean, particularly in energetic regions.

1.5 Impact

This thesis focuses on zonal asymmetries of the Southern Ocean and how they influence the distribution and fluxes of physical and biogeochemical oceanic tracers. A unifying theme between the individual chapters is ventilation, which is considered as any process, or combination of processes, that transfers surface waters and tracers into the pycnocline, *à la* Morrison et al., 2022. Through ventilation processes, the ocean can transport tracers between the surface and interior ocean, impacting tracer budgets of climatological importance like heat and carbon.

Through observations with *in situ* and remote sensing data, ventilation is shown to be shaped by the EKE distribution of the surface ocean. Standing meanders of the ACC, resulting from flow-topography interactions, have physical and biogeochemical signatures of recent ventilation at depths below the standing pycnocline (Chapter

II). The mechanisms that lead to this ventilation are difficult to observe, particularly with semi-Lagrangian BGC-Argo floats that sample every 10 days and may miss submesoscale features.

Chapter III reveals that as compared to more quiescent regions, standing meanders have enhanced submesoscale frontal gradients corresponding to the heightened tracer variability at depth. In addition, vertical tracer gradients across the pycnocline are reduced in the standing meander, illustrating enhanced ventilation. While ventilation processes are not directly observed, the observations are consistent with numerical studies that highlight standing meanders as hotspots for ventilation through enhanced mesoscale stirring and submesoscale vertical velocities. The range of physical processes are underobserved by a BGC-Argo float but captured by gliders, suggesting that submesoscale processes that shape ventilation are not fully captured by current observational systems.

Within regions of high EKE, there can be heterogeneity of ventilation as well. Chapter IV describes how within Drake Passage, ventilation is localized to the Polar Front despite strong surface wind and buoyancy forcing across the whole region. Glider data once again points to the role of submesoscale processes in contributing to ventilation, with a non-local process, sea ice melt, shaping where these motions occur. Waters penetrating to depth primarily along isopycnals demonstrate that exchange at localized fronts can dominate larger-scale tracer fluxes. The preliminary work described in Chapter V outlines how these spatial variations in stratification may result in variability beyond ocean-internal ventilation and impact air-sea fluxes of carbon.

Overall, this work emphasizes the need to account for spatial heterogeneity in physical processes influencing carbon export, air-sea exchange, and biogeochemical cycling in the Southern Ocean. Ventilation is likely a result of coupling of motions across scales. Submesoscale motions play the essential role of efficiently carrying surface properties, including organic carbon, across the base of the mixed layer. After this, stirring along isopycnals, by the same eddies that create the surface density gradients, enhances the transfer of these surface properties to depth. Thus, observations across the full mesoscale-submesoscale spectrum are necessary to capture ventilation, highlighting the need for adaptive observing strategies to constrain Southern Ocean heat and carbon budgets in ongoing and future observational systems. In addition, combining high-resolution observations with numerical modeling will further our understanding of ocean ventilation.

Chapter 2

STANDING MEANDERS AS VENTILATION HOTSPOTS

This work is published in *Geophysical Research Letters* as "Enhanced Ventilation in Energetic Regions of the Antarctic Circumpolar Current." (Dove et al., 2022).

2.1 Abstract

Flow-topography interactions along the path of the Antarctic Circumpolar Current (ACC) generate standing meanders, create regions of enhanced eddy kinetic energy (EKE), and modify frontal structure. We consider the impact of standing meanders on ventilation based on oxygen measurements from Argo floats and the patterns of apparent oxygen utilization (AOU). Regions of high-EKE have relatively reduced AOU values at depths 200-700 meters below the base of the mixed layer and larger AOU variance, suggesting enhanced ventilation due to both along-isopycnal stirring and enhanced exchange across the base of the mixed layer. Vertical exchange is inferred from finite-size Lyapunov exponents, a proxy for the magnitude of surface lateral density gradients, which suggest that submesoscale vertical velocities may contribute to ventilation. The shaping of ventilation by standing meanders has implications for the temporal and spatial variability of air-sea exchange.

2.2 Introduction

The Southern Ocean is a key region for the ventilation and formation of intermediate and deep water masses. Tilted density surfaces associated with the Antarctic Circumpolar Current (ACC) allow for the adiabatic upwelling of Circumpolar Deep Water (CDW) that has been sequestered from the surface for O(100-1000 years). At the surface, CDW exchanges heat and gases with the atmosphere, outgassing natural carbon stocks and acting as a sink for anthropogenic CO_2 (Gruber et al., 2019; Landschützer et al., 2015). Numerical models suggest that ventilation is spatially heterogeneous within the ACC (Tamsitt et al., 2017; Viglione and Thompson, 2016). Interactions of the ACC with underwater topography can result in the diversion and compaction of frontal currents, creating standing meanders (Sokolov and Rintoul, 2007) associated with enhanced mesoscale eddy kinetic energy (EKE; Figure 2.1a,b; Gille and Kelly, 1996). The ACC's major standing meanders are present at the Kergeulen Plateau, Campbell Plateau, Eastern Pacific Rise, Crozet Plateau,

and Drake Passage; these regions are thought to shape uptake and sequestration of heat and carbon (Brady et al., 2021; Klocker, 2018; Roach et al., 2016; Sallée et al., 2012).

Ventilation in the ACC depends on the local density structure as well as advection and stirring along isopycnals, and thus responds to a variety of processes and scales. Standing meanders lead to sloped isopycnals that store available potential energy (Bischoff and Thompson, 2014; Chapman et al., 2015; Klocker, 2018), which is released by baroclinic instability, producing a rich mesoscale $O(100\text{ km})$ eddy field approximately 100 km downstream of the standing meander (Rintoul, 2018; Thompson and Naveira Garabato, 2014). These eddies then stir and strain the surface density field, leading to frontogenesis and influencing submesoscale motions (Bachman and Klocker, 2020; Balwada et al., 2018; Klein and Lapeyre, 2009; Rosso et al., 2015). Through both lateral (Abernathey et al., 2013; Roach et al., 2016) and vertical (Adams et al., 2017; Klein and Lapeyre, 2009) motions, mesoscale and submesoscale eddies contribute significantly to ventilation in the ACC. Throughout this work, we refer to “ventilation" as any process or combination of processes that work to transfer surface waters and tracers into the pycnocline, which as described above, can occur on a variety of temporal and spatial scales (Morrison et al., 2022). Additionally, stirring refers to the advection of tracers by an eddying velocity field, while mixing is an irreversible process that removes tracer variance; only the former contributes directly to ventilation although mixing influences the interpretation of ventilation from tracer distributions (Villermaux, 2019).

Numerical models demonstrate that regions with higher EKE have enhanced capacity for submesoscale transport of tracers across the base of the mixed layer (Balwada et al., 2018; Lévy et al., 2018; Uchida et al., 2020) and can have an outsized impact on ventilation (Naveira Garabato et al., 2011; Rintoul, 2018; Tamsitt et al., 2016; Viglione and Thompson, 2016). Standing meanders have also been identified as regions where older waters enriched in dissolved inorganic carbon are preferentially transported to the surface (Brady et al., 2021; Tamsitt et al., 2017), which can potentially create local regions of enhanced air-sea gas exchange. Observational studies are needed to validate these largely numerical results.

Due to coarse, ship-based sampling, examination of spatial variations in ventilation have focused on the basin (or ACC sector) scale (Morrison et al., 2022; Sallée et al., 2012). More recently, observations from floats have shown that air-sea fluxes of carbon (Gray et al., 2018) and oxygen (Bushinsky et al., 2017) vary

across the Southern Ocean. Evidence for finer-scale variability in biogeochemical distributions comes from the analysis of Biogeochemical Argo (BGC-Argo) profiles, in which subsurface tracer anomalies are found to be more prevalent in high-EKE regions, suggesting stronger ventilation and export (Llort et al., 2018). High-resolution glider observations near the Southwest Indian Ridge also showed reduced vertical tracer gradients in the standing meander as compared to the low-EKE region downstream (Dove et al., 2021). Although these observational studies have provided initial evidence for the importance of standing meanders in ventilation, the physical processes in the ACC that set the dominant spatial and temporal scales of variability in surface-interior exchange have not yet been fully explored.

This study uses the broad spatial coverage of subsurface dissolved oxygen measurements collected by the BGC-Argo array, as well as remote sensing products, to consider controls on apparent oxygen utilization (AOU) patterns in the Southern Ocean and its relationship to ventilation of surface waters. Both vertical and isopycnal distributions of AOU exhibit substantial variations along the path of the ACC that can be linked primarily to enhanced ventilation in the ACC's major standing meanders. We identify several physical mechanisms that are consistent with these distributions. This work is a critical step for validating ocean models and observationally describing key regions of ventilation of climatologically-important tracers in the Southern Ocean.

2.3 Data and Methods

Biogeochemical-Argo floats

The Argo program has deployed over 10,000 profiling floats across the global ocean since 1999 (Riser et al., 2016) with the Southern Ocean Carbon and Climate Observations and Modeling (SOCCOM) program playing a vital role in increasing the BGC-Argo population of the Southern Ocean (Claustre et al., 2020; Johnson et al., 2017). Argo floats sample the upper 2000 m of the ocean every 10 days. In between profiles, the floats drift at 1000 m and follow a quasi-Lagrangian trajectory. (Roemmich et al., 2009).

This study uses 21,941 profiles of dissolved oxygen, along with the associated temperature and salinity profiles, that were collected within the boundaries of the ACC (defined in section 2.3) during the period January 15, 2003 to May 16, 2021 (Figure 2.1c-e). Only data that have undergone delayed-mode quality control procedures and have been flagged as "good" are used in this analysis. All profile data were obtained

from the "Sprof" files provided by the Argo Global Data Assembly Center (GDAC), which merge biogeochemical samples that are measured at slightly different vertical positions onto a single common pressure axis.

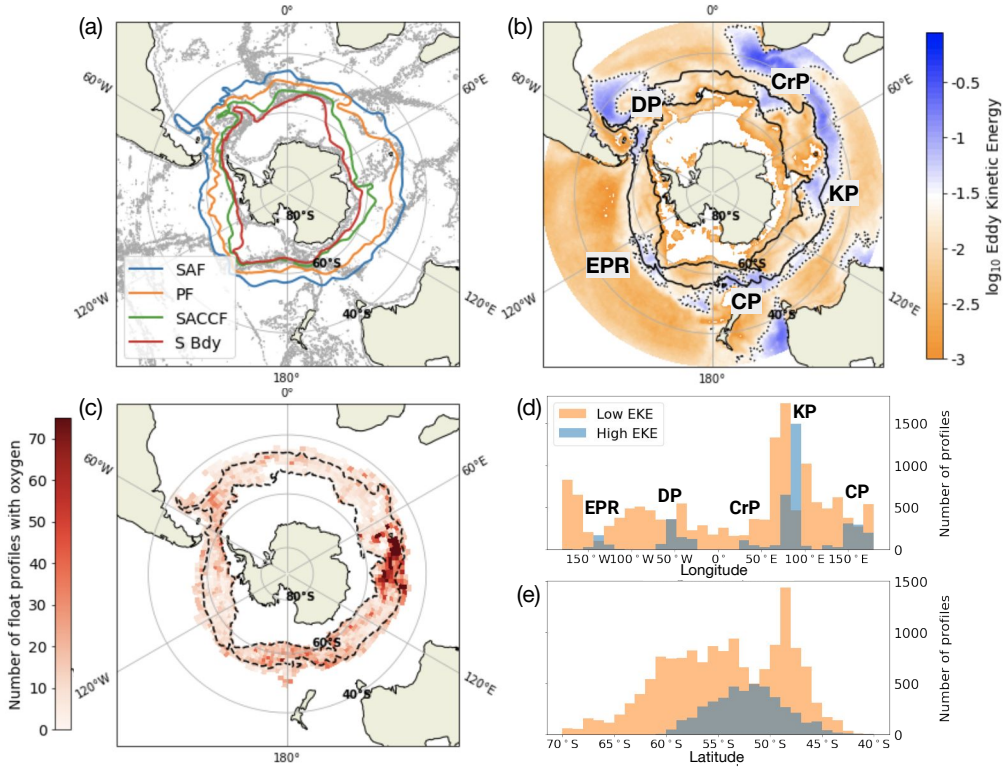

Figure 2.1: Geographic locations and data coverage of eddy kinetic energy hotspots.

(a) Bathymetry and major fronts of the Southern Ocean. Gray contours show 1000 m, 2000 m, and 3000 m isobaths. Fronts are the Subantarctic Front (SAF; blue), Polar Front (PF; orange), Southern ACC Front (SACCF; green), and the Southern Boundary (S Bdy; red). (b) Base-10 logarithm of eddy kinetic energy [$\log_{10}$ m^2 s^{-2}]. Black solid lines show the ACC boundaries used in this study. Black dotted lines denote regions of high EKE. Standing meanders are labeled by the corresponding bathymetric feature: Crozet Plateau (CrP), Kerguelen Plateau (KP), Campbell Plateau (CP), East Pacific Rise (EPR), and Drake Passage (DP). (c) Spatial distribution of float profiles containing oxygen data across the Southern Ocean within the ACC; Δlatitude = 1.25°, Δlongitude = 2.5°. Black dotted lines show the ACC boundaries used in this study. (d) Histogram of the number of float profiles as a function of longitude within the ACC boundaries in panel (b). Profiles categorized as low-EKE are in orange, with high-EKE profiles are in blue. Standing meanders are labeled the same as in panel (b). (e) Histogram of the number of float profiles at a given latitude within the ACC boundaries in panel (b). Colors are the same as in panel (d).

Derived Variables

Apparent oxygen utilization (AOU) is the difference between oxygen saturation concentration and observed dissolved oxygen concentrations (AOU = $O_2^{\text{sat.}} - O_2^{\text{obs.}}$), where the oxygen saturation is a function of observed conservative temperature and absolute salinity. AOU in the surface ocean is typically close to 0 due to equilibration with the atmosphere. Bushinsky et al., 2017 showed that AOU ≈ 0 is generally true for the ACC, but small variations of ±5-10 μmol kg^{-1} exist due to biological activity, surface heat fluxes, or rapid entrainment of thermocline waters (Ito et al., 2004). Lower AOU values are used as a proxy for younger age, signaling recent ventilation, since respiration in the ocean interior is a persistent oxygen sink. AOU is a non-conservative tracer with its value determined by several processes, *e.g.*, remineralization, along-isopycnal stirring, cross-isopycnal mixing, and the non-conservative nature of solubility. AOU has been used to trace pathways between the surface and interior (Llort et al., 2018), and both vertical and along-isopycnal variations provide insight into ventilation dynamics.

We study the distribution of AOU in both density and depth coordinates. Additionally, to account for temporal and spatial variations in mixed layer depths, vertical variations in AOU are also considered as deviations from observed values at the base of the mixed layer in each profile. Depth below the base of the mixed layer is given by Δh, and ΔAOU refers to the difference in AOU between the value at Δh and at the mixed layer depth. The mixed layer depth (MLD) was defined by a density difference criterion of 0.03 kg m^{-3} from the surface (Montégut et al., 2004). Other derived variables, such as potential density, were calculated from temperature and salinity using the Thermodynamic Equation of Seawater 2010 (McDougall and Barker, 2011).

Satellite Data

Eddy kinetic energy (EKE) was calculated as EKE= $\frac{1}{2}\sqrt{\overline{u'^2} + \overline{v'^2}}$, where u' and v' are the zonal and meridional eddy geostrophic velocities estimated from the time-varying sea surface height (SSH) anomaly field, and $\overline{(.)}$ represents a time average calculated over 1993-2016. Regions with EKE greater than 250 cm^2 s^{-2} were considered "high-EKE" (Figure 2.1b, Figure A.1), and individual float profiles were tagged as "high" or "low" EKE based on their surfacing locations. Previous studies have identified distinct dynamical regimes within individual standing meanders (Barthel et al., 2017; Youngs et al., 2017), but we do not distinguish these here.

The ACC boundaries were defined using absolute dynamic topography (ADT) with the northern and southern boundaries given by the –0.1 m and the –1.05 m ADT contours, respectively. These boundaries were selected in part to avoid inclusion of the Agulhas Retroflection, which is a region of enhanced EKE but is not considered in this study. Several definitions of the northern and southern boundaries of the ACC were tested, including hydrographic definitions of frontal boundaries (shown in Figure 2.1a) as opposed to sea level anomaly (Kim and Orsi, 2014), but these led to minimal differences in the results.

Finite-size Lyapunov Exponents (FSLEs) describe the orientation and timescale of strain fields by quantifying stretching and compression (d'Ovidio et al., 2004; d'Ovidio et al., 2010). They are a Lagrangian diagnostic, and for a given flow field are defined as the separation growth rate for particle pairs, $\lambda(d_0, d_f) = \frac{1}{\tau} log(\frac{d_f}{d_0})$, where d_0 and d_f are the initial and final separation distances and τ is the first time where separation distance d_f is reached. Here we use FSLE estimates provided by AVISO+ that were computed from satellite-derived geostrophic velocities. We use the FSLEs from January 1, 2018 to December 31, 2020, but the exact choice of period does not impact the results.

2.4 Results

Subsurface signatures of ventilation

Variations in AOU with depth and density may arise from various mechanisms, some reflecting differences in advection and stirring at scales smaller than the standing meander (discussed in section 3.2), and others related to the larger-scale density structure of the ACC. A simple partitioning of individual float profiles between high- and low-EKE regions reveals striking differences in the vertical structure of AOU between these two regimes (Figure 2.2). Just below the mixed layer, *e.g.*, Δh = 100 m, high- and low-EKE regions both have low ΔAOU values with similar distributions (Figure 2.2a), although low-EKE regions have a longer tail. At Δh = 300 m, high- and low-EKE regions have distinct peaks with the high-EKE region having a lower median; the difference in the distributions' medians is 27 μmol kg^{-1} and the difference in the modes is 68 μmol kg^{-1} (Figure 2.2b,d). For values of $\Delta h \geq 700$ m, the two regions have approximately the same distribution, with a difference in medians of only 2 μmol kg^{-1} (Figure 2c,d). The largest disparity in ΔAOU between the high and low-EKE regions is present for $200 < \Delta h < 700$ m. (Figure 2.2d). This ΔAOU structure is set, in part, by meanders of the ACC that horizontally transport lighter waters southward into energetic regions downstream

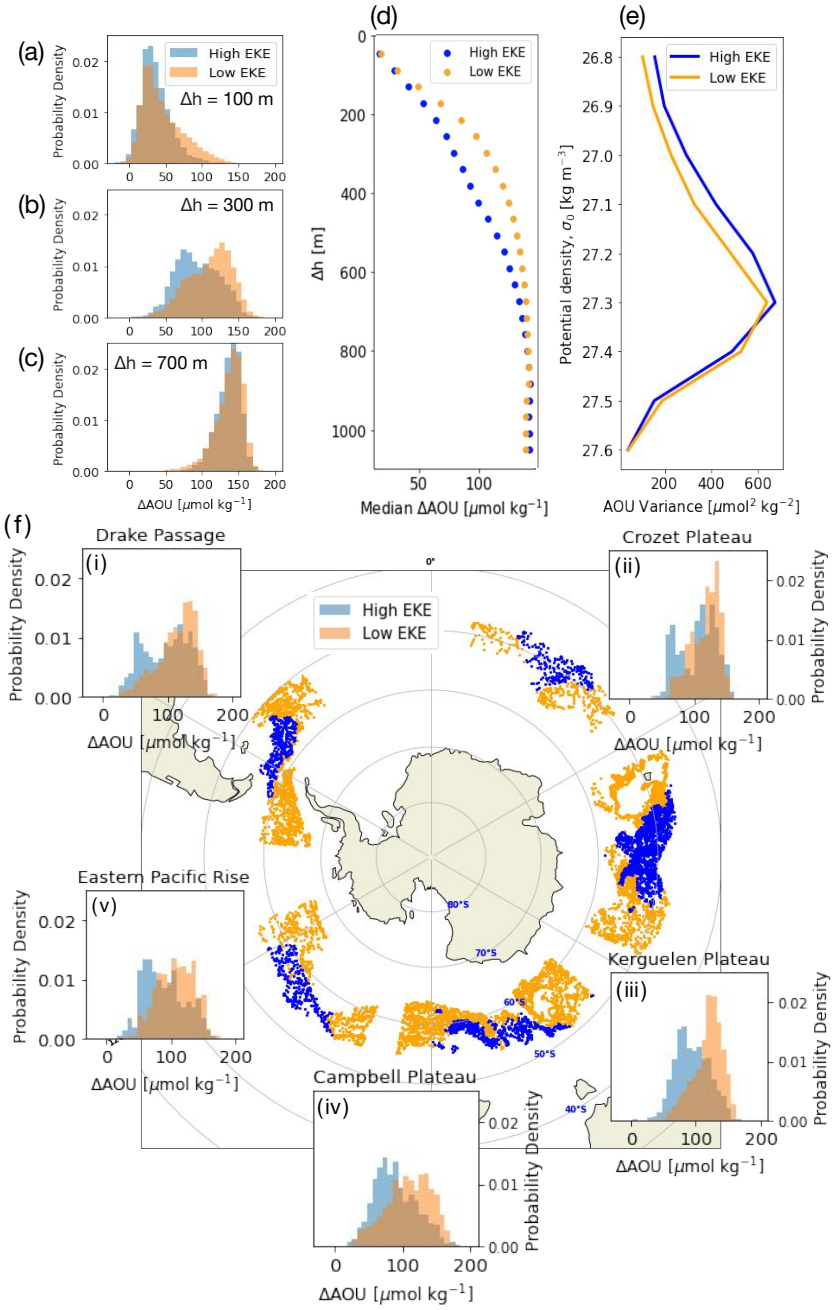

Figure 2.2: Probability density functions of ΔAOU across the full ACC.

Probability density functions across the full ACC of ΔAOU [μmol kg^{-1}] where (a) Δh = 100 m, (b) Δh = 400 m, (c) Δh = 700 m. (d) Median in ΔAOU [μmol kg^{-1}] at values of Δh. (e) Variance of AOU [μmol^2 kg^{-2}] on potential density surfaces. (f) Locations of profiles used to create probability density functions of ΔAOU [μmol kg^{-1}] at Δh = 300 m at (i) Drake Passage, (ii) Crozet Plateau, (iii) Kerguelen Plateau, (iv) Campbell Plateau, and (v) Eastern Pacific Rise. In all panels, blue colors denote high-EKE regions and orange colors denote low-EKE regions.

of topography. At the level of individual standing meanders, the high-EKE regions associated with Kerguelen Plateau, Campbell Plateau, and Eastern Pacific Rise have distributions of ΔAOU that most closely align with the median distributions for the entire ACC (Figure 2.2f.iii, iv, v). The distinction between high- and low-EKE regions is weakest at the Crozet Plateau (Figure 2.2f.ii), although data availability is reduced here.

Changes in hydrographic properties along the path of the ACC provide insight into the origin of subsurface low-AOU waters found in high-EKE regions. CDW is distinguished by high salinity (>34.6 g kg^{-1}) and low temperature ($\sim$ 2°C). Comparatively, Antarctic Intermediate Water (AAIW), a more-recently ventilated water mass, is characterized by lower salinity as a result of sea ice melt. Differences in hydrographic properties are particularly distinct around Δh = 300 m, consistent with large differences in ΔAOU medians between the high- and low-EKE regions (Figure 2.3). In both the high- and low-EKE regions at Δh = 300 m, the distributions of mean AOU as a function of temperature and salinity are similar (Figure 2.3a-c), suggesting that ΔAOU is predominantly tied to the relative contributions of water masses below the mixed layer, with variations due to biology secondary. Stronger differences between the two regions are found, however, when considering the frequency distribution in conservative temperature-absolute salinity space (Figure 2.3d-f). In the low-EKE regions, CDW properties dominate, with a temperature of 2°C and high salinity (34.4 - 34.8 g kg^{-1}; Figure 2.3d). In the high-EKE regions a greater fraction of the observations have lower values of salinity (34.0 - 34.2 g kg^{-1}) and also warmer temperatures (3-5°C; Figure 2.3e,f), consistent with intermediate waters that have been subducted from the surface. The increased presence of waters consistent with AAIW at these depths in the high-EKE regions suggests more intermediate water is subducted in high-EKE regions of the ACC as compared to low-EKE regions.

This hydrographic analysis indicates that mixing of old CDW and recently ventilated AAIW at the basin-scale contributes to the patterns in ΔAOU described in Figure 2.2. Yet, coupled processes on the submesoscale-mesoscale spectrum may still play a role in setting these subsurface ΔAOU distributions, as described in previous observational work in standing meanders (Dove et al., 2021). Using an oxygen utilization rate (OUR) for the upper mesopelagic zone of 40 μmol kg^{-1} $year^{-1}$ (Hennon et al., 2016), low ΔAOU waters with a median of O(70 μmol kg^{-1}) in high-EKE regions would have an age of $\sim$ 2 years, suggesting there may be recent

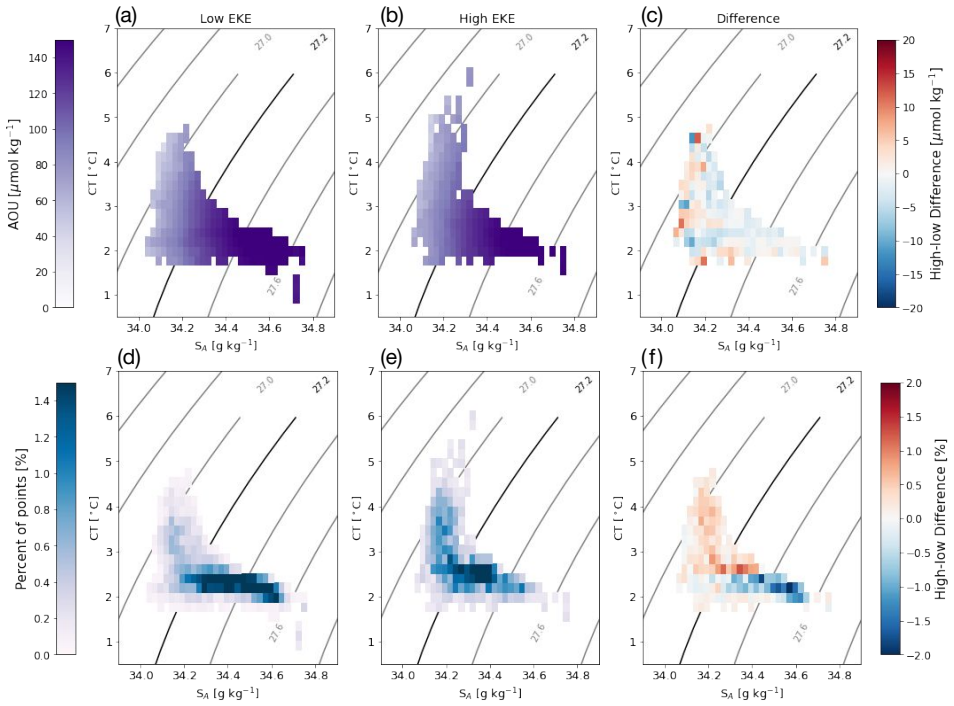

Figure 2.3: Absolute salinity (S_A)-conservative temperature (CT) diagrams.

Average AOU for each S_A-CT position at Δh = 300 m in (a) the low-EKE regions and (b) the high-EKE regions. (c) Difference in AOU between the low and high-EKE regions. Joint histogram of profile locations at at Δh = 300 m in (d) the low-EKE regions and (e) the high-EKE regions. (f) Difference in joint histograms between the low- and high-EKE regions. Grey contours are potential density [kg m^{-3}], with the black contour at 27.2 kg m^{-3}. In all panels, only where there were more than five points at a given CT-S_A value that could be averaged are shown. ΔCT = 0.2°C, ΔS_A = 0.025 g kg^{-1}.

injection from the mixed layer. However, estimates of OUR in the Southern Ocean are sparse and there is a good deal of uncertainty in the estimate of this time scale. Specifically, an OUR of 40 μmol kg^{-1} year^{-1} represents a regional, near-surface value that may not be representative of values at greater depths or over the broader Southern Ocean. Therefore this OUR value should be considered an upper bound, and the low ΔAOU waters observed in high-EKE regions likely include waters that have been subducted below the surface boundary layer for periods longer than 2 years.

It is important to also consider AOU variations on density surfaces because the mean density structure between the high and low-EKE regions is different: the lower EKE regions host denser isopycnals linked to deeper depths and higher AOU values in the

mid- and low-latitude basins to the north (Figure A.2a,b). These variations along the path of the ACC are related to changes in outcropping density classes as well as the steepening of lateral density gradients within standing meanders (Chapman et al., 2015; Thompson and Naveira Garabato, 2014), which may enable recently-ventilated surface waters to be displaced downward in the water column. Despite the different density ranges between the regions, the vertical stratification, measured by the vertical buoyancy gradient N^2, is similar (Figure A.2c). Considering the Argo observations in density space shows that the heavier isopycnals have relatively homogeneous mean AOU distributions along the path of the ACC, which is likely a result of the rapid along-ACC circulation (Figure A.3, A.4). However, lighter isopycnals and regions where isopycnals are shallower show inhomogeneities in mean AOU along the path of the ACC, due in part to the outcropping of denser isopycnals in low-EKE regions. Some of the signal of lower mean AOU concentrations, particularly at deeper depths, may be attributed to adiabatic heaving rather than ventilation by advection and mixing. In the next section, we offer evidence that high-EKE regions are subject to more energetic stirring, leading to enhanced along-isopycnal variance of AOU, suggesting that AOU variations do not result from isopycnal heaving alone.

Mesoscale and submesoscale contributions to ventilation

Variations in AOU due to the ACC's density structure occur at standing meander and larger scales ($\geq$ 1000 km); below these scales, mesoscale and submesoscale motions can impact ventilation through a number of different mechanisms. These include (1) increased along-isopycnal stirring as a result of enhanced EKE; (2) frontal subduction as a result of frontogenesis in the standing meander; and (3) enhanced vertical transport by submesoscale motions. Here, we investigate how these processes shape along-ACC differences in AOU distributions.

Differences in isopycnal AOU variance between high- and low-EKE regions offers insight into how along-isopycnal stirring contributes to ventilation within the ACC. To remove the effects of vertical isopycnal displacement (i.e., heave; Figure A.3), we consider deviations from a longitude-dependent (10-degree longitude bins), along-isopycnal mean AOU value. The variance in AOU on density surfaces <27.4 is up to 18% larger in high-EKE regions than in low-EKE regions, with a peak in variance at 27.3 kg m^{-3} in both regions. The observed enhanced AOU variance in high-EKE regions is consistent with along-isopycnal stirring bringing low-ΔAOU waters to depth, as opposed to this signal solely occurring due to variations in the ACC's

large-scale density structure. Enhanced variance in the high-EKE regions may arise from both stirring processes and injection of tracer anomalies from the surface layer onto density surfaces below the mixed layer. With regard to exchange out of the mixed layer, seasonal or along-stream changes in mixed layer properties may be expected to modify ventilation. However, the float data indicate that MLD and stratification at the base of the mixed layer are similar in high- and low-EKE regions and therefore do not contribute to the disparity in subsurface ΔAOU distributions (Figure A.5).

In addition to being regions of energetic mesoscale eddies, ACC standing meanders are regions of strong surface frontogenesis that give rise to large mixed layer lateral density gradients. These gradients are reservoirs of potential energy that can give rise to instabilities that lead to intense submesoscale vertical motions and increase the efficiency of tracer transport between the surface and interior ocean, contributing to ventilation (Klein and Lapeyre, 2009; Lévy et al., 2018; Mahadevan, 2016). While these instabilities typically occur on spatial and temporal scales consistent with the submesoscale, they are shaped by the mesoscale flow field (Balwada, LaCasce, et al., 2021; Balwada et al., 2018; Rosso et al., 2015). We investigate the potential of enhanced ventilation occurring via frontogenesis and submesoscale subduction by considering the relative magnitude of lateral density gradients between low- and high-EKE regions. Measuring lateral density gradients can be achieved with high temporal and spatial resolution measurements, but such observations are sparse in the Southern Ocean. Siegelman et al., 2020 empirically showed that maximum stretching FSLEs (hereafter FSLEs) calculated from satellite-derived flow fields can be used to approximate the magnitude of lateral density gradients and derived a relationship between the two quantities. Specifically, density anomalies are physically aligned with FSLEs, so larger magnitude FSLEs are correlated with stronger lateral density gradients. While FSLEs have previously been linked to mixed-layer density gradients, Siegelman et al., 2020 demonstrated that this relationship may extend below the mixed layer in the Southern Ocean, particularly in energetic regions.

Consistent with the heterogeneous distribution of EKE in the ACC, lateral density gradients (as inferred from FSLEs) undergo abrupt transitions in standing meander regions (Figure 2.4a). The probability distribution of FSLE has a log-normal distribution within both low- and high-EKE regions (Figure 2.4b). However, in the high-EKE region, the median value is shifted to larger magnitudes and the distribution has a longer tail, which we link to stronger and more frequent small-

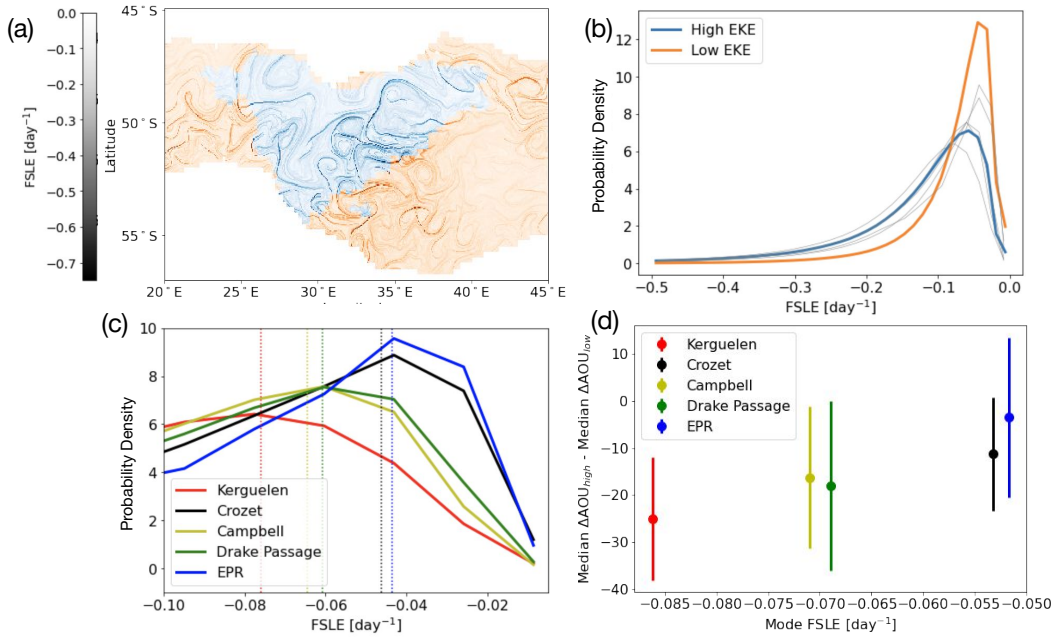

Figure 2.4: Finite-Size Lyapunov Exponents (FSLE) analysis.

(a) Snapshot of FSLEs from March 1, 2020 centered on the Crozet Plateau region of the ACC. Blue regions are high-EKE while orange are low-EKE, using the EKE definition defined in the methods. (b) Probability density function of maximum stretching FSLE in the high- (blue) and low- (orange) EKE regions across the full ACC. Gray lines are expanded in (c). (c) Probability density function of maximum stretching FSLE at in the Kerguelen Plateau (red), the Crozet Plateau (black), the Campbell Plateau (yellow), Drake Passage (green), and the Eastern Pacific Rise (EPR; blue). Vertical lines represent 75th percentiles with colors the same as above. (d) Plot of the mode of the FSLE in the high-EKE region versus the differences in the high and low medians of the ΔAOU probability density functions (δAOU) at Δh = 250 m. Error bars are standard deviations of δAOU and colors are the same as in (c).

scale surface density gradients. The FSLE probability density function also differs for each individual standing meander (Figure 2.4c). The standing meander at Kerguelen Plateau has the most negative (strongest) FSLE values, implying an increased frequency of strong lateral density gradients and potentially enhanced vertical transport. The standing meanders associated with the Crozet Plateau and Eastern Pacific Rise have the least negative (weakest) mode of FSLE probability, with the Campbell Plateau and Drake Passage falling between the extremes.

To consider the relationship between FSLEs and ΔAOU within individual standing meanders, we define localized low-EKE regions that surround each high-EKE standing meander, defined between the north-south ACC boundaries and extending

5 degrees of longitude to either side of the meander. For each of the five major standing meander regions, the median difference in ΔAOU between the high- and *localized* low-EKE regions at Δh = 250 m is calculated; we refer to this as δAOU. A large magnitude of δAOU represents large differences in ΔAOU distributions between the high-EKE standing meander and the surrounding low-EKE region, while a negative δAOU indicates a greater volume of low-AOU water in the high-EKE region. In other words, a large, negative value of δAOU suggests that the high-EKE region experiences enhanced ventilation as a result of the stirring and submesoscale subduction processes described above, as compared to the surrounding low-EKE region. Differences in FSLE distributions between meanders are correlated with differences in δAOU (Figure 2.4d) for depths of Δh up to 500 m. The standing meander that has the largest FSLE mode magnitude (implying strongest stirring), Kerguelen Plateau, is associated with the largest δAOU. Standing meander regions with smaller magnitude FSLE modes, the Eastern Pacific Rise and Crozet Plateau, have δAOU values closer to zero. While five meanders dominate the high-EKE regions in the ACC, this analysis suggests that contributions of low ΔAOU waters to depth may be localized to only one or two intense standing meanders, Kerguelen and Campbell plateaus, indicating these standing meanders may play the dominant role in ventilation of the ACC.

2.5 Discussion

Ventilation of surface properties and tracers can arise from a combination of large-scale circulation features, *e.g.* shaping of density surfaces through flow-topography interactions, as well as smaller-scale stirring by mesoscale and submesoscale motions. There is increasing evidence from both observational and numerical studies that motions occurring in the mesoscale and submesoscale range are tightly coupled. Mesoscale strain, through the process of frontogenesis, is responsible for the generation of near-surface lateral density gradients that are precursors for strong vertical submesoscale velocities (Archer et al., 2020; Su et al., 2020). A possible scenario is that these enhanced submesoscale velocities in high-EKE regions rapidly inject surface properties to depths of 300-m or even deeper. Llort et al., 2018 did indeed find evidence of deep, unmodified waters (anomalously low AOU values), which only occurred in high-EKE standing meander regions. Yet, these deep anomalies were found in <1% of all float profiles. An alternate scenario, in line with Balwada et al., 2018, Balwada, Xiao, et al., 2021, and Freilich and Mahadevan, 2021, and one that is more consistent with the observed ΔAOU values, is that submesoscale

motions play the essential role of efficiently carrying surface properties across the base of the mixed layer. After this, stirring along isopycnals, by the same eddies that create the surface density gradients, enhances the transfer of these surface properties to depth. Thus, while attributing ventilation to different physical processes is important for ensuring that they are represented accurately in climate models, the coupling of motions across scales likely makes this task challenging. Accordingly, numerical models that do not fully resolve mesoscale and submesoscale processes may misrepresent the formation of intermediate waters, as well as the concentration of oxygen in thermocline.

While this study has focused on ventilation pathways of oxygen in the ACC, these results likely have important implications for the spatial variability of air-sea CO_2 fluxes. Oxygen has an equilibrium timescale that is at least an order of magnitude shorter than that of CO_2, which has an equilibration timescale of O(6 months). Combining this study with evidence that ACC standing meanders are also sites of enhanced upwelling (Brady et al., 2021; Tamsitt et al., 2017) suggests that recently-ventilated deep waters in these regions may have short surface residence times, and therefore full equilibration with atmospheric CO_2 may not be reached (Jones et al., 2014). This provides further motivation for exploring how localized high-EKE regions impact exchange of waters between the surface and interior and the larger Southern Ocean carbon cycle.

Various estimates of air-sea exchange of CO_2 in the Southern Ocean have identified interannual to decadal-scale variations in the region's ability to provide an atmospheric carbon sink (Gruber et al., 2019; Landschützer et al., 2015). Notably, these estimates are obtained after some form of interpolation or mapping, *e.g.* neural network (Landschützer et al., 2016), of CO_2 measurements from repeat shiptracks that typically do not sample the strongest and most variable EKE regions. Decadal-scale variations in the Southern Ocean carbon sink have been largely attributed to large-scale processes, such as a change in the Southern Annular Mode (Le Quéré et al., 2007; Lovenduski et al., 2008, a southward shift and strengthening of the westerly winds (DeVries et al., 2017), and enhanced stratification due to increased northward advection of sea ice and southward advection of warmer waters (Landschützer et al., 2015). Localized processes may shape the temporal evolution of air-sea fluxes across the Southern Ocean. For instance, Y. Zhang et al., 2021 illustrate that the standing meander associated with the Campbell Plateau governs trends in EKE over the full Pacific basin. This may also extend to air-sea flux properties; for example, Langlais

et al., 2017 show that standing meanders dominate the transfer of anthropogenic carbon to AAIW. This sequestration is underresolved in models and underobserved *in situ*. Processes at the standing meander level, including enhanced localized winds and jet-submesoscale interactions, may play a vital role in shaping air-sea exchange of climatologically important properties such as CO_2 Bachman and Klocker, 2020. This aligns with our findings that standing meanders are likely hotspots for ventilation and suggests that dynamics occurring at scales currently unresolved by most climate models are critical for the transfer of atmospheric anomalies to the ocean interior.

2.6 Conclusions

We provide observational evidence of heterogeneous subsurface vertical distribution of AOU along the full path of the ACC. In both depth and density space, we find substantial differences in AOU linked to enhanced ventilation in high-EKE regions associated with the ACC's major standing meanders. While shifts in the ACC's density surfaces due to topographic steering at standing meanders explain some of the observed distribution, we also identify mechanisms on the submesoscale-mesoscale spectrum that can contribute to the ventilation of AOU. Data from BGC-Argo floats, especially those deployed by the SOCCOM project, have enhanced our ability to understand the processes impacting ventilation across the entire Southern Ocean, and here we use those data to suggest localized regions of high EKE play an outsized role in such ventilation. Accordingly, it is vital to consider sub-basin-scale variability and, in particular, how temporal variations in high-EKE standing meanders can impact global Southern Ocean properties that influence and reflect biogeochemical cycling.

Chapter 3

CHARACTERIZING SCALES OF VARIABILITY IN A STANDING MEANDER

This work is published in *Journal of Geophysical Research: Oceans* as "Observational Evidence of Ventilation Hotspots in the Southern Ocean." (Dove et al., 2021).

3.1 Abstract

Standing meanders are a key component of the Antarctic Circumpolar Current (ACC) circulation system, and numerical studies have shown that these features may locally enhance subduction, upwelling, as well as lateral and vertical tracer transport. Yet, observational data from these regions remain sparse. Here we present results based on measurements made by a group of autonomous platforms sampling an ACC standing meander formed due to the interaction of the Polar Front with the Southwest Indian Ridge. Two Seagliders were deployed alongside a Biogeochemical-Argo float that was advected through the standing meander. In the high eddy kinetic energy region of the standing meander, the glider observations reveal enhanced submesoscale frontal gradients as well as heightened tracer variability at depth, as compared to the more quiescent region further downstream. Vertical gradients in spice and apparent oxygen utilization are reduced in the standing meander despite similarities in the large-scale vertical stratification, suggesting greater ventilation of the surface ocean. These observations are consistent with numerical studies that highlight standing meanders as hotspots for ventilation and subduction due to enhanced mesoscale stirring and submesoscale vertical velocities. Our results emphasize the need to account for spatial heterogeneity in processes influencing air-sea exchange, carbon export, and biogeochemical cycling in the Southern Ocean.

3.2 Introduction

The Southern Ocean exerts a strong control on the global climate as the primary site of both deep water ventilation at the ocean surface and subduction of newly-formed intermediate water masses (Marshall and Speer, 2012). Tilted density surfaces spanning the Antarctic Circumpolar Current (ACC) expose a range of density classes at the ocean surface, causing the Southern Ocean to be a key site for

the uptake and sequestration of anthropogenic carbon dioxide from the atmosphere (Frölicher et al., 2015; Gruber et al., 2019). Observations in the Southern Ocean have historically been both spatially and temporally sparse, contributing to disagreements between carbon uptake estimates in models and observations (Gruber et al., 2019) and limiting attribution to specific processes that explain these discrepancies. The deployment of Biogeochemical-Argo (BGC-Argo) floats as part of the Southern Ocean Carbon and Climate Observations and Modeling (SOCCOM) project, which began in 2014, has started to fill the gap in observations of biogeochemical tracers, especially in winter months (Gray et al., 2018; Johnson et al., 2017; Riser et al., 2016). The typical float sampling strategy of repeat profiling every ten days maximizes the temporal and spatial coverage of the resulting dataset, at the cost of aliasing mesoscale and submesoscale dynamics that can have a leading order impact on larger-scale Southern Ocean properties (Rintoul, 2018). Due to the lack of high-frequency subsurface observations, the impact of mesoscale and submesoscale processes on modulating biogeochemical tracer distributions in the Southern Ocean remains largely unresolved.

Export production, the flux of net primary production across the base of the ocean's euphotic zone, is a critical step for the sequestration of carbon from the atmosphere into the deep ocean (Buesseler and Boyd, 2009; Lévy et al., 2013; Sallée et al., 2012). Our appreciation of the complexity of the organic carbon pump has expanded in recent years (Boyd et al., 2019), making it clear that the vertical carbon flux associated with gravitational sinking alone is insufficient to close the carbon budget (Boyd et al., 2019; Lévy et al., 2013; Schlitzer, 2002). Ecological processes (*e.g.* predator migration) and physical processes have both been highlighted as potential mechanisms for enhancing carbon export fluxes (Lévy et al., 2012; Lévy et al., 2018; Omand et al., 2015). Physical processes that contribute to non-gravitational carbon export are associated both with modulation of mixed layer depths (MLDs) and with direct transport by vertical motions across the base of the mixed layer. The MLD changes in response to wind and buoyancy forcing, the latter caused by surface heating, freshwater fluxes, or sea ice melt that act dominantly at seasonal timescales with contributions from processes occurring at higher-frequency timescales as well (Bol et al., 2018; Dall'Olmo et al., 2016; Palevsky et al., 2016). Export may also occur via subduction processes at frontal zones due to associated strong vertical velocities (Klein and Lapeyre, 2009). The three-dimensional overturning structure and energetic eddy field of the Southern Ocean preconditions this region to have a significant contribution to export from physical processes (Llort et al., 2018; Omand

et al., 2015).

Assessment of the potential for physical export in the Southern Ocean must account for the multi-scale nature of the circulation. At larger scales, the ACC is comprised of a series of eastward-flowing frontal jets that are typically efficient water mass barriers (Orsi et al., 1995). These frontal flows are accompanied by strongly tilting density surfaces in thermal wind balance that allow for the adiabatic ventilation of deep waters and sustain a vigorous mesoscale eddy field (Rintoul and Naveira Garabato, 2013). A small number of standing meanders form in the ACC where these jets interact with major topographic features, including one arising from the flow of the Polar Front (PF) over the Southwest Indian Ridge (SWIR). This standing meander is the focus of this study (Figure 3.1). In these standing meander regions, flow-topography interactions can cause transport barriers to become "leaky" (Naveira Garabato et al., 2011) as well as enhance eddy kinetic energy (EKE) (Gille and Kelly, 1996; Lu and Speer, 2010; Witter and Chelton, 1998), vertical momentum transport (Thompson and Naveira Garabato, 2014), lateral tracer transport (Dufour et al., 2015; MacCready and Rhines, 2001; Roach et al., 2016; Thompson and Sallée, 2012), upwelling (Tamsitt et al., 2017; Viglione and Thompson, 2016), and subduction (Bachman and Klocker, 2020; Llort et al., 2018). Observational studies of the circulation in the SWIR region, e.g., Pollard and Read, 2001, have identified a steady, largely barotropic jet associated with the PF, which is stabilized by the ridge before "fragmenting" into multiple smaller-scale jets further downstream. This area plays a central role in the upwelling branch of the overturning circulation (Tamsitt et al., 2017).

ACC standing meanders are characterized by enhanced EKE and strain rates due to persistent conditions favorable for baroclinic and barotropic instabilities (Lu et al., 2016; Youngs et al., 2017). The imprint of coherent eddies on tracer structure, $e.g.$ surface chlorophyll, occurs over horizontal scales of O(10-100km). These eddies typically have a vertical extent of O(2000 m) and stir tracers below the mixed layer in the interior (Balwada, LaCasce, et al., 2021; Balwada et al., 2016). Near the surface, mesoscale eddies usually have an inlay of strong submesoscale O(1-10 km, 1 hour-10 days) currents, which are often visible as cusps and filaments in surface tracers. These smaller scale motions are energized by the production of surface buoyancy gradients through mesoscale frontogenesis (Adams et al., 2017; Klein and Lapeyre, 2009) and by the formation of submesoscale eddies through mixed layer baroclinic instabilities (Boccaletti et al., 2007) or through wind-front

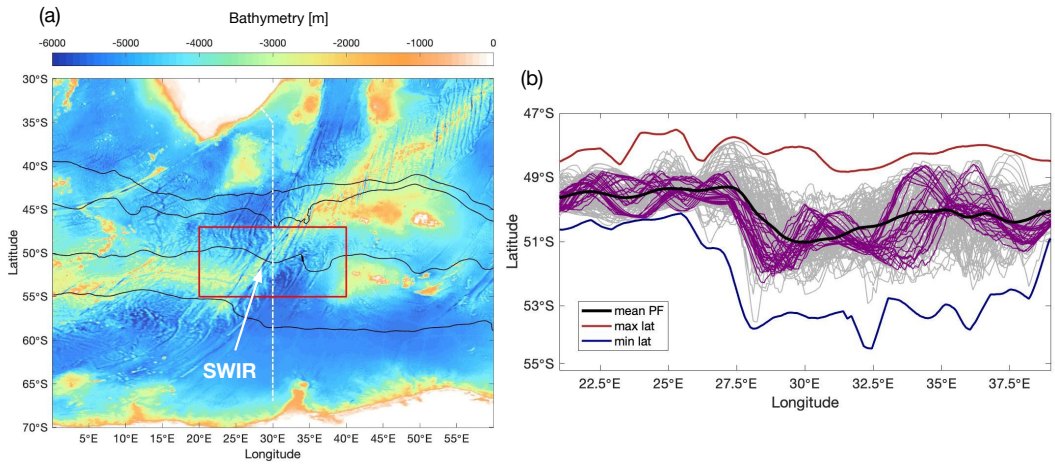

Figure 3.1: Southwest Indian Ridge standing meander location and variability.

(a) Bathymetry of the western Indian sector of the Southern Ocean. The white dotted line shows the path of the I6S GO-SHIP cruise track; the red box outlines the study region shown in panel (b). Thin black lines denote the major fronts of the ACC as defined in Gray et al., 2018. Southwest Indian Ridge is labeled as SWIR. (b) Latitude of the SSH contour corresponding to the PF as defined by Kim and Orsi, 2014. Gray lines show weekly examples from 2017-2020, and the black line shows the mean location. Purple lines show examples of the PF location from every 3 days during the glider deployment timeframe (April 29-July 25, 2019). Blue and red lines are the maximum and minimum latitudinal extents of the PF, respectively.

interactions (Thomas et al., 2008). Submesoscale currents are generally associated with elevated vertical velocities and restratification tendencies in the mixed layer (Su et al., 2018). Strong vertical velocities may penetrate up to a few 100 m below the base of mixed layer (Siegelman et al., 2020), playing an important role in transporting material across the base of the mixed layer and connecting the surface ocean to the mesoscale-dominated interior.

Both observational and modeling studies have confirmed that the Southern Ocean has an active submesoscale flow field (Adams et al., 2017; Bachman et al., 2017; du Plessis et al., 2017; du Plessis et al., 2019; Rosso et al., 2014; Viglione et al., 2018), although the degree to which submesoscale motions are effective at enabling surface-interior exchange has been limited to modeling studies (Balwada et al., 2018; Brannigan, 2016; Mahadevan, 2016; Uchida et al., 2019). In some regions, strong upper-ocean vertical stratification, often induced by sea-ice melt in the marginal ice zone, may limit the vertical extent of submesoscale motions (Swart et al., 2020). However, observations in a region of vigorous EKE and mesoscale strain further

to the north have been used to infer enhanced vertical velocities well below the ocean surface (Siegelman et al., 2019). Constraining the impact of submesoscale dynamics on vertical tracer exchange from observations requires high spatial- and temporal-resolution measurements that are challenging to acquire, particularly in regions with a strong mean flow. Inhomogeneity in submesoscale variability is a key feature of the Southern Ocean that appears to be strongly shaped by interactions with topography (Rosso et al., 2015; Viglione et al., 2018).

Tracer variability arising from mesoscale is difficult to distinguish from that caused by submesoscale dynamics, and previous modeling work has demonstrated the close link between these scales. Increasing model resolution leads to the production of more small-scale features, but they remain structured around the mesoscale eddy field (Balwada et al., 2018). Mesoscale strain has also been shown to be a proxy for the magnitude of submesoscale vertical velocities (Rosso et al., 2015; Siegelman et al., 2020). The entangled nature of mesoscale and submesoscale flows, together with the three-dimensional nature of the currents, means that while fine-scale structure in tracer variability is a well-known feature of the Southern Ocean (Joyce et al., 1978; Pollard and Read, 2001), attribution of this structure to specific dynamical processes remains challenging.

The primary goal of the Southern Ocean Glider Observations of Submesoscales (SOGOS) project was to observe the variability of physical and biogeochemical properties around a BGC-Argo float at much higher spatial and temporal resolution than the typical float sampling, through the use of two ocean gliders. Details of the autonomous platforms and their sampling capabilities are provided in Section 3.3, and the measurements collected by these platforms that are used to examine the influence of mesoscale and submesoscale processes on ventilation are presented in Section 3.4. Section 3.5 considers these measurements in the context of recent numerical simulations and shows that the observational evidence supports the hypothesis that ACC standing meanders are sites of enhanced Southern Ocean ventilation. We conclude in Section 3.6 by suggesting how these results inform sampling strategies of future Southern Ocean observing systems (Meredith et al., 2013) as well as our ability to monitor future changes to the Southern Ocean carbon sink.

3.3 Data and Methods

Autonomous platforms and sensors

The SOGOS field campaign began with the deployment of two Seagliders (SG659 and SG660) in conjunction with a SOCCOM BGC-Argo float (WMO 5906030) on May 1, 2019 at 51.49°S, 30.03°E, from the I06S GO-SHIP cruise (April-May 2019, `www.go-ship.org`). All platforms were advected downstream to the east, experiencing meridional deviations due to flow meanders. The float and gliders sampled immediately in the lee of the SWIR, a major topographic feature in the western Indian sector of the Southern Ocean; the observation region fell roughy between 30°E to 40°E and 50°S to 54°S (Figure 3.2). The gliders sampled for a period of 86 days, ending their mission on July 25, 2019. SG659 and SG660 completed 462 and 509 V-shaped profiles from the surface to 1000 m and back, respectively, with 3-5 hours (average 4.5 hours) and 2-4 km (average 3.25 km) between surfacings. The BGC-Argo float has continued to profile since deployment and remains active as of the submission date of this manuscript. During the dedicated SOGOS period, the float sampled at five-day intervals, completing 16 vertical profiles. The drifting depth of the float was 1000 m, and the profile depth alternated between 2000 m and 1000 m during the five-day interval sampling.

The SOCCOM BGC-Argo profiling float was equipped with a suite of sensors to collect profiles of physical and biogeochemical properties in the upper 2000 dbar. A standard conductivity-temperature-depth (CTD) sensor (SeaBird 41CP) recorded bin-averaged salinity, temperature, and pressure at 2-m vertical resolution above 1000 m and 100-m vertical resolution below. Dissolved oxygen concentrations were measured with an Aanderaa 4330 optode (Tengberg et al., 2006) at variable vertical resolution, and these data were calibrated using float-based observations of atmospheric oxygen Johnson et al., 2015. The float detected chlorophyll fluorescence and optical backscatter at 700 nm with a WET Labs FLBB (Haëntjens et al., 2017). Nitrate and pH were also measured using an ultraviolet spectrophotometer (Johnson et al., 2013) and an ion-sensitive field effect transistor (Johnson et al., 2016), respectively, although those data are not used in the present study.

The gliders each carried unpumped CTD (CT-Sail) sensors measuring conductivity (salinity), temperature, and pressure; an Aanderaa oxygen optode; and a WET Labs ECO puck that measured induced fluorescence and optical backscatter. The salinity and temperature data from the glider sensors were calibrated to deep (>600 m) values from a ship-based profile taken during the congruous I06S GO-SHIP cruise

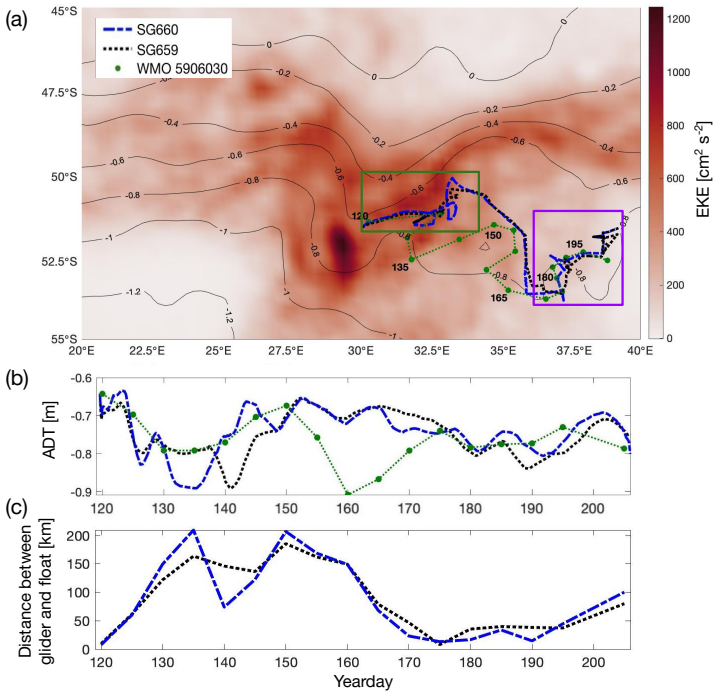

Figure 3.2: Study region for the SOGOS field deployment.

(a) Mean eddy kinetic energy (EKE; [cm^2 s^{-2}]) from 2017-2020 in the same area as boxed in Figure 3.1a. Gray contours give the mean absolute dynamic topography (ADT) from AVISO over the same time period, ranging from -1.2 to 0 m with 0.2 m increments. Lines represent the paths of SG660 (blue) and SG659 (black) and the profile positions of float WMO 5906030 are denoted by green points. Numbers represent the yearday when the float performed a vertical profile. Green box represents the high-EKE region and purple box represents the low-EKE region as discussed in the text. (b) ADT values at the locations of the float and glider profiles. Although the gliders were persistently north of the float during the early stages of the deployment, they sampled similar water masses as indicated by their proximity in SSH space. (c) Distance [km] between each of the two gliders and the float.

at the deployment site. Calibration of the gliders to the float was performed when the gliders and float were within 10 km of each other. No sensor drifts were observed but pressure-dependent offsets of the temperature and salinity were used for each glider. Oxygen measurements were collected over the full 1 km dive depth; to conserve battery power, optical measurements were collected down to 400 m with occasional dives down to 1 km to determine a background signal. Oxygen measurements were calibrated with reference to the float when the float and each glider were within 10 km of each other. Only deep (>600 m) waters were used for calibration to account for surface variability and used to calculate a gain correction

for the glider oxygen, similar to the method pioneered in Johnson et al., 2015. A pressure correction was also applied to the gliders' oxygen measurements below the mixed layer.

Optical backscatter data on the gliders were measured at two wavelengths: 470 nm and 700 nm. Raw sensor counts were calibrated using the manufacturer-supplied scale factor and dark counts. The resulting volume scattering function includes scattering signal from pure seawater and particulate scattering (Vaillancourt et al., 2004; X. Zhang et al., 2009). The scattering by seawater was calculated using a function described in X. Zhang et al., 2009 and subtracted from the volume scattering function. The resulting particulate volume scattering function was converted into particulate optical backscattering coefficient b_{bp} (Bol et al., 2018; Briggs et al., 2011). Finally, following Briggs et al., 2011, the backscatter data were filtered using a seven-point minimum filter followed by a seven-point maximum filter in order to remove spikes, which often occur in profiles of b_{bp} due to aggregate material.

Glider data were objectively mapped onto a regular grid with 10-m depth resolution along the vertical axis and 500-m distance resolution along the horizontal axis, using a Gaussian weighting function with a vertical scale of 20 m and a horizontal scale of 5000 m. A visual comparison of the raw data to the objectively-mapped data set revealed no significant biases due to this choice of resolution. The time associated with each glider position was interpolated to the horizontal distance grid to give an along-track time in number of days since January 1, 2019.

Several additional quantities were derived from the measured properties. Potential density and spice, a variable most sensitive to isopycnal thermohaline variations and least correlated with the density field, were calculated from temperature and salinity using the Thermodynamic Equation of Seawater 2010 (McDougall and Barker, 2011). Adjacency of positive (warm, salty) and negative (cold, fresh) spice anomalies can be used to identify thermohaline intrusions. The MLD was defined by a density difference criteria of 0.05 kg m^{-3} from a 10-m reference level. We follow the methods of previous work (Thompson et al., 2016; Viglione et al., 2018) to calculate the Ertel Potential Vorticity (PV) from the glider data, estimated here as

$$PV \approx fN^2 - M^4 f^{-1}, \tag{3.1}$$

where $N^2 = b_z$, $M^4 = b_x^2$, and $b = g\rho_0^{-1}(\rho_0 - \rho)$. Here, ρ is potential density and subscripts indicate partial derivatives and x is in the along-glider-trajectory direction. Discussion of the assumptions and limitations associated with estimating PV from

glider data using Equation 3.1 is described in detail in the aforementioned studies. From the biogeochemical measurements, apparent oxygen utilization (AOU) was calculated as the difference between the measured oxygen and the oxygen saturation value for a given salinity and potential temperature.

Additional data sets

Hourly estimates of surface forcing fields for the region during the study period were obtained from the ERA5 atmospheric reanalysis. Net surface heat flux was calculated as the sum of the shortwave, longwave, sensible and latent heat flux estimates. Surface freshwater flux was computed using the total precipitation and evaporation estimates. Surface wind stress was calculated using the 10 m winds (u_{10}, v_{10}) and a simple drag law; $\tau = \rho C_d U^2$, where $\rho = 1.225$ kg m^{-3} is the air-density, $C_d = 0.00125$ is the drag coefficient (set constant here for simplicity), and U^2 is the square of the wind speed. The zonal and meridional components of the wind stress were calculated as $\tau_x = \tau \left(u_{10} U^{-1}\right)$ and $\tau_y = \tau \left(v_{10} U^{-1}\right)$.

Daily estimates of sea surface height (SSH) relative to the geoid for the time period 2017-2020 were obtained from the L4-gridded satellite altimeter product provided by Aviso+, along with u' and v', the zonal and meridional geostrophic velocities associated with the time-varying, anomalous component of the SSH field. Regional EKE was calculated as $EKE = \frac{1}{2}\sqrt{u'^2 + v'^2}$. The mean was computed over the period 2017-2020, although the magnitude and spatial pattern of EKE did not vary significantly from year to year. SSH, represented by absolute dynamic topography (ADT), is determined as the sum of the time-mean dynamic topography and time-varying sea level anomaly. ADT values at the glider and float locations were determined using the satellite gridpoint closest to the surfacing location of the instrument.

3.4 Results

Regional variability

We first describe the large-scale variability within the study region, with an emphasis on how the sampling of the autonomous platforms during the SOGOS mission fits into that broader picture. As noted above, the circulation in this area is dominated by the standing meander that forms through the interaction of the PF with the SWIR (Figure 3.1). The meridional variability of the PF immediately downstream of the SWIR (based on satellite observations following the methods of Kim and Orsi, 2014) illustrates that the frontal position is relatively constant upstream of the SWIR as

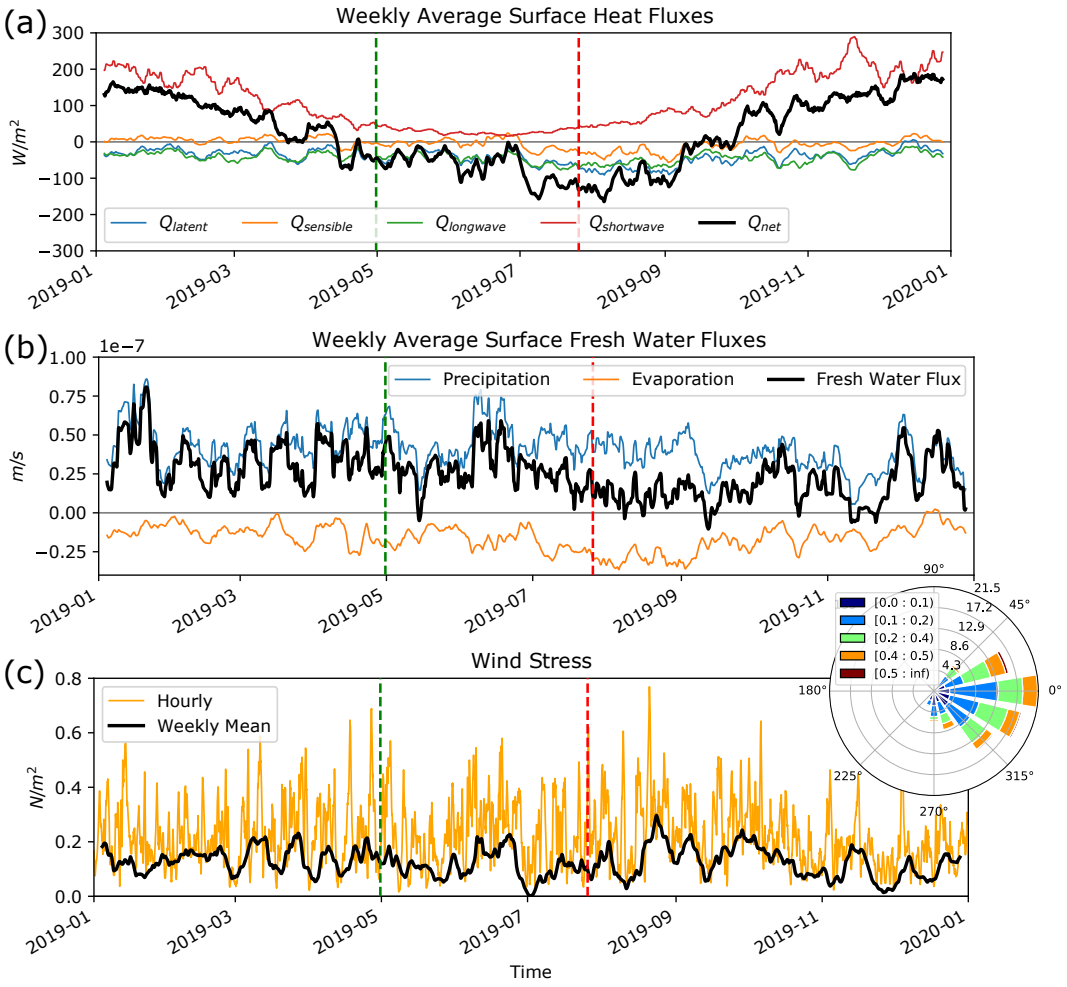

Figure 3.3: Surface forcing fields from ERA5 during the SOGOS deployment.

(a) Weekly-averaged surface heat fluxes (W m^{-2}) and its components, (b) weekly-averaged surface freshwater fluxes (m s^{-1}), and (c) hourly- and weekly-averaged surface wind stress (N m^{-2}). All variables were averaged spatially over $30 - 39^{o}E$ and $50 - 53.5^{o}S$. The inset (d) shows a windrose plot of the hourly wind stress during the period of glider deployment. The direction shows wind stress orientation while the legend indicates wind stress magnitude. The dashed vertical green and red lines in each panel represent the start and end dates of the glider surveys.

compared to just downstream (Figure 3.1b). The downstream variability is consistent with a breakdown of the zonal flow and the formation of mesoscale eddies. Mean EKE accordingly reaches a local maximum within the standing meander (Figure 3.2a).

All SOGOS platforms spent most of their time sampling close to the PF in waters collocated with SSH values of approximately -0.7 m, hereafter referred to as PF

core waters (Figure 3.2b). Within these waters, the gliders and float captured two distinct flow regimes. The mean EKE within the standing meander portion (between 30°E to 33°E and 50°S to 52°S) was 460 cm^2 s^{-2}, over an order of magnitude larger than the 20 cm^2 s^{-2} average value in the region downstream where eddy activity was weak (between 35°E to 40°E and 52.5°S to 54°S; Figure 3.2a). Vigorous currents dominated the first part of the deployment in the high-EKE region near the standing meander (yeardays 120-155), which presented challenges for keeping the autonomous platforms together (Figure 3.2c). In the low-EKE region downstream, during the latter portion of the deployment (yeardays 170-206), the gliders sampled across at least one coherent eddy and the gliders and float remained in close proximity (Figure 3.2c). Throughout the sampling period, the air-sea heat flux was characterized by net surface cooling that led to a slow thickening of the mixed layer; details of the surface forcing are provided in Figure 3.3.

Mean hydrographic properties computed from Argo float observations (Roemmich and Gilson, 2009) and measurements from the I06S repeat transect at 30°E show the dominance of the PF in setting large-scale tracer distributions in this region (Figure 3.4). Located at approximately 51°S, the PF is associated with a region of outcropping density surfaces. In the upper 400 m of the water column, the PF acts as a barrier to mixing between warmer waters to the north and cooler waters to the south that have a temperature minimum at a depth of 150-200 m (Figure 3.4a). The PF also separates southern, salinity-stratified waters from temperature-stratified waters to the north (Stewart and Haine, 2016). The salinity distribution shows evidence of subduction of fresher waters along density surfaces at the core of the PF, illustrating that on large scales, this region is associated with ventilation of intermediate waters (Figure 3.4b). Patterns in backscatter mirror the temperature distribution, with colder waters to the south showing a local minimum in backscatter near 150 m depth and the PF marking the southern boundary of high surface backscatter values to the north (Figure 3.4d).

The core of the PF is associated with a local weakening of the stratification at the base of the mixed layer, which likely enables subduction in this region (Figure 3.4c). Near the PF, stratification at the base of the mixed layer is strongest and the MLD itself shallowest at the end of the austral summer (March), as a result of the stratifying effects of sea ice melt and increased solar radiation (Giddy et al., 2021). During austral fall and early winter (April-July), stratification at the base of the mixed layer decreases, corresponding to a reduction in the maximum vertical

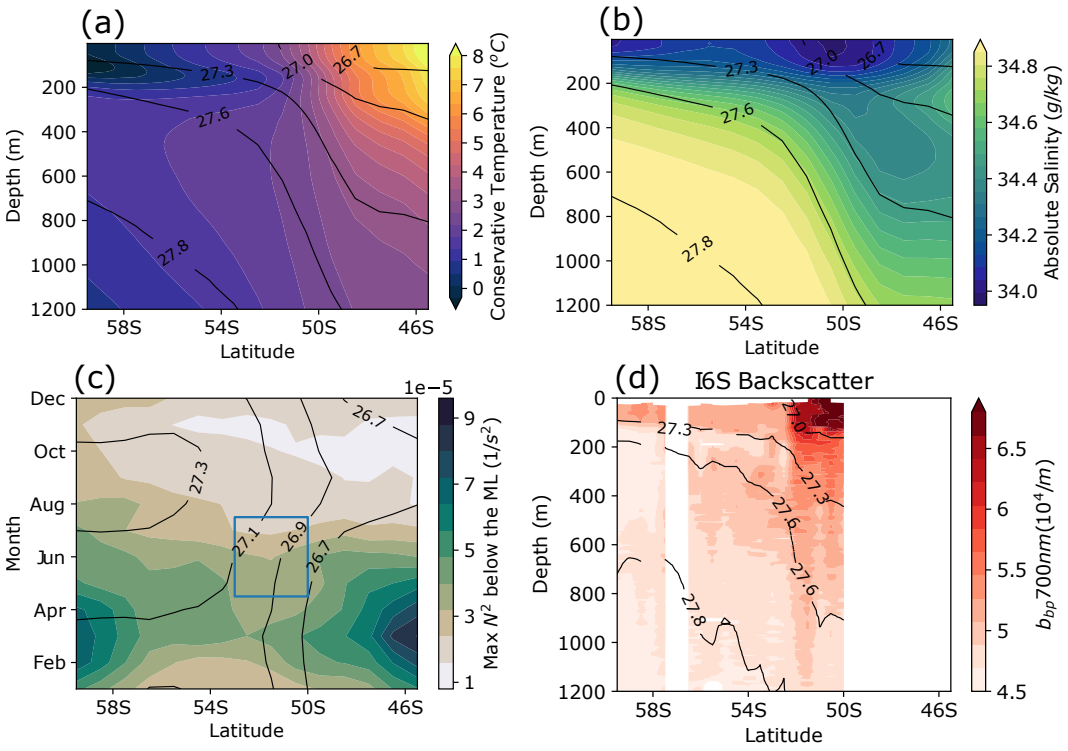

Figure 3.4: Hydrographic properties at 30°E.

Depth vs latitude plots of (a) conservative temperature (°C) and (b) absolute salinity (g kg^{-1}) at 30E from the Roemmich and Gilson, 2009 climatological mean. (c) Hovmoller plot of the maximum N^2 observed below the base of the mixed layer (ML), with the time and meridional extent of the glider sampling shown by the blue box, also from Roemmich and Gilson, 2009. (d) Depth-latitude plot of de-spiked backscatter data collected during I06S (2019); note the different latitude axis range in this panel. The σ_0 surfaces are shown as black contours, with panel (c) showing contours of surface σ_0. White space in panel (d) denotes a lack of data.

stratification (Dong et al., 2008). The autonomous platforms sampled during this weakening of the stratification in austral fall, which is also consistent with the surface forcing over the deployment period (Figure 3.3).

High-resolution physical and biogeochemical observations

Despite their relative proximity, the distributions of temperature-salinity ($\theta - S$) values measured by the float and by the gliders differ significantly. Throughout the deployment, the float sampled a relatively tight $\theta - S$ relationship, reflecting properties of the PF core waters (temperatures between 2°C and 2.5°C; Figure 3.5a). This suggests the float's trajectory was Lagrangian to good approximation, despite profiling vertically. While the gliders spent a large portion of time sampling within

the PF core waters as well, they also observed water masses sourced from north of the PF (with higher SSH and temperatures warmer than 2.5°C) and from south of the PF (with lower SSH and temperatures colder than 2°C). The gliders sampled a larger range of water mass properties during the first part of the deployment, corresponding to the high-EKE region (Figure 3.5b). Despite our best efforts to keep the gliders close to the float during the deployment, the platforms did not sample identical water masses over the duration of the mission. In some places this reflects the strong frontal currents and associated abrupt changes in water properties, although the platforms were geographically distant at certain times as well (Figure 3.2c). In fact, the gliders at times sampled "southern-sourced" waters based on hydrographic properties despite being physically well north of the float (Figure 3.2b, *e.g.* yeardays 130-150) – a signature of lateral stirring across the PF.

Gaps in $\theta - S$ space found in the distribution of hydrographic properties are indicative of multiple small-scale fronts (Naveira Garabato et al., 2011). This frontal structure is also supported by consideration of the local SSH field along the path of the gliders. Multiple minima in the frequency distribution of SSH are indicative of the gliders sampling across more than one frontal jet (Sokolov and Rintoul, 2009; Thompson and Sallée, 2012). In the high-EKE region early in the study period, the gliders sampled across several water masses separated by multiple fronts (Figure 3.5b,c). This frontal structure is highlighted further in Figure 3.8a, which shows that $\theta - S$ properties are correlated with SSH in the high-EKE region. In the standing meander region, mesoscale eddies may form and enclose water properties from either side of the front (Roach et al., 2016; Thompson and Sallée, 2012). This makes it difficult to distinguish jets from eddies in the glider data, although the correlation between SSH and $\theta - S$ will primarily reveal mesoscale structure due to the resolution of the altimetry data. In contrast, in the low-EKE portion of the deployment, distinct water masses were only sampled when crossing eddies shed from the PF (Figure 3.5d). During this latter period, the low range of SSH values sampled, together with the quasi-Lagrangian nature of the float, suggest that the gliders and float both stay primarily within the PF core waters. Over the full deployment, the PF core waters were observed most frequently (Figure 3.5e).

The similarities and differences in tracer variability between the high-EKE and low-EKE regions is further illustrated by the representative depth-time series plots of physical and biogeochemical properties from one of the gliders (SG660) shown in Figures 3.6 and 3.7. Periods dominated by mesoscale variability are characterized

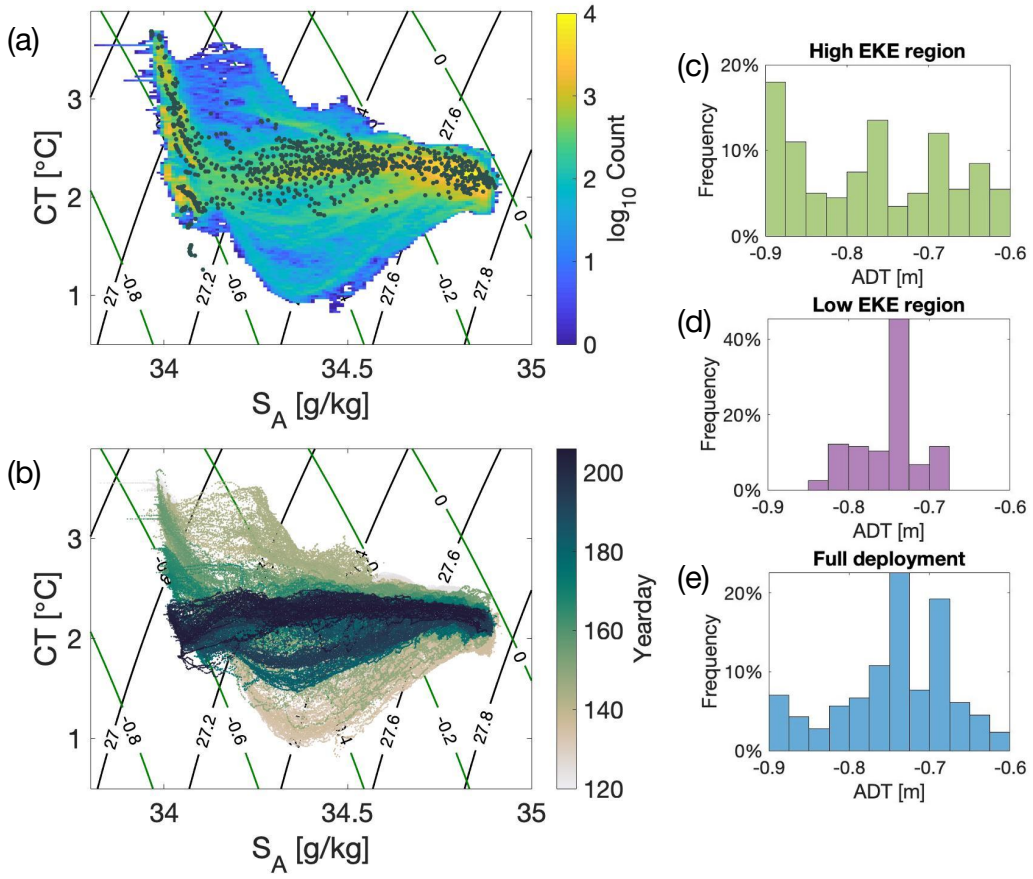

Figure 3.5: Hydrographic properties sampled by gliders and float.

(a) Conservative temperature-Absolute salinity diagram for all observing platforms over the full deployment colored by the frequency of observations collected by the two gliders with given CT-SA properties, using discretizations of $\Delta T = 0.02°C$ and $\Delta S = 0.01$ g kg^{-1}. Gray points are from the BGC-Argo float during the period April 29 - July 25, 2019. (b) Conservative temperature-Absolute salinity diagram colored by the yearday of the observation made by the two gliders. Black contours show potential density [kg m^{-3}] referenced to the surface, and green contours show spice [kg m^{-3}] referenced to the surface. Histograms of the absolute dynamic topography [m] (sea surface height) along the path of the gliders in (c) the high-EKE region (yearday 120-155), (d) the low-EKE region (yearday 170-206), and (e) the full deployment. Made from the joint data of SG659 and SG660.

by homogeneous properties in the upper 500 m of the water column as well as curvature in the isopycnals that is anti-correlated with SSH, for example during yeardays 140-145 (Figures 3.6a, 3.7a,b). Correlated variations between the vertical displacement of isopycnals and SSH are not observed to the same extent in the low-EKE regime, although the signature of a mesoscale eddy is present in the tracer observations collected between days 187-194 (Figure 3.6e-h). Higher frequency

and finer scale variability also occurs at the typical glider sampling scale, O(<1 day, <10 km), throughout the time series. This submesoscale variability is enhanced along the periphery of the mesoscale structures, consistent with increased strain in these regions (Brannigan, 2016; Siegelman, 2020). These features are particularly noticeable in temperature (Figure 3.6a,e), which acts as a passive tracer below the mixed layer, as well as in oxygen and optical backscatter (Figure 3.6c,g and d,h). Outside of the coherent mesoscale features, in what is sometimes referred to as the "submesoscale soup" (McWilliams, 2016), fine-scale tracer variability appears as horizontal layers, primarily in the high-EKE region (Figure 3.6a,c,e,g). Notably, the MLD is more variable in the high-EKE region, shoaling particularly at the edges of mesoscale eddies, and then stays relatively constant in the low-EKE region (black line in Figure 3.6a,b).

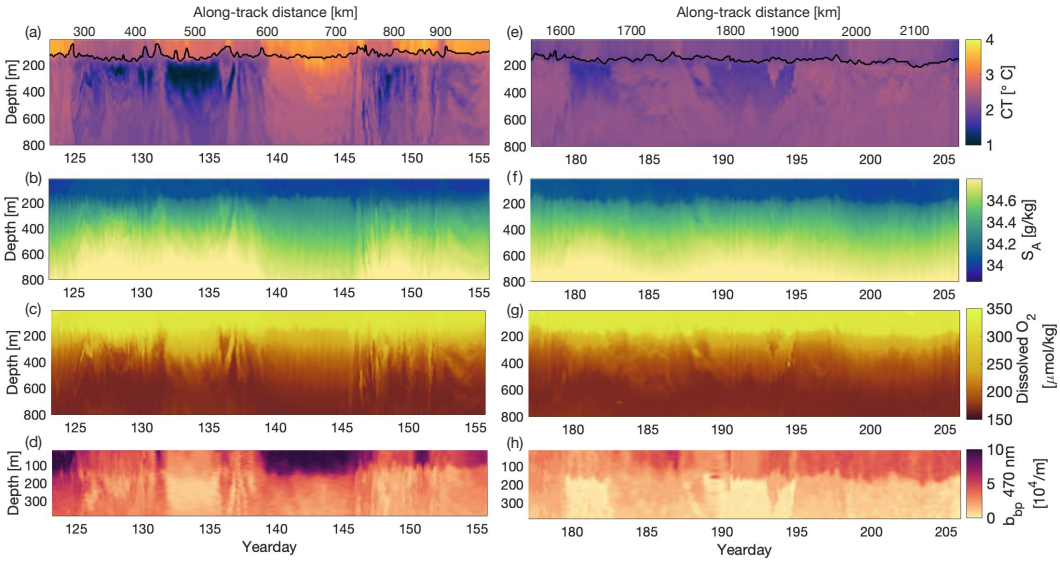

Figure 3.6: Glider tracer sections.

(a) conservative temperature [°C], (b) absolute salinity [g kg^{-1}], (c) dissolved oxygen [μmol kg^{-1}], and (d) backscatter at 470 nm [10^4 m^{-1}]. (a-d) from the high-EKE region (yeardays 120-155). (e-h) Same as in panels (a-d) but for low-EKE region (yeardays 177-206). Black line in panels (a) and (e) designates the mixed layer depth. Color bars apply to both left-hand and right-hand panels. Note change in depth axis for (d) and (h) compared to the other panels.

The optical backscatter distribution is closely correlated with temperature, with warmer temperatures associated with higher backscatter values (Figure 3.6d,h, 470 nm wavelength; sections of the 700 nm backscatter are similar but not shown). The temperature-backscatter relationship is consistent with the large-scale distribution observed during the I06S cruise (Figure 3.4d), suggesting that in both of these

properties, stirring cascades variance to smaller scales. An compelling feature of both the temperature and backscatter data is the non-monotonic vertical distribution, with the presence of prominent low anomalies located just below the mixed layer in the high-EKE region, sandwiched between higher values above and below (yeardays 127-132 and yeardays 145-150, between 150 m to 250 m). The temperature minima could be explained as a remnant of cold Winter Water that is capped in the summer by a warmer surface layer. In contrast, the backscatter mimima must arise from lateral or along-isopycnal advection. For instance, this feature could arise from the subduction of cold surface waters with low backscatter sourced from south of the PF. Notably, the backscatter minima at the base of the mixed layer (at approximately 150 m) only occurs in the high-EKE region, even though in the downstream region backscatter has a similar correlation with temperature at mesoscales (see mesoscale features over yeardays 132-135 and 187-195).

There is generally strong stratification at the base of the mixed layer throughout the deployment, which may limit exchange between the surface boundary layer and the ocean interior (Figure 3.7c,g). However, in the high-EKE region, the glider encountered intermittent periods of weakened upper ocean stratification collocated with the edge of strong mesoscale features. Although there is little evidence for coherent boluses of weakly stratified, low PV waters in the interior, high PV waters with strong stratification are observed to intrude into the mixed layer in the high-EKE region (*e.g.*, yeardays 125, 132, and 136; Figure 3.7d,h). The advection of high PV waters towards the surface is reminiscent of the tracer distributions associated with upwelling induced by anticyclonic eddies in the model-based study of Brannigan, 2016 (their Figure 2).

The complicated three-dimensional circulation that the gliders sampled along their trajectories motivates a consideration of biogeochemical distributions in temperature-salinity space as well as geographic space. Optical backscatter distributions, despite the intricate variations along the gliders' trajectories (Figure 3.6d,h), are largely shaped by the frontal structure in this region, with elevated backscatter values found north of and in the core of the PF and considerably lower backscatter values to the south (Figure 3.8c). Regions with high surface backscatter values do not all have the same vertical distributions; backscatter values are elevated to much greater depths and density classes for those waters associated with the core of the PF (Figure 3.8c,d). This suggests that subduction of water with high backscatter values (and potentially high POC) is linked to specific water masses and water mass formation

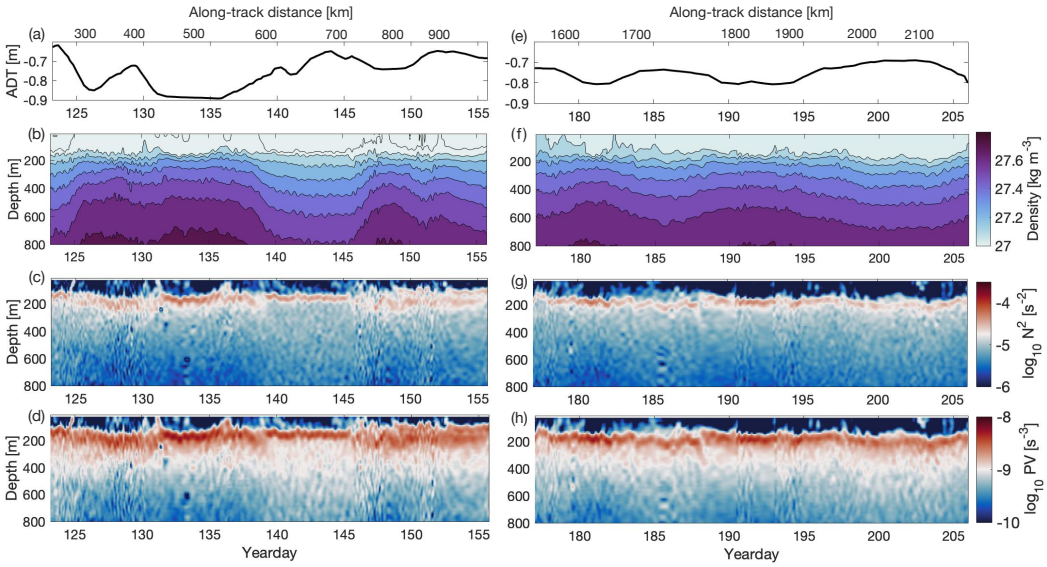

Figure 3.7: Glider derived tracer sections.

(a) absolute dynamic topography [m], (b) potential density [kg m^{-3}], (c) vertical buoyancy gradient, N^2 [s^{-2}], and (d) Ertel Potential Vorticity (PV) [s^{-3}]. (a-d) from the high-EKE region (yeardays 120-155). (e-h) Same as in panels (a-d) but for low-EKE region (yeardays 177-206). Color bars apply to both left-hand and right-hand panels.

processes.

The distribution of AOU also shows distinct behaviors between the different frontal regions. South of the PF core waters, contours of AOU (in temperature-salinity space) are predominantly aligned with contours of spice (Figure 3.8b). The resulting gradient of AOU on density surfaces may arise from lateral advection as cold anomalies are correlated with low AOU/high dissolved oxygen anomalies. This suggests that these waters have recently been subducted to the south of the study region, since these density classes do not access the mixed layer in the float/glider observations. North of and within the PF core waters, contours of AOU are largely aligned with density contours, such that AOU increases with depth and density. Those density surfaces with low AOU anomalies south of the PF have higher AOU values north of the PF, suggesting that recently ventilated waters are localized to the PF.

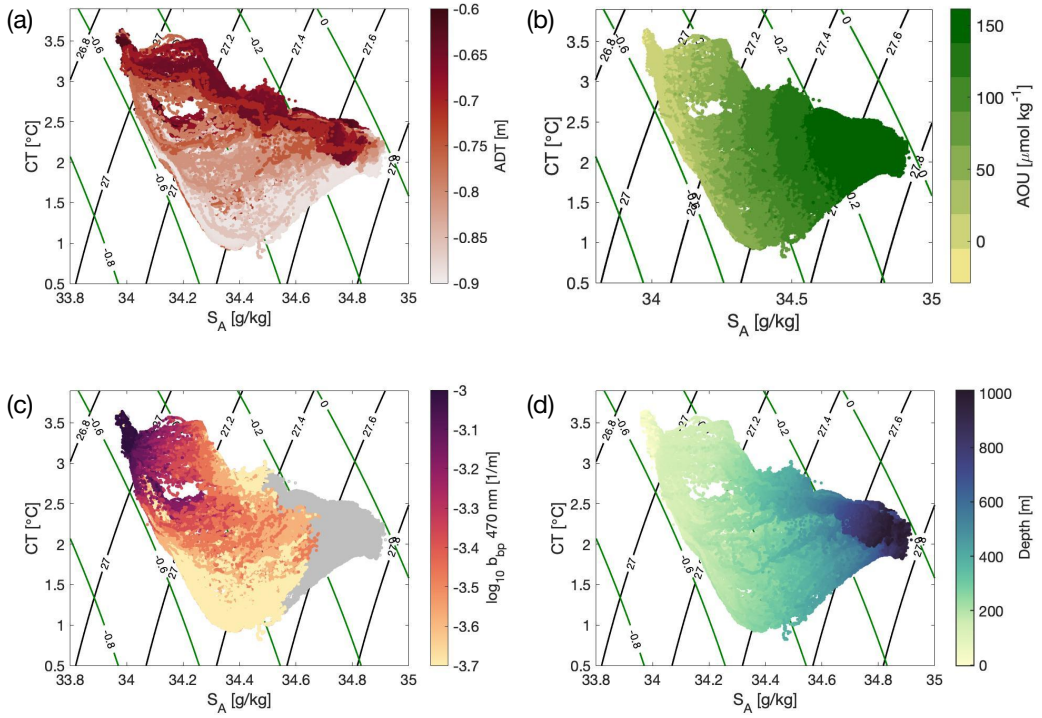

Figure 3.8: Distribution of tracers in the standing meander region.

(a) Absolute dynamic topography (SSH) [m] for each glider profile, (b) apparent oxygen utilization (AOU) [μ mol kg^{-1}], (c) $\log_{10} b_{bp}$ at 470 nm [m^{-1}], and (d) depth [m]. Gray points in the backscatter plot represent data between 400-1000 m where temperature, salinity, and oxygen measurements were collected but biogeochemical properties were not. In all panels, black contours show potential density [kg m^{-3}] referenced to the surface, and green contours show spice [kg m^{-3}] referenced to the surface. Made from the joint data of SG659 and SG660.

Submesoscale structures

Submesoscale motions are typically enhanced in the ocean surface boundary layer due to reduced stratification and the potential for frontogenesis (McWilliams, 2016; Thomas et al., 2008). Characterization of mixed-layer frontal structure has been a common method for assessing the potential for submesoscale motions and instabilities (Thompson et al., 2016), with previous studies showing that the statistical properties of the mixed layer can change over relatively short spatial scales (Viglione et al., 2018). In the SOGOS glider data, strong lateral buoyancy gradients in the along-track direction form in the mixed layer in the high-EKE region, as disparate water masses are stirred together (Figure 3.9). Both temperature and salinity anomalies in the surface layer work in concert to enhance the buoyancy anomalies. The compounding contributions from temperature and salinity intensify lateral buoyancy

gradients when these water masses are stirred by mesoscale eddies (for example, on yeardays 124, 139, 146, and 149; Figure 3.9b). Lateral buoyancy gradients have peak magnitudes and are most variable during the initial month of the deployment (Figure 3.9d). Strong surface buoyancy gradients are collocated with the edge of coherent mesoscale eddies or small-scale fronts, which are commonly associated with an intermittent shoaling of the mixed layer on the time scale of 1-2 glider dives (≈3-10 hours). The magnitude of the mixed-layer lateral buoyancy gradient weakens over the duration of the deployment (Figure 3.9d). This weakening could be caused by seasonal-scale changes in surface forcing (Figure 3.3a); however, the fact that the MLD remains relatively uniform (Figure 3.9c) suggests that it is more likely related to the reduction in vigorous stirring by mesoscale motions later in the deployment.

The prevailing paradigm for ventilation of the surface mixed layer by submesoscale motions has been along-isopycnal subduction at fronts, moving water masses across the base of the mixed layer (Freilich and Mahadevan, 2019; Omand et al., 2015; Ruiz et al., 2009). This view has been supported by consideration of tracer distributions in density space, in which tracer anomalies tend to be aligned along isopycnals, even if they have a significant vertical structure (see Fig. 3 in Lévy et al., 2018, for instance). In the glider observations, there are significant variations in spice and AOU along density surfaces, and anomalies are also often coherent across a broad range of densities, particularly below the mixed layer (Figure 3.10). The lack of obvious, coherent along-isopycnal subduction events indicates that other processes are active or that the subduction features occur at small scales so that gliders only observe them intermittently. Consistent with Figure 3.8b, AOU and spice anomalies are tightly correlated in regions associated with cold, southern-sourced waters. Anomalies in both spice and AOU echo the signatures of mesoscale features seen in Figures 3.6 and 3.7. At eddy peripheries or between eddies, most noticeable where there is a strong tilting of density surfaces (*e.g.* day 124 or 140), there are enhanced submesoscale variations (Siegelman, 2020). In these regions, both spice and AOU anomalies are coherent across a broad range of densities, even well below the base of the mixed layer, which suggests that stirring by (largely barotropic) eddies is likely the primary mechanism for generating this structure. Smaller-scale variations on density surfaces exist primarily in the high-EKE region, suggesting that in this region, deep density classes are accessed by filamentary structures that transport tracers vertically.

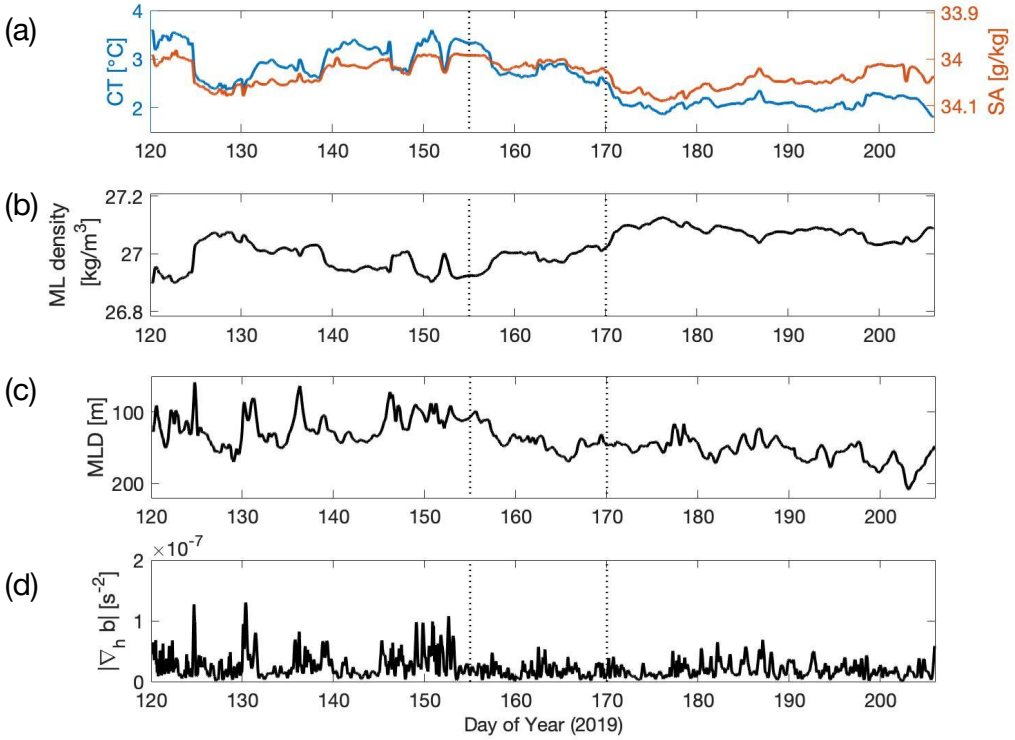

Figure 3.9: Mixed layer properties from glider.

(a) Mixed layer temperature (blue line) and salinity (red line) variations throughout the glider time series. The vertical axes are scaled by α (temperature) and β (salinity) so that variations in CT and S_A have equal effects on density. (b) Mixed layer density [kg m^{-3}]. Vertical axis has been scaled to the minimum and maximum contributions by the temperature and salinity presented in panel (a). (c) MLD as defined by a density difference criteria of 0.05 kg m^{-3} from a 10-m reference level. (d) Horizontal gradient of buoyancy in the mixed layer. Dotted line at yearday 155 denotes an end to the high-EKE region and the dotted line at yearday 170 denotes the start of the low-EKE region. Data from SG660.

Although tracer anomalies are not predominantly aligned with density surfaces, the signature of surface mixed layer-interior exchange is apparent nonetheless. In several locations throughout the deployment, low AOU (recently ventilated) waters intrude well below the MLD (Figure 3.10). Most notably, between yeardays 148-152, recently ventilated waters reach density surfaces typically associated with Upper Circumpolar Deep Water ($> 27.6\ kg/m^3$). In addition to the observations of low spice, low AOU waters extending to denser isopycnals, there is also evidence of deep, oxygen-depleted (high AOU) waters reaching across the base of the mixed layer (yearday 140), consistent with high-stratification waters intruding into the mixed layer at eddy peripheries in Figure 3.7c.

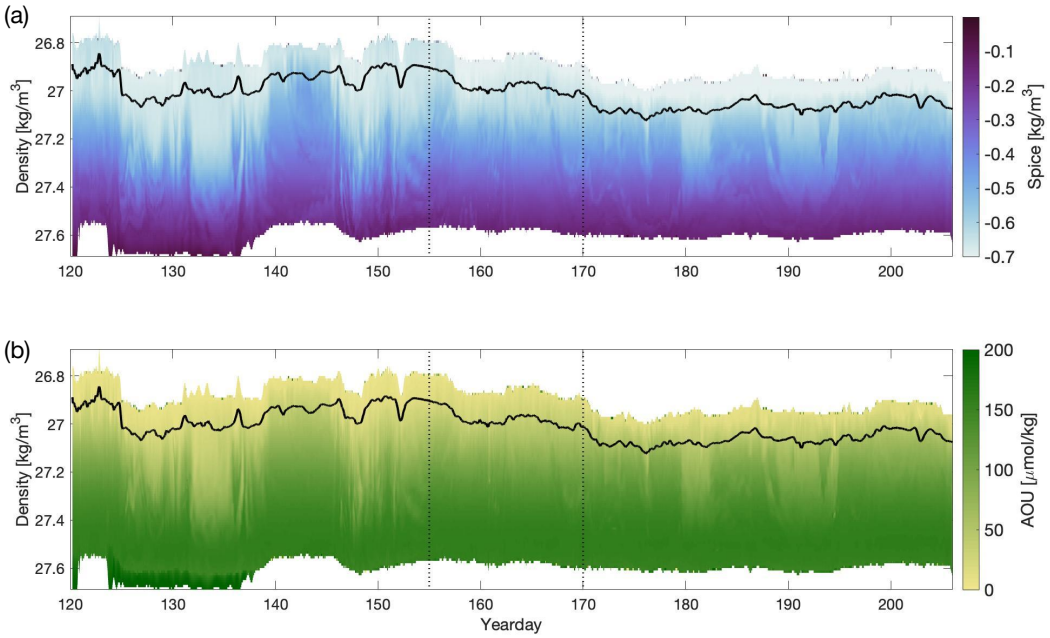

Figure 3.10: Glider tracer distributions on density surfaces.

Time series of (a) spice [kg m^{-3}] and (b) apparent oxygen utilization (AOU) [μmol kg^{-1}] from glider SG660 mapped on to potential density surfaces. Black line denotes the position of the mixed layer base. Dotted line at yearday 155 denotes an end to the high-EKE region and the dotted line at yearday 170 denotes the start of the low-EKE region. Data from SG660.

Biological signatures

While we have thus far focused on physical processes that generate the variability observed in both physical and biogeochemical tracer distributions, biological variability was also apparent in the glider and float data. Spikes in backscatter can be signatures of aggregated particulates (Briggs et al., 2020; Briggs et al., 2011). Typically the export of aggregates is dominated by gravitational sinking, rather than by active advective processes that contribute to the export of smaller particles (Boyd et al., 2019). The number of aggregated particles, counted by large spikes in the b_{bp}, is variable across the deployment but is often correlated with the concentration of backscatter in the mixed layer, consistent with the export process for large particulate aggregates being primarily one-dimensional (Figure 3.11a,b). The regions of highest backscatter at the surface are correlated with warmer waters sourced north of the PF (*e.g.* yeardays 120-122 and 130-140). While large aggregates may sink out of the water column, smaller non-aggregated particulate matter may be transported along isopycnals to intermediate depths (Dever et al., 2021), a process that highlights the impact of three-dimensional transport on tracer distributions.

The float backscatter data, which were collected to greater depth than that collected by the gliders, reveal that enhanced backscatter can exist at depths down to 600 m in the high-EKE region (not shown). Although the platforms did not follow identical pathways and backscatter processing between the platforms differ, the distribution of spikes in 700 nm backscatter from float WMO 5906030 is qualitatively similar to that determined from the gliders (Figure 3.11a). However, due to the 5-day sampling period of the float, the small-scale structure within the patterns in the glider backscatter spike data is absent in the float backscatter data, which can have a significant impact on longer-term mean values. Observing platforms that rely on sampling on the order of many days will miss this high-frequency variability, which provides information on particulate export from the surface ocean, especially due to submesoscale dynamics.

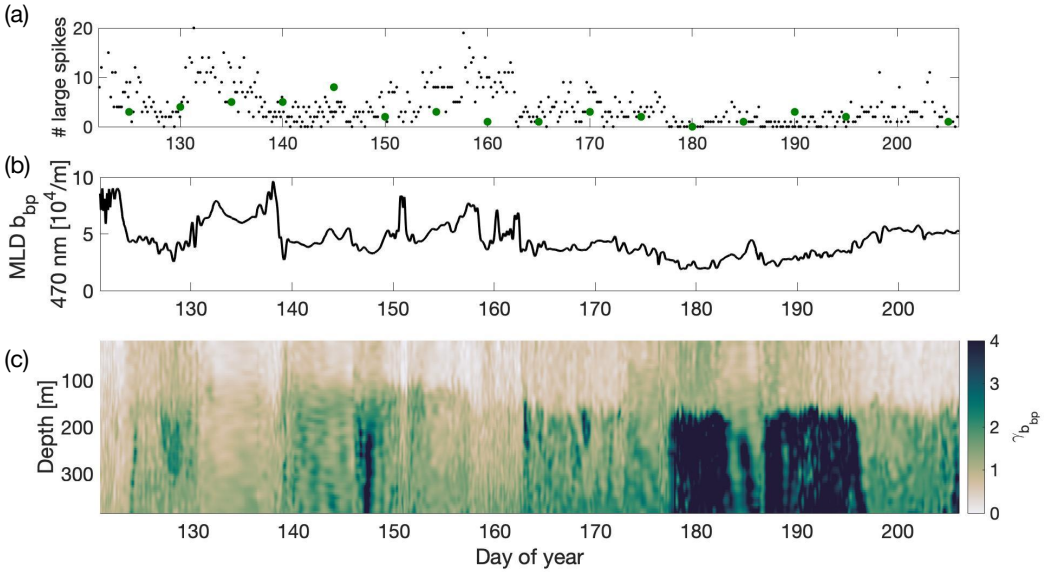

Figure 3.11: Optical backscatter signatures from glider and float.

(a) Black dots: number of large spikes in 470 nm backscatter below the mixed layer per each downcast and upcast of SG659. Green dots: number of large spikes in 700 nm backscatter in BGC-Argo float data from WMO 5906030. Note that only qualitative patterns should be considered as the sampling rates of the gliders and float were not the same. (b) 470 nm backscatter in the mixed layer from SG659. (c) Backscatter spectral slope (γ_{bbp}) from SG659. Figure made with SG659 due to potential errors in the 700 nm backscatter data from SG660.

Backscatter spectral slope ($\gamma_{b_{bp}}$), which was calculated using two wavelengths of despiked backscatter from $b_{bp}(\lambda) = b_{bp}(\lambda_0)\frac{\lambda}{\lambda_0}^{-\gamma_{b_{bp}}}$, has been shown to reflect the size distribution of suspended particles (Dever et al., 2021; Kostadinov et al.,

2009). Qualitatively, the spectrum of backscatter will flatten as the percentage of larger particles increases; a transition from large to small $\gamma_{b_{bp}}$ may thus indicate a transition into a more productive region with larger phytoplankton. Estimates from satellite observations of $\gamma_{b_{bp}}$ in the surface ocean of the Southern Ocean suggest values of 0.5-1.5 (Loisel et al., 2006), consistent with our glider estimates.

Ranging from 0 to 4, $\gamma_{b_{bp}}$ is generally low in the surface mixed layer (Figure 3.11c), suggesting a greater proportion of large-sized particles that are potentially diatoms, the dominant marine primary producers in the Southern Ocean (de Baar et al., 1999; Rousseaux and Gregg, 2014). Below the mixed layer, $\gamma_{b_{bp}}$ increases, particularly in regions where backscatter concentrations are low (*e.g.* yeardays 146-147, 178-196); here a larger proportion of small-sized particles are likely dominating the backscatter measurements. In general, the high-EKE region has a weaker vertical gradient in $\gamma_{b_{bp}}$ across the base of the mixed layer, suggestive of enhanced surface-interior exchange.

The particle composition distribution suggests plankton communities with differing compositions are intricately mixed in this localized region of high EKE in the Southern Ocean. The PF typically acts as a barrier to mixing of biological communities and is a known front in silicate, which has implications for the growth of diatoms (Freeman et al., 2018). However, the high EKE at standing meanders may allow plankton communities to be stirred into proximity and ultimately to mix. While these communities remain intact when transported within coherent mesoscale features (*e.g.* days 178-196 in Figure 3.11c), mixing of these communities occurs in filaments at the edges of eddies. Such mixing is especially prevalent in the high-EKE region, implying a regional hotspot for community mixing both in the surface ocean and at depth (Figure 3.11c).

3.5 Discussion

Cross-scale contributions to variability

Our understanding of the role of mesoscale and submesoscale processes in setting the distribution of biogeochemical tracers has been shaped by observations of organic matter subduction (Mahadevan, 2016; Stukel and Ducklow, 2017), as well as heavily-instrumented studies that tracked the transport of tracer anomalies between the surface ocean and the interior (Omand et al., 2015; Stukel et al., 2017). However, open questions remain about the relative contributions that processes at different scales make to setting these patterns. This is particularly true in the Southern

Ocean where observational surveys that resolve submesoscale features have been rare (Adams et al., 2017), and geographic regions or features that enhance export via small-scale subduction remain relatively unexplored.

Stirring by mesoscale eddies is known to produce filaments and anomalies of spice, AOU, and biogeochemical tracers at smaller submesoscales, particularly in regions where water masses with differing formation processes and community compositions are adjacent (Balwada, LaCasce, et al., 2021; Balwada et al., 2018; Smith and Ferrari, 2009). In the Southern Ocean, the PF supports large gradients in temperature and salinity that, via stirring by geostrophic turbulence, can produce a direct cascade of tracer variance to small scales, especially below the mixed layer. Indeed, the largest variance of tracers occurs on density surfaces below the mixed layer and can be explained primarily by stirring of large-scale gradients at the mesoscale, particularly within the high-EKE standing meander region (Figures 3.8 and 3.12). Furthermore, the majority of the observed tracer features at the submesoscale are not aligned along density surfaces. Thus, vigorous stirring along tilted density surfaces, ubiquitous in the Southern Ocean and particularly at the PF, must be critical in assisting with the export of biologically-relevant tracers from the surface layer to the interior. To this end, parameterizations that assume purely vertical sinking for particulate matter may misrepresent the subduction of organic matter in the Southern Ocean, particularly due to the three-dimensional structure of high EKE and enhanced stirring.

Yet, these observations also provide evidence that submesoscale motions are likely impacting surface boundary layer-interior exchange. This is particularly true for waters sourced from north of the PF, for which tracers such as AOU are more aligned with density surfaces (Figure 3.8b). Furthermore, high AOU and spice anomalies that reach across the base of the mixed layer occur almost exclusively along the periphery of coherent mesoscale features, as distinguished by co-variations in SSH and density surfaces. More broadly, stirring along density surfaces may also generate strong vertical gradients across the base of the mixed layer that then increase tracer fluxes due to turbulent vertical mixing at the submesoscale. Observations with high spatial and temporal resolution, sampled in a way that crosses submesoscale fronts at a near-perpendicular angle, are necessary for inferring ageostrophic vertical velocity w from existing parameterizations. While we were not able to provide a direct estimate of w with this dataset, there is strong evidence that upper-ocean submesoscale motions are playing a role in the subduction of surface waters, in a compact region in

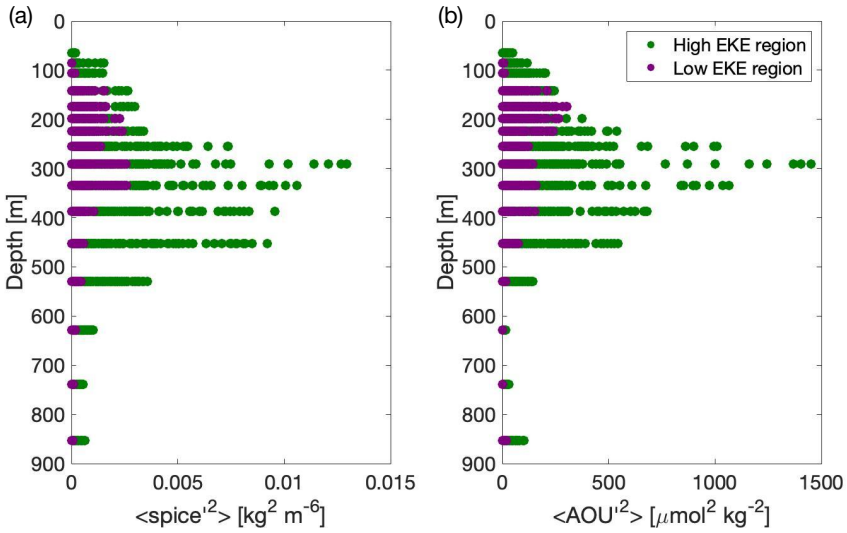

Figure 3.12: Variance in spice and AOU.

(a) Squared anomalies of spice in the high-EKE (green) and low-EKE (purple) regions on isopycnals, plotted on the average depth of each isopycnal. (b) Same as in (a) but for AOU. Individual points are the squared difference of spice (or AOU) at a point and the running mean (50 km) of spice (or AOU) along the isopycnal. Joint data of SG659 and SG660.

the lee of topography. Our observations thus allow for the validation of models that predict enhanced vertical tracer exchange where submesoscale dynamics are active. Ultimately, because features at the submesoscale are shaped by the mesoscale, the coupling of these scales plays an important role in shaping the tracer gradient, with submesoscales having a more prominent role in enabling exchange across the base of the mixed layer and mesoscales shaping tracer distributions at depth.

Isolating physical mechanisms responsible for tracer distributions becomes challenging when constrained solely by vertical profiles from floats that sample every O(10 days). Higher-resolution glider measurements, which sample scales of O(hours, 1 km), provide greater insight into anomalies resulting from mesoscale stirring and active submesoscale processes, which may be either misclassified or entirely absent in typical float profiles. Figure 3.13 shows how the BGC-Argo float and the gliders sampled around the edge of a mesoscale eddy in the low-EKE region of the deployment. The quasi-Lagrangian float was advected cyclonically around the edge of the eddy, performing three purely vertical profiles. In contrast, the glider sampled across the edge of the eddy and crossed through a coherent, low-AOU anomaly that extended below the mixed layer to a depth of 400 m, likely indicative of waters recently subducted from the surface layer (Figure 3.13a). The feature was not clearly

observed by the float although the instruments were all within 20 km of each other (Figures 3.2c, 3.13b). In fact, both gliders crossed the mesoscale eddy edge, but only one observed the submesoscale subduction feature, highlighting the azimuthal variability around a given eddy. Llort et al., 2018 showed that, in high-EKE regions of the Southern Ocean, anomalies of spice and AOU at depth are regularly present in BGC-Argo float profiles and described a method to attribute such anomalies to submesoscale dynamics. Our data illustrate that an accurate interpretation of profiling float observations must account for the fact that small numbers of floats will not capture the full signature of the submesoscale, particularly because these instruments do not often cross eddy edges. To this end, parameterizations that assume purely vertical sinking for particulate matter may misrepresent the subduction of organic matter in the Southern Ocean, particularly due to the three-dimensional structure of of high EKE and enhanced stirring.

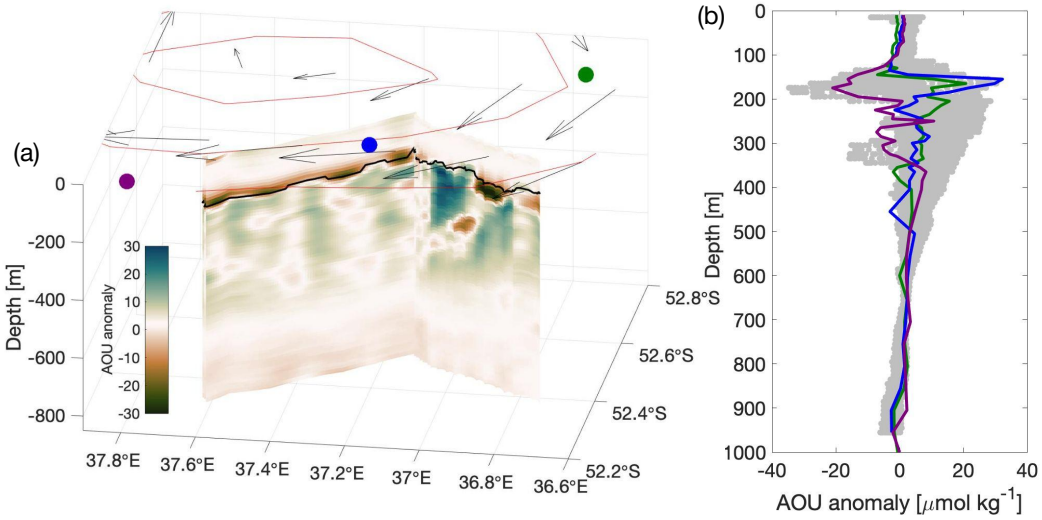

Figure 3.13: AOU anomalies in glider and float data in a mesoscale eddy.

(a) Curtain figure of the AOU anomaly from the mean value at each depth from SG660 between yeardays 187-193. MLD is plotted as a black line. Sea level anomaly from day 190 is given by the red contours; the arrows show the geostrophic velocity with peak speed of (20 cm s^{-1}). Green, blue, and purple lines represent the locations of vertical profiles done by the BGC-Argo float on yeardays 185, 190, and 195, respectively. (b) AOU anomaly with depth for the glider (gray) and each of the 3 float profiles with the same colors as in panel (a). Note the float did every other profile to 2000 m but only the upper 1000 m are shown.

The case for Southern Ocean ventilation hotspots

Standing meanders of the Southern Ocean, characterized by high EKE and rates of strain, may play an outsized role in the export of organic matter due to their ability to sustain a persistent and vigorous mesoscale eddy field that provides a source of frontogenesis and catalyzes strong submesoscale motions that enhance vertical velocities and fluxes (Siegelman, 2020). Our data set is unique in that the gliders and float sampled regions of both strong and weak mesoscale strain, corresponding roughly to the first and second halves of the deployment, respectively (Figure 3.2a). Evidence for subduction at the submesoscale is greater in the high-EKE portion of our study region, where larger lateral buoyancy gradients, stronger tracer variability, and high oxygen values penetrating deeper into the water column are all diagnostics consistent with enhanced submesoscale activity (Figures 3.9 and 3.10). The MLD is both shallower on average and more variable in the high-EKE region (Figure 3.9), potentially demonstrative of shoaling as a result of mixed layer instability (du Plessis et al., 2017; Thompson et al., 2016; Viglione et al., 2018.) This observation is also consistent with numerical models, such as Balwada et al., 2018, that find that mixed layers are shallower downstream of a topographic feature where an active submesoscale field is present. Finally, the deepest penetration of the backscatter data away from the surface is found within the core of the PF, associated with the strongest frontal structure (Figure 3.8c).

Further evidence for localized ventilation in the standing meander is the stronger along-isopycnal tracer variance in the high-EKE region directly in the lee of topography than in the low-EKE region downstream (Figure 3.12). The difference in tracer variance between the high- and low-EKE regions is particularly apparent on isopycnals with average depths of 250-500 m. At times these isopycnals reach close to the base of the mixed layer, and thus this variance can influence the exchange of tracers between the interior ocean and the surface layer. The peak in variance is deeper in the high-EKE region (350 m) compared to the low-EKE region (250 m). In contrast to these mid-depth isopycnals, anomalies are low on isopycnals found in the surface ocean because of the homogenizing nature of the mixed layer (the average MLD is 140 m). These tracer variance characteristics suggest that vigorous stirring by coherent eddies within the standing meander plays a dominant role in setting tracer distributions and gradients in the interior ocean. Furthermore, the peak in tracer variance occurs at greater depths in the high-EKE region as compared to downstream, despite deeper mixed layers in the latter (Figure 3.12). While much of the tracer variance generation likely occurs through mesoscale stirring, injection

of anomalously low AOU, low spice waters from the surface is required to maintain the range of observed tracers.

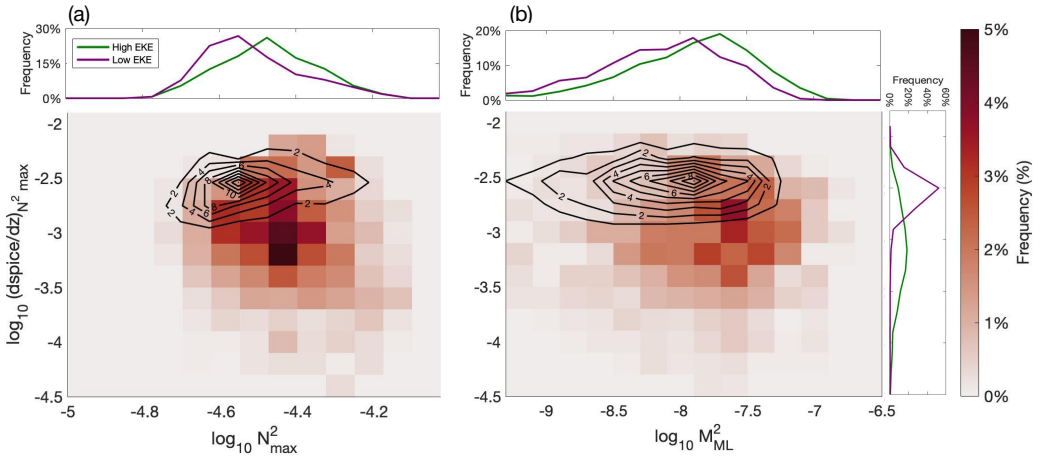

Figure 3.14: Joint probability distribution functions of buoyancy and spice gradients. (a) $\log_{10}$ maximum vertical gradient of buoyancy (N^2_{max}), and (b) $\log_{10}$ horizontal gradient of buoyancy in the mixed layer (M^2_{ML}) and with the $\log_{10}$ of the absolute value of vertical spice gradient at the depth of N^2_{max}. Colors show the distribution for the high-EKE region; contours give that for the low-EKE region. Values of the joint probability for the contours for the low-EKE region are labeled. The one-dimensional histograms show the the probability distribution of (a) $\log_{10}$ N^2_{max} and (b) $\log_{10}$ M^2_{ML} for the high-EKE region (green) and low-EKE region (purple). Made from the joint data of SG659 and SG660. Discretization: ΔN^2 = 0.075, ΔM^2 = 0.2, dspice/dz = 0.2.

While small-scale fluctuations in the stratification at the base of the mixed layer are observed by the glider (Figure 3.7c,g), overall there is only a slight difference in the maximum value of stratification (N^2_{max}) between the high-EKE standing meander and the low-EKE downstream region. In the high-EKE region, both N^2_{max} (Figure 3.14a) and lateral buoyancy gradients in the mixed layer (Figure 3.14b) are slightly stronger, but by less than a factor of 2. In contrast, substantial changes are found in the vertical tracer gradient across the base of the mixed layer (shown as a change in spice in the 10 m above and below the depth of N^2_{max} in Figure 3.14), with gradients within the high-EKE region reduced by almost an order of magnitude as compared to those in the low-EKE region. Weaker vertical gradients in tracers suggest that those waters were recently subducted below the mixed layer. While gradients of spice can possibly be impacted by seasonal or meridional changes, the signal of reduced vertical tracer gradients is also robust in AOU, which has a relatively constant value near the surface. Waters between the depth of N^2_{max} and

the depth of N^2_{max} + 200 m in the high-EKE region are substantially more likely to have lower values of AOU than those in the low-EKE region, suggesting these waters have been more recently ventilated and subducted below the depth of high stratification, potentially via active submesoscale processes (Figure 3.15). Whether this alignment of increased ventilation with higher EKE is a pattern that holds across the Southern Ocean remains an interesting open question.

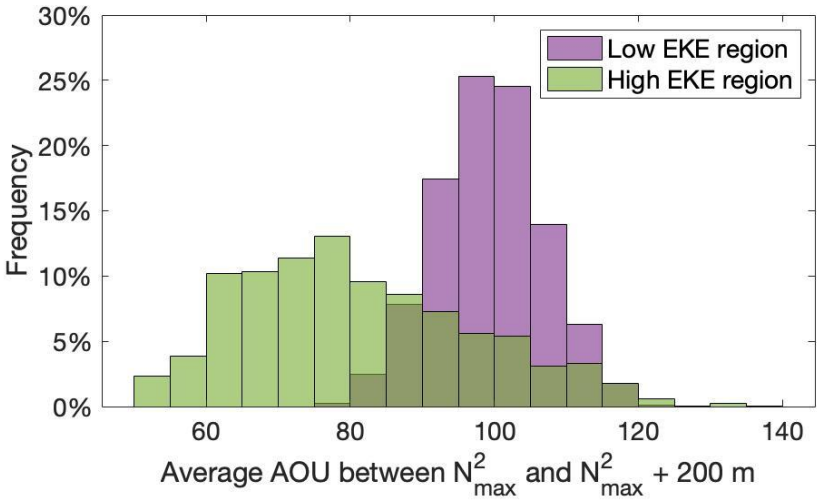

Figure 3.15: Probability distribution of ventilation parameters.

AOU [μmol kg^{-1}] between the depth of N^2_{max} and the depth of N^2_{max} + 200m. Green bars represent the high-EKE region and purple bars the low-EKE region. Made from the joint data of SG659 and SG660.

In this data set, there is only weak evidence for the subduction of low PV (weak stratification) anomalies into the interior. This can be contrasted with the intense surface boundary layer-interior exchange that has been observed in the wintertime North Atlantic (Thompson et al., 2016). This characteristic of the SOGOS data differs from a recent study by Bachman and Klocker, 2020, in which an extremely high-resolution simulation (1/120°) was employed to argue that topographically-steered jets produce localized regions of enhanced ventilation. These simulations, focused on the region around the Kerguelen Plateau, produced a strong stationary jet north of the plateau, with surface velocities and EKE variations similar to our study region. Focusing on the topographically-steered jet, Bachman and Klocker, 2020 suggested that a westerly wind stress can produce a destabilizing Ekman buoyancy flux that generates convective mixing and intense exchange with the interior (Thomas and Lee, 2005). Most diagnostics in this study do not extend into the standing meander region just downstream of the plateau. While we can not rule out the

possibility that a similar mechanism occurs as the PF passes directly over the SWIR, the float and the gliders all measure stratification levels at the base of the mixed layer that are much greater than one would expect if convective mixing was active. Our observations suggest instead that ventilation peaks as the jet becomes more variable and filamented in the lee of topography and mesoscale stirring intensifies.

Considering the SOGOS observations in the context of our current understanding of the Southern Ocean, a picture emerges where instabilities associated with topographically-steered jets give rise to an energetic field of mesoscale eddies. The jet itself has enhanced gradients in tracer properties that are then effectively stirred in the standing meander. This stirring strengthens horizontal surface buoyancy gradients, leading to an active submesoscale velocity field. The depth to which these submesoscale motions penetrate is difficult to determine from our observations but likely depends strongly on the stratification at the base of the mixed layer. During our study period, this stratification appears to be relatively strong due to the influx of freshwater and low mean wind stress. Intermittent, strong wind events (> 0.5 N m^{-2}) did occur several times over the glider deployment (Figure 3.3c), which may have acted to destabilize the mixed layer, similar to the results of Bachman and Klocker, 2020 or Giddy et al., 2021. However, even if the submesoscale tracer fluxes are localized to the surface ocean, they still provide a continuous source of recently ventilated surface waters that are effectively stirred by the mesoscale, generating fine-scale gradients along density surfaces. Thus, through a combination of mesoscale stirring and submesoscale fluxes in the surface boundary layer, exchange between the surface ocean and the interior may be enhanced.

Observations such as those described here, together with model simulations, have suggested that standing meanders in the ACC may play an outsized role in air-sea exchange as well as tracer exchange between the surface and interior ocean. Process studies have demonstrated that this exchange is dependent on dynamics at the mesoscale and submesoscale and that along-stream variability created by standing meanders can result in vital regions of subduction and ventilation. Enhanced vertical velocities and vigorous stirring result in increased tracer variability that can lead to highly localized ventilation of old waters; in turn, localized ventilation impacts air-sea fluxes due to a disequilibrium between the atmosphere and surface ocean carbon dioxide (pCO_2) concentrations. Year-round data from BGC-Argo floats have allowed for further investigation into the locations of carbon uptake and outgassing in the ACC. These float-based estimates show that the regions around the Polar

Front exhibit significant outgassing during autumn and winter, likely associated with the large-scale upwelling of old, carbon-rich waters (Gray et al., 2018). The development and deployment of unmanned surface vehicles has further expanded the collection of ΔpCO_2 concentrations across the atmosphere and surface ocean (Sutton et al., 2021). However, the role of localized regions of enhanced EKE has not yet been diagnosed using such methods, in terms of the effects on air-sea exchange of CO_2. Previous model-based work that considered the distribution and number of platforms needed to constrain air-sea fluxes in the Southern Ocean found that high-frequency variance dominated in topographically complex locations (Mazloff et al., 2018; Wei et al., 2020), suggesting that increased sampling rates in those regions would be a valuable tool for constraining Southern Ocean tracer budgets. Due to the potential importance of these regions in impacting air-sea fluxes, observing systems in the Southern Ocean should consider using an adaptive sampling strategy for these regions, increasing sampling rates when platforms enter these standing meanders. Higher rates of sampling in standing meanders of the ACC may lead to a more complete understanding of their role in the carbon cycle and also provide year-round data regarding strength of subduction and ventilation at the mesoscale and submesoscale.

3.6 Conclusions

Data from a pair of ocean gliders, deployed alongside a SOCCOM BGC-Argo float, are used to assess the scales of variability in physical and biogeochemical tracers both within and downstream of a major standing meander of the ACC's Polar Front. In both regions, variability in passive tracers is largest along the edge of coherent mesoscale eddies. However, the standing meander, marked by enhanced EKE and strain, exhibits enhanced lateral buoyancy gradients in the mixed layer, a more variable MLD, and evidence of stronger interior mesoscale stirring, as compared to the more quiescent downstream region. Despite similar mean vertical stratification in both parts of the deployment, vertical tracer gradients are nearly an order of magnitude weaker in the standing meander region, suggesting more efficient subduction of surface waters into the interior. While submesoscale motions are likely critical for carrying tracer anomalies across the base of the mixed layer, interior stirring effectively advects these tracers to depth in the standing meander.

The observations presented here confirm a series of recent high-resolution modeling studies (Bachman and Klocker, 2020; Balwada et al., 2018; Rosso et al., 2015) that highlighted the key role that the complex three-dimensional stirring occurs

downstream of the interaction of the PF with topography has on vertical exchange between the surface ocean and interior. These regions are characterized as having an active submeoscale flow field with vigorous restratification processes occurring in a region of high EKE. Filamentary structures that allow for the vertical movement of tracers impact the transport of organic matter into the interior ocean, as well as the ventilation of older waters found at depth in the Southern Ocean. There are a discrete number of standing meanders associated with high EKE along the path of the ACC, each of which is likely to be a key region of surface-interior exchange that impacts air-sea exchange and biogeochemical cycling. Our results highlight the need for improved focus on parameterizing flow-topography interactions in models with coarse resolution. Ventilation in the ACC's standing meanders is highly localized, typically spanning a region of only a few hundred kilometers, in which Lagrangian floats experience a short residence time, even with a 1000-m parking depth. To address the impact of standing meanders on large-scale air-sea carbon fluxes in the Southern Ocean, current and future observational systems should consider employing adaptive sampling in these regions.

Chapter 4

CROSS-FRONT VARIABILITY IN VENTILATION IN SOUTHERN DRAKE PASSAGE

This work is published in *Geophysical Research Letters* as "Controls on Wintertime Ventilation in Southern Drake Passage." (Dove et al., 2023).

4.1 Abstract

Drake Passage is a key region for transport between the surface and interior ocean, but mechanistic understanding of this exchange remains immature. Here, we present wintertime, submesoscale-resolving hydrographic transects spanning the southern boundary of the Antarctic Circumpolar Current and the Polar Front (PF). Despite strong surface wind and buoyancy forcing, a freshwater lens suppresses surface-interior exchange south of the PF; ventilation is instead localized to the PF. Multiple lines of analysis suggest submesoscale processes contribute to ventilation at the PF, including small-scale, O(10 km), frontal structure in water mass properties below the mixed layer and modulation of a surface eddy diffusivity at sub-50 km scales. These results show that ventilation is sensitive to both submesoscale properties near fronts and non-local processes, *e.g.* sea-ice melt, that set stratification and mixed layer properties. This highlights the need for adaptive observing strategies to constrain Southern Ocean heat and carbon budgets.

4.2 Introduction

More than 40% of anthropogenic carbon in the ocean has been taken up south of 40°S, making the Southern Ocean one of the primary regulators of global climate (Frölicher et al., 2015; Sallée et al., 2012). The position at which isopycnals outcrop at the surface in the Southern Ocean has a leading-order impact on climate as this determines the structure and strength of the overturning circulation, as well as the magnitude of air-sea fluxes, which together control ventilation rates of surface waters (Abernathey et al., 2016; Ferrari et al., 2014; Pellichero et al., 2018; Speer et al., 2000). Following Morrison et al., 2022, we refer to "ventilation" as any process, or combination of processes, that transfers surface waters and tracers into the pycnocline. Drake Passage is a key region for the formation of mode waters (Close et al., 2013; Naveira Garabato et al., 2009; Sallée et al., 2010) and the

ventilation of carbon (Sallée et al., 2012). Wintertime measurements of pCO_2 have, until recently, only been collected in Drake Passage, and thus processes governing exchange of carbon with the atmosphere here have had an outsized influence on the interpretation of carbon cycling across the Southern Ocean (Takahashi et al., 2009; Takahashi et al., 2012). This sampling bias may contribute to differences between estimates of air-sea CO_2 fluxes from climatology, autonomous platforms (Gray et al., 2018; Sutton et al., 2021), atmospheric inversion (Landschützer et al., 2015), and aircraft observations (Long et al., 2021).

The Antarctic Circumpolar Current (ACC) is dominated by several major fronts that result in sharp transitions of water properties, with these fronts delimiting boundaries between different water masses (Chapman et al., 2020; Orsi et al., 1995). Frontal jets contribute the majority of the ACC's zonal transport, but also act as barriers to mixing and cross-front exchange by reducing the efficiency at which mesoscale eddies can stir tracers (Ferrari and Nikurashin, 2010; Klocker et al., 2012; Naveira Garabato et al., 2011; Thompson and Sallée, 2012). The ACC's fronts additionally connect the interior ocean with the atmosphere through both upwelling of deep waters and subduction of surface waters. In particular, the Antarctic Circumpolar Current's Polar Front (PF) is a key location where the formation of intermediate and mode waters occurs, impacting carbon and heat exchange with the atmosphere (Morrison et al., 2022; Stukel et al., 2017). Previous work has typically not resolved small-scale processes that influence both ventilation and eddy mixing at strong fronts.

Mesoscale stirring and submesoscale motions in the ocean surface boundary layer can significantly alter upper-ocean stratification and exchange between the mixed layer and the thermocline (Klein and Lapeyre, 2009) with important implications for ocean biogeochemistry (Lévy et al., 2018; Mahadevan, 2016). Coherent mesoscale eddies impact tracer structure at horizontal scales of O(10–100 km). Meanwhile, submesoscale motions are characterized by length scales of O(1–10 km) and Rossby numbers of O(1), dynamical regimes where rotation and inertial forces are of comparable importance. Process-based modeling studies of the Southern Ocean have suggested that submesoscale motions play a critical role in determining vertical fluxes of heat (Rosso et al., 2014), mixed layer depths (Bachman et al., 2017), and exchange across the base of the mixed layer (Balwada et al., 2018), underlining the need to accurately represent these dynamics in global climate models. Numerical studies have also found a heterogenous distribution of submesoscale characteristics

across the Southern Ocean with recent observations highlighting that these dynamical transitions are often abrupt and intermittent. (Adams et al., 2017; Dove et al., 2021; du Plessis et al., 2017; du Plessis et al., 2019; Giddy et al., 2021; Viglione et al., 2018). Estimates of Southern Ocean carbon subduction based on mesoscale and coarser observations (Sallée et al., 2012) have highlighted spatial variability in the ACC at $O(1000\,\text{km})$ scales; our analysis here suggests that significant variations in these climatatically-relevant air-sea exchange and ventilation properties occur on much finer scales in localized regions.

We present a unique, high-resolution hydrographic data set from Drake Passage, acquired by an autonomous ocean glider during austral winter 2016, that permits assessment of how variability at scales smaller than mesoscale impact ventilation and mixing rates. This study contributes to growing evidence that submesoscale dynamics are spatially and temporally heterogeneous in the Southern Ocean, responding not only to local, mesoscale variability (Balwada et al., 2018; Dove et al., 2022; Dove et al., 2021; du Plessis et al., 2019; Viglione et al., 2018), but also to non-local processes, such as sea ice melt, that influence upper ocean stratification.

4.3 Data and Methods

Ocean glider data

Two Seagliders carried out meridional transects across southern Drake Passage from 10 May–20 August, 2016 as part of the ChinStrAP-2 (Changes in Stratification at the Antarctic Peninsula) field program (Figure 4.1). The gliders profiled in a V-shaped vertical pattern to a maximum depth of 1000 m, collecting temperature, salinity, and dissolved oxygen concentration data using a SeaBird unpumped CT-Sail and an Aanderaa optode. Optical backscatter at 532 nm was additionally measured to 300 m in the first third of the deployment (10 May–10 June) using a WET Labs ECO puck. Although two gliders were deployed in the field study, analysis from one glider (SG537) is shown here; characteristics are similar between the gliders, as seen in Figure 4.2 and Figure B.1. The mean separation between glider surfacings at the start and end of dives was 4.6 km (Figure 4.1a) with a standard deviation of 2.1 km.

The raw glider data were processed using the GliderTools toolbox (Gregor et al., 2019). The data were then mapped onto a regular grid with 5 m vertical spacing and 2.5 km horizontal spacing. The processing and gridding of the glider data is described in full in Text B.1. In this paper, we discuss the two northward transects

collected by one of the gliders; we term these the "June" transect (spanning 18 May–6 June) and the "July" transect (spanning 8 July–23 July; 4.1b). Data were processed using the Gibbs Seawater Toolbox (McDougall and Barker, 2011) and the EOS-80 neutral density package (Jackett and McDougall, 1997); we use conservative temperature (Θ), absolute salinity (S_A), and neutral density (γ^n), unless otherwise noted. Mixed layer depths (MLDs) were calculated with a density difference criterion of $\Delta\sigma_0 = 0.125$ kg m^{-3} from the surface (Monterey and Levitus, 1997) that was found by Viglione et al., 2018 to be most representative of MLDs in Drake Passage. Apparent oxygen utilization (AOU) is a tracer, with units of concentration, that removes the temperature dependence of oxygen saturation, and is defined $AOU \equiv [O_2^{sat}] - [O_2]$ (Ito et al., 2004). Low AOU values are used as a proxy for recent ventilation (Dove et al., 2022; Llort et al., 2018), as respiration in the ocean interior is an oxygen sink.

Mixing length theory (L_{mix})

Ferrari and Nikurashin, 2010 argued that mean flows can suppress lateral mixing by advecting tracers away from eddy-rich regions before stirring can cascade tracer variance to smaller scales. This effect was later quantified from observations (Naveira Garabato et al., 2011) using mixing length theory that describes a characteristic length scale over which a fluid parcel can move before exchanging properties with the background fluid. This analysis was focused on hydrographic sections across major fronts of the ACC at mesoscale resolution (~50 km station separation). Since waters of southern Drake Passage are salinity stratified, mixing lengths are calculated using conservative temperature, Θ, following:

$$L_{mix} = \frac{\Theta_{rms}}{\nabla_n \Theta_m}. \tag{4.1}$$

First, Θ is mapped from objectively interpolated pressure coordinates to neutral density space using an interval of $\Delta\gamma_n = 0.02$ kg m^{-3}. A horizontal running mean at 25 km scales produces a low-pass spatial-mean temperature field, Θ_m, from which a large-scale temperature gradient along neutral surfaces, $\nabla_n\Theta_m$, is calculated. Temperature anomalies are defined as deviations from this mean per gridded profile. The first baroclinic Rossby deformation radius at 60°S is ~20 km (Chelton et al., 1998), so this averaging provides a "mesoscale" mean field. The temperature root mean square, Θ_{rms}, is calculated as the standard deviation of temperature anomalies with a running mean of 5 km. This approach differs slightly

from Naveira Garabato et al., 2011, which used both a temporal and spatial mean. Θ_{rms} along each transect provides a realization of the variability at the submesoscale. Using average values from the mixed layer, the mixed layer Rossby deformation radius ($NH_{ml}f^{-1}$) is 3.4 km, suggesting 5 km averaging at least partially captures properties at submesoscale.

The mixing length can be combined with an eddy velocity, U_e, and a correlation coefficient, c_e, to estimate an eddy diffusivity, κ, using the relationship:

$$\kappa = c_e U_e L_{mix}. \tag{4.2}$$

An eddy velocity scale was not calculated from the glider data, but an estimate of eddy kinetic energy (EKE) can be determined from satellite-derived surface geostrophic velocity. In June and July 2016, the time-mean EKE in Drake Passage was 0.01 $m^2\ s^{-2}$, or $U_e \approx EKE^{1/2} = 0.1$ m s^{-1}, with no significant change over the study period. Following Naveira Garabato et al., 2011, we apply $c_e = 0.16$.

Characterization of the study site

Each glider transect traversed the Southern ACC Front (SACCF) and the PF, defined using both hydrographic definitions (Orsi et al., 1995) and ADT contours of -98.5 and -61 cm, respectively (Kim and Orsi, 2014). The ADT contour definitions match the crossing of the PF by the glider as defined by hydrography, the northernmost extent of 2°C water at 200 m (Figure B.2). Velocity sections were constructed by calculating the geostrophic shear from the glider density field and then referencing this velocity to the glider's depth-averaged current (DAC). DAC is calculated from glider trajectories using the difference between the glider's expected and actual surface location at the end of each profile and applying a glider flight model. The maximum observed geostrophic velocity of the PF was similar during the June crossing (49 cm s^{-1}) and the July crossing (42 cm s^{-1}; 4.1b,c), similar to velocities described in the literature (Firing et al., 2011; Foppert et al., 2016). The geostrophic component of the velocity field is resolved in the direction perpendicular to the glider path and therefore the inferred intensity of the PF is dependent on the angle at which the glider crosses the front. However, the angles at which the glider crossed the PF differed by only $\sim 10\%$ between the crossings.

During the glider deployment, the mean surface heat flux in Drake Passage from the ERA5 reanalysis European Centre for Medium-Range Weather Forecasts (ECMWF) was -50 W m^{-2}, (over the box bounded by 55 °S, 65 °S and 60 °W, 70 °W), consistent with wintertime heat flux in Drake Passage (Stephenson Jr. et al., 2012). The average

wind speed over this time period was 10.1 m s^{-1} with maximum winds reaching 21.4 m s^{-1} (Figure B.3). The winds are predominantly westerly, with a westerly wind stress of 0.1 N m^{-2} averaged over the deployment period.

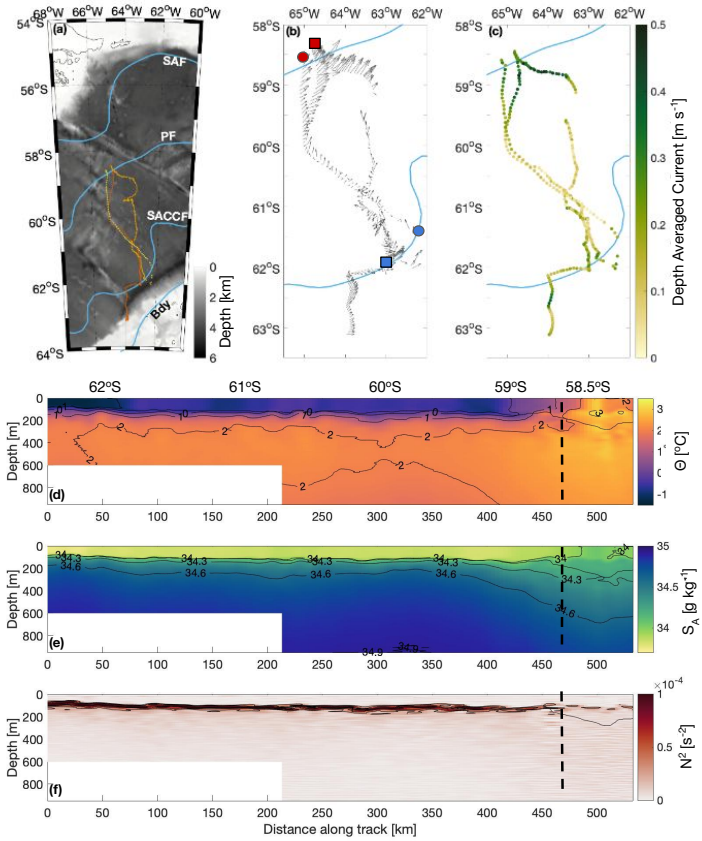

Figure 4.1: Geographic and hydrographic context of the ChinStrAP2 study region. (a) Map of the ChinStrAP2 study region. Individual glider surfacing locations are plotted as dots over ETOPO bathymetry, with red, orange, and yellow distinguishing separate transects. Fronts derived from AVISO altimetry and using the definitions of Kim and Orsi, 2014 are plotted in blue and labeled: Subantarctic Front (SAF), Polar Front (PF), Southern ACC Front (SACCF), Southern Boundary (Bdy). (b) Quiver plot of depth-averaged current (to 1000 m) derived from the glider path. Starting points of the transects discussed are denoted in blue with ending points in red, with the June transect marked with squares and July transect marked with circles. (c) Depth-averaged current speed. Glider data from the June transect, objectively mapped in pressure-distance space, showing (d) conservative temperature (Θ), (e) absolute salinity (S_A), and (f) vertical stratification (N^2). Dashed lines indicate PF crossing.

4.4 Results

Mixed layer properties

The PF marks a transition between salinity-stratified (south of the PF) and temperature-stratified (north of the PF) regions of the Southern Ocean (Stewart and Haine, 2016). The PF also marks a transition in upper ocean mixed layer variability. South of the PF, the mixed layer in 2016 was relatively cold and fresh, bounded below by a strong pycnocline (Figure 4.1d,e). This freshwater lens largely suppressed variations in the MLD: the mean and standard deviation of the MLD was 105.4 ± 13.0 m. On approaching the PF, the mixed layer deepened and the stratification at the base of the mixed layer weakened (Figure 4.1f). During the June crossing of the PF, the maximum MLD was 199 m. The maximum MLD deepened to 386 m during the July crossing (Figure B.4).

The freshwater lens south of the PF had an average temperature of −0.79°C and an average salinity of 33.67 g kg^{-1}. This temperature value is consistent with the average value measured by Expendable Bathythermograph (XBT) transects across Drake Passage in winter (Meredith et al., 2011; Sprintall, 2003). The observed fresh and cold values are consistent with sea ice melt (Meredith et al., 2011), which is notable because sea ice does not occupy this region of Drake Passage. Instead, this layer was likely sourced remotely, and based on the regional circulation, advected from the West Antarctic Peninsula and the Bellingshausen Sea.

Fine-scale structure of the Polar Front

A striking feature of the glider-derived high resolution hydrographic transects is the water mass structure reflected in temperature and salinity properties (Figure 4.2). The major fronts of the ACC support abrupt changes in hydrographic properties (Orsi et al., 1995) that can be diagnosed as gaps or low concentrations of observations in Θ/S_A space, when considering data with uniform horizontal sampling. Naveira Garabato et al., 2011 highlighted these distinctive, well-defined clusters of Θ/S_A curves at mesoscale resolution. Fronts appear as gaps in Θ/S_A space, while profiles within each inter-frontal zone fall within a narrow range of properties.

In Θ/S_A space, there are two clear regimes along the glider transects. South of the PF, the Θ/S_A profiles largely fall onto a single curve that has limited variability throughout the deployment (black lines in Figure 4.2a,b). Additionally, all of the profiles converge to the same temperature and salinity (1.6°C and 34.9 g kg^{-1}) at the base of the thermocline that represents the subsurface reservoir of Upper

Circumpolar Deep Water.

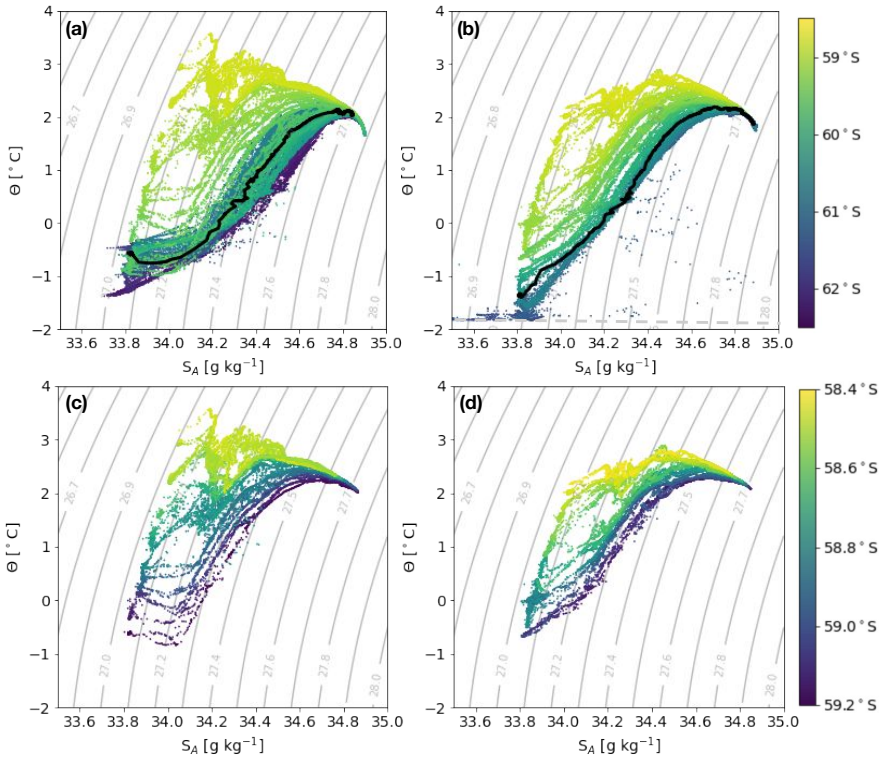

Figure 4.2: Conservative temperature (Θ)-absolute salinity (S_A) diagrams.

Panels on the left correspond to the June northward transect and panels on the right correspond to the July northward transect. Points are colored by the latitude at which they were collected. (a,b) show data for the entire transect, with black lines indicating representative glider profiles south of the PF; (c,d) show data only in the region immediately surrounding the PF (approximately 1 degree of latitude). Dashed line on (b) indicates the freezing point of seawater. Note the change in color scale range between upper and lower panels.

In contrast, surface waters at the PF span a larger range of Θ and S_A values (Figure 4.2c,d). The "PF crossing" waters are from glider profiles within 50 km of the PF for each transect. The distribution of Θ/S_A properties in the surface mixed layer along 27.05 kg m^{-3} is more continuous than the waters in the transition layer located between 27.05 and 27.25 kg m^{-3}. The Θ/S_A properties in this transition layer group into discrete "families" with distinct Θ/S_A properties (Figure 4.2c,d). Reminiscent of analysis of Θ/S_A at the mesoscale, gaps in Θ/S_A space over this narrow band of $\sim 1^\circ$ of latitude are indicative of submesoscale fronts that result in the propagation of discrete hydrographic properties below the base of the mixed layer, consistent with the important role of filaments in ventilation (Balwada et al., 2018; Dove et al.,

2021; Freilich and Mahadevan, 2021).

Mean-flow suppression at the Polar Front

We re-visit the approach of Naveira Garabato et al., 2011 with the ability to assess whether smaller-scale frontal structure impacts mixing properties. Across both the June and July transects, the hydrographic signature of the PF is located just north of 59°S (dashed black line in Figure 4.3a,b), consistent with a strongly elevated $\nabla_n \Theta_m$ (Figure 4.3c,d). The strong temperature gradient combines with mesoscale and submesoscale stirring to enhance temperature variance (Θ_{rms}) in the PF (Figure 4.3e,f). The distribution of Θ_{rms} captures smaller-scale variability, highlighting intermittent patches of enhanced variance south of the PF. Enhanced tracer variance found in density classes below the mixed layer south of the PF may represent tracer variance generated within the PF advecting southward along the upwelling limb of the overturning circulation, and is a topic of future work.

The estimated values of the mixing length, L_{mix}, range from 0 to >100 km (Figure 4.3g,h). Similar to property distributions in Θ/S_A space, there are two regimes. South of the PF, L_{mix} reaches its largest values. There is potentially a shift from large values of L_{mix} to smaller values from the June to July transects, although this limited temporal resolution make it difficult to infer whether this is related to a seasonal evolution or a shift in the mesoscale background properties. In contrast, in both transects, L_{mix} is suppressed at the PF, with the smallest values confined to a region <50 km wide. The vertically-averaged mixing length at the PF is L_{mix} = 11 km and L_{mix} = 10 km in June and July, respectively. These values are consistent with the findings of Naveira Garabato et al., 2011 from non-winter months and Foppert et al., 2016 from a full year, but augments these studies by directly resolving the inferred scale of the mixing length. From multiple crossings of the PF, our results imply that the PF acts as a barrier to upper ocean mixing, not only at mesoscales but also at submesoscales, in wintertime Drake Passage. Finally, using (4.2) we estimate κ at the PF as $\approx$170 m^2 s^{-1}, a value that corroborates that mesoscale stirring is not efficient at the PF.

Biogeochemical signatures of ventilation

The distribution of AOU in Drake Passage also supports spatial variations in ventilation. The June transect, representative of both transects, shows that low-AOU waters, indicative of recent ventilation, are confined to the mixed layer south of the PF. At the PF, the combination of a weakened vertical stratification and tilted

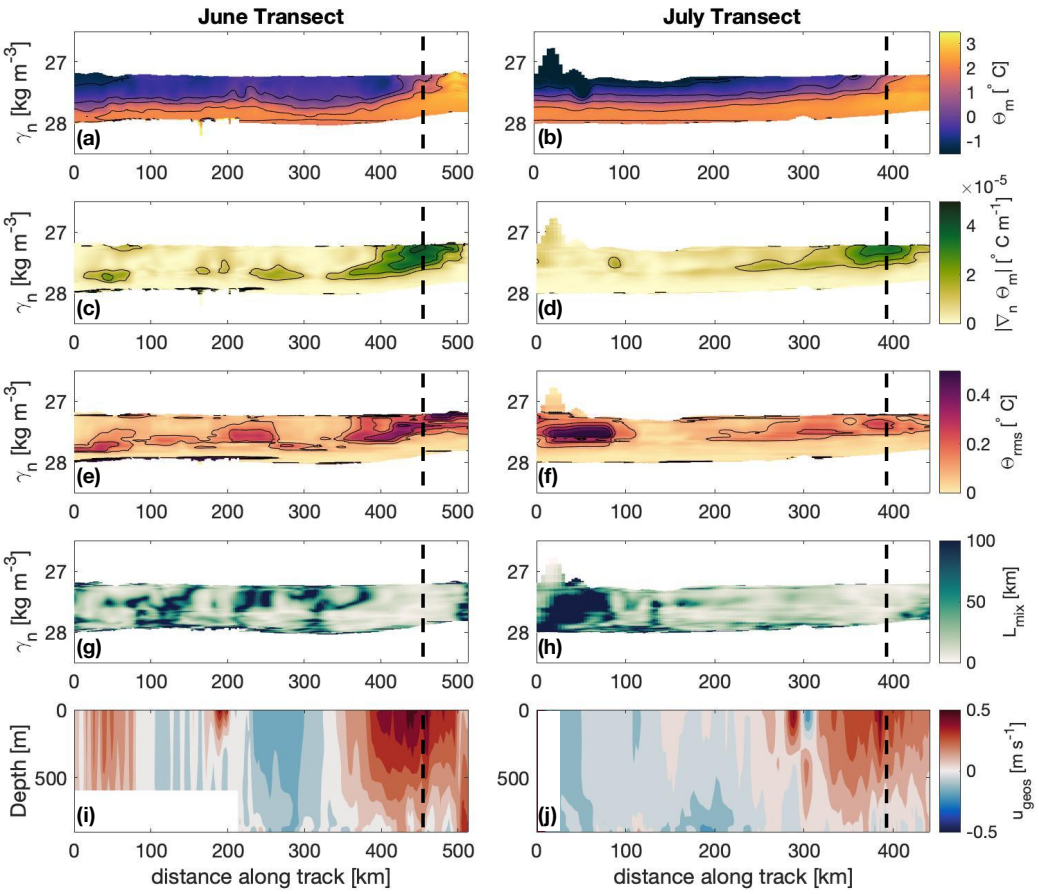

Figure 4.3: Mixing characteristics along two northbound glider transects spanning southern Drake Passage.

Panels (a–h) are plotted in distance-neutral density space, panels (i,j) are plotted in distance-pressure space. Left-hand panels (a,c,e,g,i) show observations from the June transect; right-hand panels (b,d,f,h,j) show observations from the July transect. (a,b) Smoothed temperature, Θ_m. (c,d) Large-scale temperature gradient along isoneutral surfaces, $\nabla_n \Theta_m$. (e,f) Standard deviation of temperature fluctuations, Θ_{rms}. (g,h) Eddy mixing length, L_{mix}.(i,j) Geostrophic velocity, U_{geo}. Black dashed lines indicate PF crossings.

isopycnals (Figure 4.4a) allows low-AOU waters to extend over 100 m below the base of the mixed layer. These low-AOU waters penetrate to depth primarily along isopycnals, suggesting a key role for rapid adiabatic advection or stirring in ventilation. These observations are consistent with numerical modeling studies that show that exchange at localized fronts can dominate larger-scale tracer fluxes (Uchida et al., 2019). MLD reaches its maximum extent in July and August in Drake Passage (Pellichero et al., 2017); therefore, we expect any tracer subducted at the Polar Front

is unlikely to be re-entrained to the mixed layer.

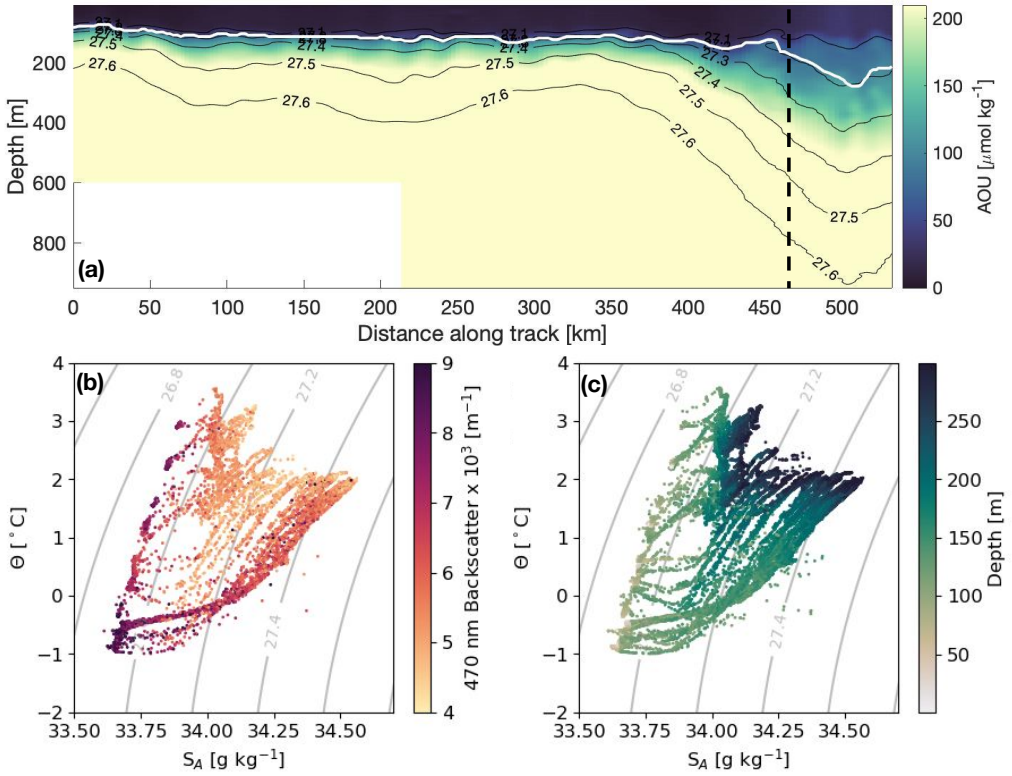

Figure 4.4: Biogeochemical signatures from the Polar Front.

(a) Distance-depth section of apparent oxygen utilization (AOU) for the June transect. Θ/S_A diagrams for (b) 532 nm optical backscatter and (c) depth. Optical backscatter was only measured to 300 m depth.

The high-resolution sampling capabilities of the glider permit an analysis of tracer variance at submesoscale resolution. The transition between a near-continuous distribution of Θ/S_A properties in the mixed layer to a discrete collection of Θ/S_A "families" in the transition layer provides compelling evidence that water is ventilated from the surface into the interior in small-scale filaments (Figure 4.2c,d). Specifically, the filamentary structure occurs in the same localized region near the PF where low-AOU waters penetrate to depth along isopycnals (Figure 4.4a), suggesting submesoscale processes contribute to the ventilation. We acknowledge that this ventilation may occur upstream of the glider observations, and there are fundamental limitations in documenting three-dimensional ventilation processes from individual transects.

Along-isopyncal variations in optical backscatter suggest a pathway for the transport of particulate organic carbon from the surface to the interior ocean. Waters with high

particulate content from the southern edge of the PF are preferentially found at depth within a density range that occupies a relatively small fraction of the surface water occupied by the gliders (Figure 4.4b,c). This is consistent with process-modeling studies that show subduction of near-surface waters is typically located along the dense side of fronts, which can further localize ventilated waters to mesoscale or smaller regions (Freilich and Mahadevan, 2021).

4.5 Discussion

The Southern Ocean has traditionally been identified as a region preconditioned for strong submesoscale activity due to strong surface wind and buoyancy forcing and a weak vertical stratification (Gille et al., 2022; Su et al., 2018). Yet, despite a strong wind stress and surface cooling (Figure B.3), the glider sections presented here show limited signatures of submesoscale variability and ventilation throughout southern Drake Passage. The fresh and cold mixed layer water properties found south of the PF indicate that non-local processes—e.g., the advection of waters influenced by sea ice melt from the West Antarctic Peninsula and Bellingshausen Sea—influence surface-interior exchange far from the melt location. In contrast, both tracer distributions (Figure 4.2) and tracer variance (L_{mix} calculation in Figure 4.3) suggest local small-scale, or submesocale, control on ventilation at the PF.

This work builds on the study of Naveira Garabato et al., 2011 in two important ways: first, our analysis was carried out using higher-resolution data (glider- vs. ship-based), and second, their analysis was carried out during summer and autumn months. The calculated mixing lengths, in regions where mean-flow suppression both is and is not active, have similar magnitudes, but the spatial scales of variability in Naveira Garabato et al., 2011 are much broader. Direct resolution of the suppressed mixing lengths of $O(10)$ km provide confidence that suppression of eddy stirring is strong in the upper and intermediate layers within the PF, and may even contribute to setting the small-scale distribution of water mass properties (Figure 4.2). Larger values of L_{mix} and weak isopycnal gradients are consistent with homogenization south of the PF, which may suppress the generation of strong submesoscale fronts.

Sallée et al., 2012 highlighted all of Drake Passage as a key site of mode water formation and tracer ventilation, based on coarsely-resolved *in situ* and remote sensing data. In recent years, higher resolution models and observations have indicated significant heterogeneity in surface properties, influencing ventilation and air-sea

fluxes, in regions as small as Drake Passage. The need to resolve and mechanistically understand these variations is particularly acute in Drake Passage since it is the principal location from which the Surface Ocean CO_2 Atlas (SOCAT) underway pCO_2 data is collected in winter (Bakker et al., 2016). Analysis of Southern Ocean Carbon and Climate Observations and Modeling (SOCCOM) biogeochemical-Argo float data (Gray et al., 2018) found stronger CO_2 outgassing south of the PF than previous estimates. While this discrepancy remains unexplained—in fact, Long et al., 2021 found strong carbon uptake south of 45°S—a potential for bias can arise if the region of weak surface-interior exchange in southern Drake Passage is extrapolated zonally. More broadly, the observations presented here highlight complications linked to extrapolating local measurements to other regions based purely based on geographical considerations, *e.g.* latitude. While the SOCCOM program has begun to identify regional variations in air-sea exchange (Prend et al., 2022), the abrupt spatial transitions in dynamical regimes that occur in the ACC imply that global estimates of air-sea fluxes will continue to have substantial uncertainties.

4.6 Conclusions

The ChinStrAP2 field campaign provided a unique dataset comprising several high-resolution transects of Drake Passage collected by ocean gliders in wintertime. These observations have offered new insight into the fine-scale structures of the PF. We find that the PF acts to suppress eddy mixing, even at scales below mesoscale eddies. We also reveal that submesoscale variability, including exchange across the base of the mixed layer, is suppressed south of the PF, even with strong wintertime surface forcing, due to enhanced vertical stratification that occurs due to meltwater water advected into the region from upstream. Ventilation over the study region is restricted to a narrow region ($\sim 1^\circ$ of latitude) near the PF. Here, the stratification weakens, the mixed layers deepens, and small-scale (submesoscale) water masses are found in the mixed layer pycnocline. The sensitivity of ventilation to both large-scale, even remote, processes as well as fine-scale frontal structure, suggests the need for scale-aware and adaptive future observing arrays to constrain Southern Ocean-wide heat, carbon, and nutrient budgets.

Chapter 5

VERTICAL STRATIFICATION AS A LEVERAGE ON AIR-SEA CARBON FLUXES

5.1 Introduction

The vertical structure of the world ocean is comprised of two main layers: a surface mixed layer which is continually exchanging heat and gases with the atmosphere, and the deep ocean, which is largely isolated from the atmosphere. Separating these two layers is the pycnocline, a region of strong vertical density stratification. The pycnocline typically acts as a barrier to mixing between the two layers. Differences in stratification at the pycnocline are a result of varying contributions of salinity and temperature to the density structure, which are shaped by surface fluxes – including from winds, freshwater input, and heat input – and mesoscale and submesoscale eddy processes. As a result, there is seasonal variability in pycnocline stratification, with stratification stronger in summer than in winter, as the mixed-layer deepening induced by the wintertime intensification of upper-ocean turbulence erodes the increased summer stratification (Buckingham et al., 2019). The Southern Ocean is traditionally viewed as a region of low stratification as a result of persistent along-front surface wind forcing (Gille et al., 2022; Thompson and Naveira Garabato, 2014), and the pycnocline is well associated with the stratification at the base of the mixed layer. However, global climatology demonstrates that stratification is highly variable across the Southern Ocean (Stewart and Haine, 2016). In addition, large differences in stratification have been observed in Drake Passage (Dove et al., 2023) and the marginal sea-ice zone (Giddy et al., 2021), demonstrating that differences in stratification can occur on relatively small regional scales. Stratification is rarely used as a dianostic and is potential source of bias in climate models, as heat and carbon uptake are strongly linked to models' stratification (Bourgeois et al., 2022; Haumann et al., 2020); however the mechanisms leading to this relationship have not yet been described. Notably, two models from the NOAA Global Fluid Dynamics Laboratory have significantly different modern-day density stratification, implying there may be discrepancies in parametrizations at the the mesoscale and submesoscale that both impact and are impacted by stratification.

The Southern Ocean is a region of both uptake of anthropogenic carbon and out-

gassing of "natural" carbon, with the Polar Front separating the northern region where uptake is dominant and southern region where outgassing dominates. There is a seasonal cycle to carbon fluxes, with outgassing particularly strong in wintertime due to deep mixed layers (Gray et al., 2018; Long et al., 2021). The source of the carbon that is outgassing south of the Polar Front is dissolved inorganic carbon (DIC) contained in Circumpolar Deep Water (CDW) that upwells in the Southern Ocean (Gruber et al., 2019; Talley, 2013). Upwelling CDW is characterized by high DIC and alkalinity due to its source waters, *i.e.*, North Atlantic Deep Water and return flows from the deep Pacific and Indian Oceans (Lovenduski et al., 2008; Sarmiento et al., 2004). The amount of high-DIC CDW that enters surface mixed layer is a major control on the amount of outgassing of carbon occurring from the surface mixed layer to the atmosphere. Strong stratification of the pycnocline may act as a barrier to the vertical exchange of waters between the surface and interior ocean and for vertical fluxes, while reduced stratification can result in comparatively strengthened fluxes (Su et al., 2018). Evidence from the Arctic and Patagonian Shelf indicate that local and non-local sea ice melt can have impacts on air-sea carbon fluxes and also phytoplankton bloom onset (Bianchi et al., 2018; Sejr et al., 2011).

The Polar Front (PF) acts as a physical barrier to latitudinal transport, with highly stratified waters resulting from non-local sea ice melt to the south of the PF, even in wintertime (Dove et al., 2023). However, the northerly extent of the PF varies on an annual timescale (Figure 5.1; Freeman and Lovenduski, 2016; Sprintall, 2003, 2008). Along with vertical stratification, the variability in the northward extent of the PF may shape which isopycnals are able to outcrop to the south, impacting how much high-DIC water reaches the mixed layer and the resulting outgassing. Numerical models traditionally do not fully capture the variability of the PF location and extent when calculating carbon fluxes (Pauthenet et al., 2018). Considering the latitudinal extent of the PF and the resulting enhanced northerly vertical stratification is necessary to predict long-term trends in carbon uptake at polar latitudes.

The aim of this work is to describe the role of mesoscale and submesoscale processes in transporting high-DIC CDW into the surface mixed layer and the impact of pycnocline stratification in constraining this ventilation process. While the preliminary work focuses on Drake Passage, these results have implications for understanding tracer exchange across the Southern Ocean and, ultimately, air-sea carbon fluxes.

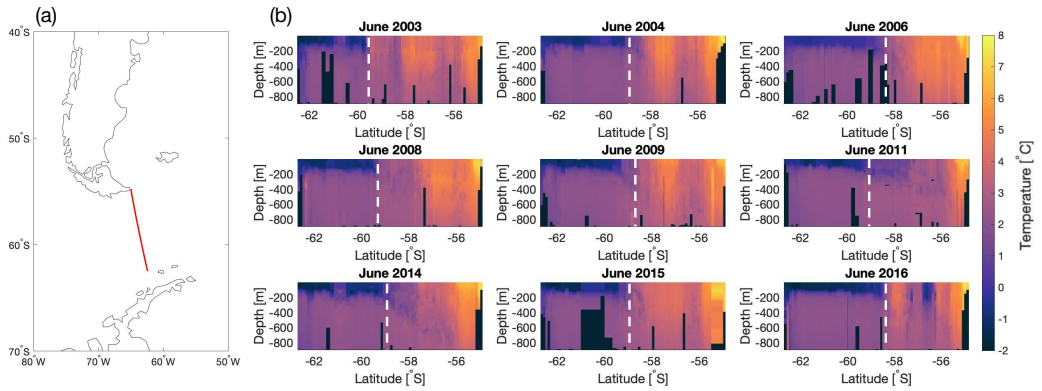

Figure 5.1: Expendable Bathythermograph (XBT) data from Drake Passage.

(a) Location of the XBT survey taken across Drake Passage (b) Nine examples of XBT data from June (austral winter). Black represents regions where no data is available. White dotted lines are locations of the Polar Front as defined by Orsi et al., 1995. Each section is comprised of approximately 60-70 XBTs at roughly equal distances.

5.2 Data and Methods

Biogeochemical-Argo floats

Biogeochemical-Argo (BGC-Argo) floats measure temperature, salinity, pressure, dissolved oxygen, nitrate, pH, fluorescence, and optical backscatter over the top 2,000 m of the water column every 10 days (Riser et al., 2018). The quality-controlled data from the Monterey Bay Aquarium Research Institute provides a snapshot of the float data with estimated total alkalinity and derived carbon parameters for DIC and pCO_2 (http://www3.mbari.org/soccom/SOCCOM_Data_Archive/). Data used here used carbon parameters derived using the Locally Interpolated Alkalinity Regression (LIAR) algorithm from the 21 December 2022 snapshot. Errors of up to 15 μmol kg^{-1} total alkalinity, or 3 μatm pCO_2, are found from alkalinity regressions. LIAR particularly struggles to replicate *in situ* data in the Southern Ocean. These errors are primarily due to a lack of local training data for the interpolation algorithm (personal communication, Ken Johnson and Yui Takeshita).

Air-sea carbon fluxes from observations

Air-sea carbon fluxes will be estimated from the profiling float data using the bulk formula (Gray et al., 2018):

$$F_{CO_2} = kK_0(pCO_2^{ocean} - pCO_2^{atm})$$

where k is the gas transfer velocity, which is calculated from ERA5 winds collocated with the location and time of each float profile (Hersbach et al., 2020). K_0 is the solubility of CO_2 in seawater and is dependent on temperature and salinity. The surface ocean pCO_2^{ocean} is derived from float pH and empirically estimated alkalinity. Measurements of the mole fraction of CO_2 in dry air taken at Cape Grim Observatory are used to estimate atmospheric pCO_2^{atm} (http://www.csiro.au/greenhouse-gases).

Biogeochemical Southern Ocean State Estimate (B-SOSE)

The model used is the data-assimilating B-SOSE, which is produced using the machinery developed by the consortium for Estimating the Circulation and Climate of the Ocean (ECCO; http://www.ecco-group.org). B-SOSE is described in detail in Verdy and Mazloff, 2017 and has an optimization procedure that solves for adjustments to the prescribed atmospheric state and initial oceanic conditions to bring the solution into better consistency with input observations. As a result, B-SOSE is a closed-budget model that provides an estimate of Southern Ocean air-sea fluxes of heat and carbon and the cycling of nutrients from a biogeochemical and carbon model. The available output provides 5-day gridbox tracer averages from 2013 to 2018.

The B-SOSE carbon system is adapted from the MITgcm simple biogeochemical model. DIC and alkalinity are prognostic variables, and pH and pCO2 are diagnosed based on carbonate chemistry numerical solution detailed in Follows et al., 2006. Oceanic pCO_2 is a function of DIC, alkalinity, temperature, salinity and silica, with silica prescribed from the 2013 World Ocean Atlas climatology (Boyer et al., 2013). Air-sea fluxes of pCO_2 are calculated following Wanninkhof, 1992, with atmospheric pCO_2 prescribed using values from Peters et al., 2007.

5.3 Preliminary Results, Discussion, and Next Steps

Data from four BGC-Argo floats that sampled across the Drake Passage provide a preliminary analysis for the observational evidence of stratification impacts on oceanic pCO_2 (Figure 5.2). The preliminary float data provides a spread of profiles across the Drake Passage, with the majority of profiles found south of the climatological PF.

There is an observed inverse relationship between mixed layer pCO_2 and stratification at the base of the mixed layer as measured by BGC-Argo floats (Figure 5.3). The highest values of pCO_2 in the mixed layer are found where stratification at the base of the mixed layer is low. The inverse correlation points to a potential physical

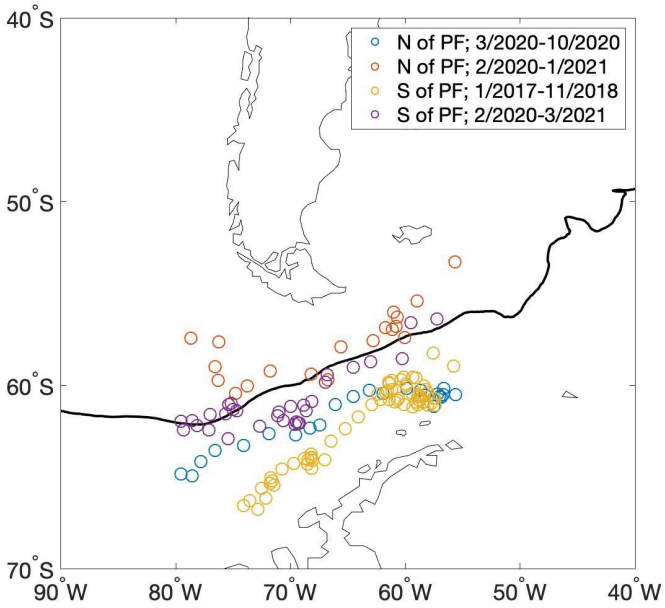

Figure 5.2: Locations of BGC-Argo floats in Drake Passage.

Locations of BGC-Argo profiles (10 day profiling) in Drake Passage. Black line indicates the climatological average location of the Polar Front.

relationship, with high stratification acting as a barrier to high-DIC CDW entering the mixed layer.

Even within a localized region like Drake Passage, there is a spread pCO_2 values of upwards of 200 μatm within the mixed layer. Large positive and negative gradients in pCO_2 between the atmosphere and mixed layer are observed, illustrating Drake Passage's role as a region of both carbon outgassing and uptake, as described by numerical models (Fay et al., 2018; Jiang et al., 2014). Localized vertical velocities associated with submesoscale ageostrophic cross-frontal circulations transport high-DIC and high-nutrient waters into the surface mixed layer (Brannigan, 2016; Mahadevan et al., 2020; Qu et al., 2022; Simoes-Sousa et al., 2022), and these submesoscale processes have been documented at the PF in Drake Passage (Dove et al., 2023), suggesting a potential mechanism that leads to these pCO_2 gradients and the resulting geographic and temporal disparities. However, the distribution of these enhanced fluxes of DIC into the mixed layer and potential for an impact on air-sea carbon fluxes remains underconstrained in the Southern Ocean.

Use of B-SOSE will expand the spatiotemporal analysis of the relationship of stratification and mixed layer pCO_2. Investigation towards B-SOSE may point

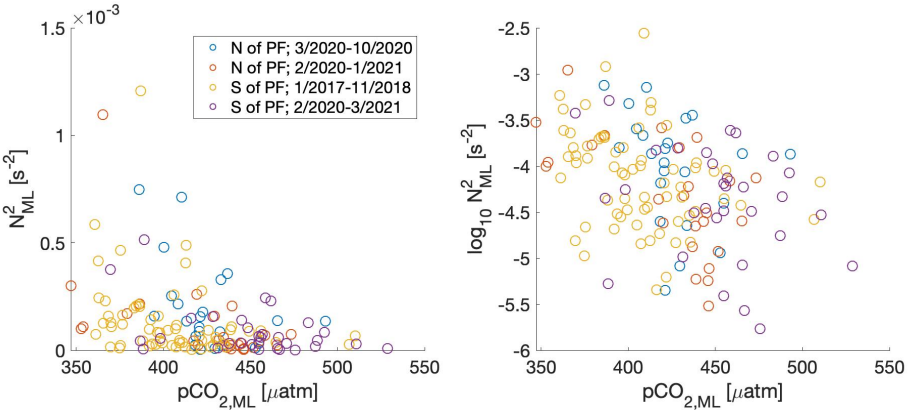

Figure 5.3: BGC-Argo float mixed layer pCO_2^{ocn} against mixed layer stratification. (a) pCO_2 in the mixed layer as calculated from MBARI processing against stratification at the base of the mixed layer, as defined by a density threshold of 0.03 $\frac{kg}{m^3}$. (b) Same as in (a), but with a logarithmic y-axis.

towards potential physical mechanisms that are unresolved in the model but that result in the observed patterns of surface pCO_2, such as vertical processes shaped by submesoscale and mesoscale motions.

While analysis so far has focused on upwelling of high-DIC water into the mixed layer as a predominantly vertical process, there is also a lateral component to be considered. Waters with high-DIC content may be advected from upstream of Drake Passage within the mixed layer. Ongoing analysis will consider lateral advection as a component of the pCO_2 budget in Drake Passage. In addition, while processes on the mesoscale-submesoscale spectrum are expected to contribute to ventilation, previous work has indicated that these processes work at localized scales not well sampled by BGC-Argo 10-day sampling (Dove et al., 2021; Freilich and Mahadevan, 2021).

Additionally, seasonality, surface fluxes, and solubility all have impacts on surface pCO_2 that are yet to be accounted for in this work. The seasonal cycle of mixed layer depth and stratification at the base of the mixed layer has not yet been separated out in the float data. Dove et al., 2023 and Meredith et al., 2011 show that even in wintertime, stratification south of the PF in Drake Passage is strong, preventing exchange between the mixed layer and interior ocean. However, the seasonality in stratification in Drake Passage north of the PF is not as well constrained with high-resolution observations and part of the relationship shown in Figure 5.3 may be a result of a seasonal cycle, with lower stratification expected in wintertime

months. Separating out the pCO_2 pattern into components driven by changes in sea surface temperature (the thermal component) and those driven by changes in DIC and/or alkalinity (the non-thermal component) will provide insight into the relative contributions to pCO_2 and the impact of seasonal and solubility (Gruber et al., 2009; Landschützer et al., 2015; Takahashi et al., 2012). Methods pioneered in Prend et al., 2022 will be employed to segregate the thermal and non-thermal components of pCO_2 in B-SOSE and the BGC-Argo data.

Appendix A

SUPPLEMENTAL INFORMATION FOR CHAPTER II

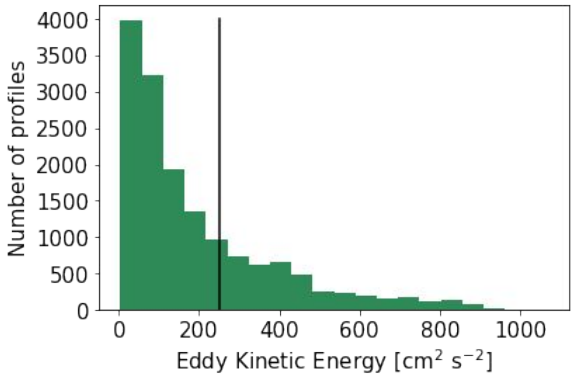

Figure A.1: Histogram of the number of profiles by eddy kinetic energy in the defined Antarctic Circumpolar Current.

Black line represents the boundary of "high" and "low" EKE (cm^2 s^{-1}) used in this work.

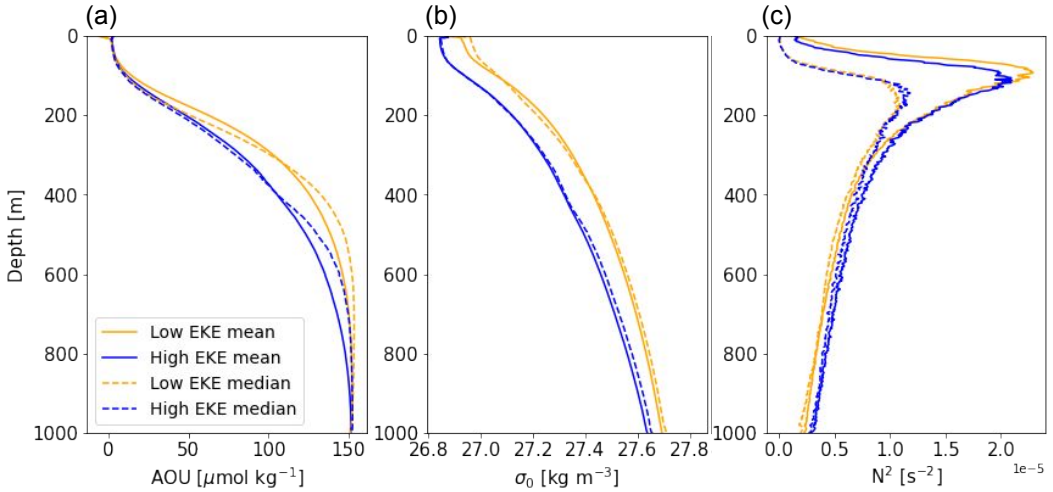

Figure A.2: Averaged float profiles of potential AOU, potential density, and stratification.

(a) AOU [μmol kg^{-1}], (b) Potential density, σ_0, [kg m^{-3}], and (c) Vertical stratification, N^2, [s^{-2}], with depth from all float profiles used in this study. For all panels, blue is high-EKE and orange is low-EKE. Solid lines are means while dashed lines are medians.

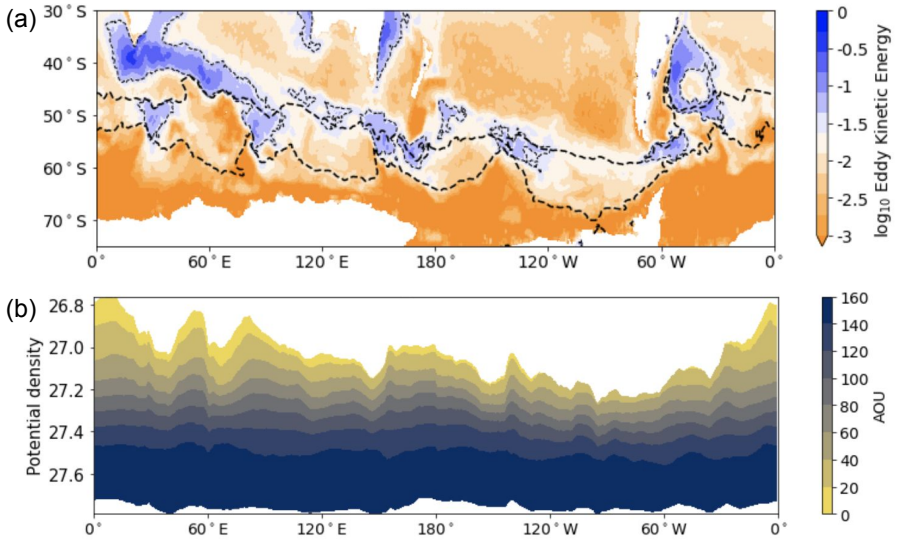

Figure A.3: AOU on density surfaces referenced to EKE.

(a) Base-10 logarithm of eddy kinetic energy [$\log_{10}$ m^2 s^{-2}]. Black dotted lines illustrate the definitions used for ACC boundaries in this study. (b) Median AOU [μmol kg^{-1} on longitude plotted on potential density [kg m^{-3}].

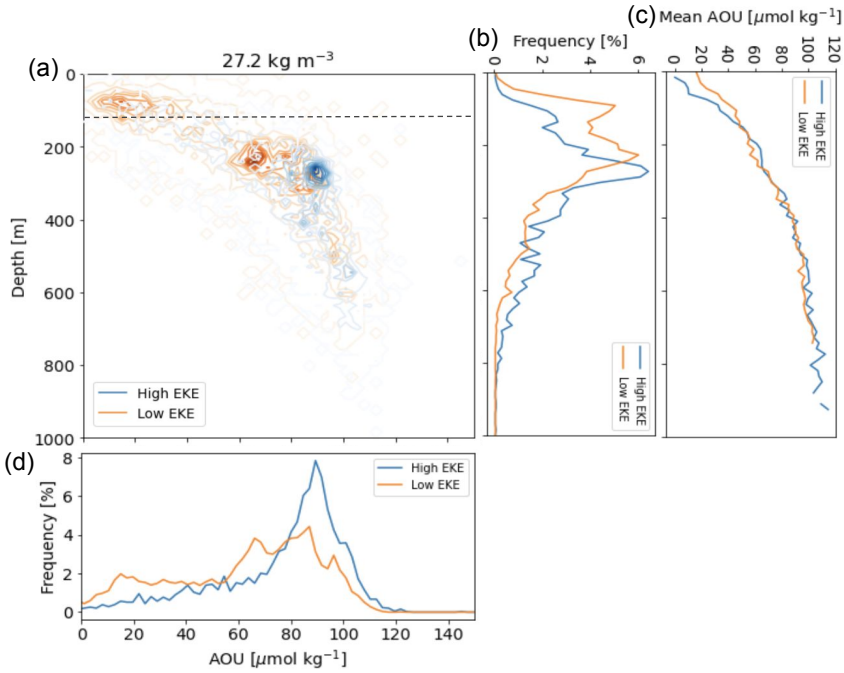

Figure A.4: Joint probability density function on the 27.2 kg m^{-3} density surface.

(a) Joint probability density function of all points on the 27.2 kg m^{-3} density surface in depth and AOU for low-EKE (orange) and high-EKE (blue) regions. Dotted black line represents the average mixed layer depth for both the high- and low-EKE regions and ΔAOU = 2 μmol kg^{-1}, Δz = 10 m. (b) Frequency histogram of depths of the 27.2 kg m^{-3} isopycnal in the ACC. (c) Mean AOU [μmol kg^{-1}] in depth of the 27.2 kg m^{-3} isopycnal in the ACC. (d) Frequency histogram of AOUs of the 27.2 kg m^{-3} isopycnal in the ACC. In (b)-(d), high-EKE regions are denoted in blue, low-EKE regions in orange.

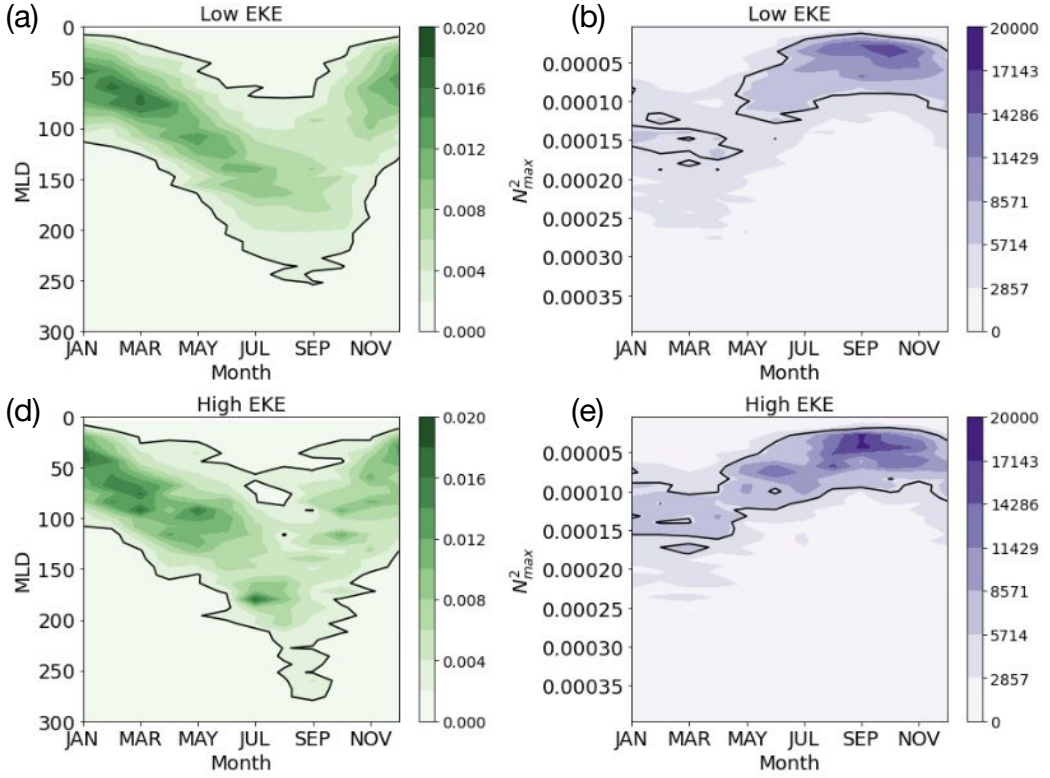

Figure A.5: Joint probability density functions of dynamic features between high- and low-EKE regions.

Month and (a) mixed layer depth [m] and (b) maximum stratification [s^{-2}]. (c) and (d) Same as (a) and (b) but for the high-EKE regions.

Appendix B

SUPPLEMENTAL INFORMATION FOR CHAPTER III

B.1 Processing of Seaglider data

Seaglider measurements of salinity, temperature, pressure, and dissolved oxygen were collected down to 1000 m depth. Salinity, temperature, and pressure were collected at a vertical resolution of approximately 1 m, while dissolved oxygen and optical backscatter data were collected with a vertical resolution of 2–3 m. 500 dives were performed, each with an upcast and a downcast. The raw glider data were processed using the GliderTools toolbox (Gregor et al., 2019). The data were then mapped onto a regular grid with 5 m vertical spacing and 2.5 km horizontal spacing, which corresponds to a temporal scale of approximately 2.4 hours following the GliderTools routine. With this gridding, each 5 meter depth bin holds approximately 10-15 measurements made by the glider. When transformed into neutral density bins, there are approximately 20 glider measurements in near-surface density bins and up to 100 glider measurements in deep density bins. The interpolation uses a Gaussian weighting function with vertical and horizontal scales of 10 m and 4 km, respectively.

Optical backscatter data on the gliders was measured 532 nm. Backscatter data was only collected to 300 m depth, and only in the first third of the deployment. Raw sensor counts were calibrated using the manufacturer-supplied scale factor and dark counts. The resulting volume scattering function includes scattering signal from pure seawater and particulate scattering (Vaillancourt et al., 2004; X. Zhang et al., 2009). The scattering by seawater was calculated using a function described in X. Zhang et al., 2009 and subtracted from the volume scattering function. The resulting particulate volume scattering function was converted into particulate optical backscattering coefficient, bbp (Bol et al., 2018; Briggs et al., 2011). Finally, following Briggs et al., 2011, the backscatter data were filtered using a seven-point minimum filter followed by a seven-point maximum filter in order to remove spikes, which often occur in profiles of bbp due to aggregate material.

B.2 Supplemental Figures

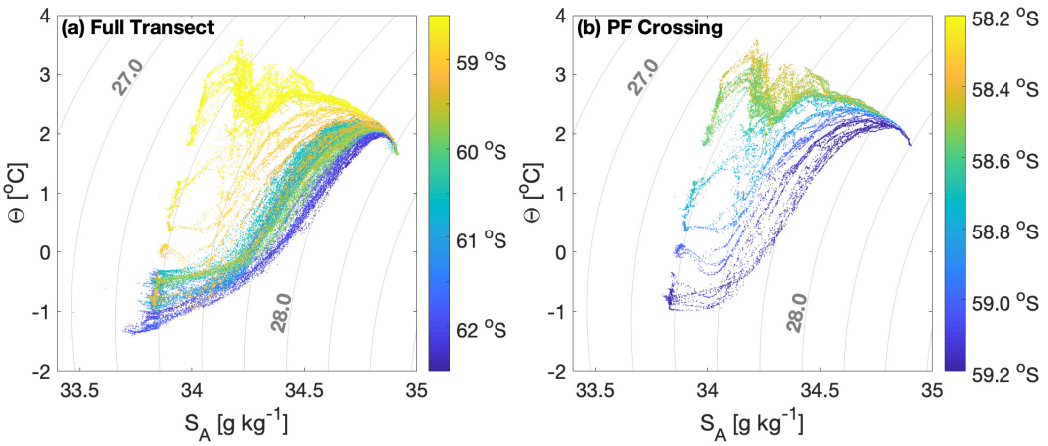

Figure B.1: Temperature-Salinity diagrams for the June northward transect by the second glider.

Points are colored by the latitude at which they were collected. (a) shows data for the entire transect; (b) shows data only in the region immediately surrounding the PF (approximately 1 degree of latitude). The core of the PF was located at approximately 58.5°S.

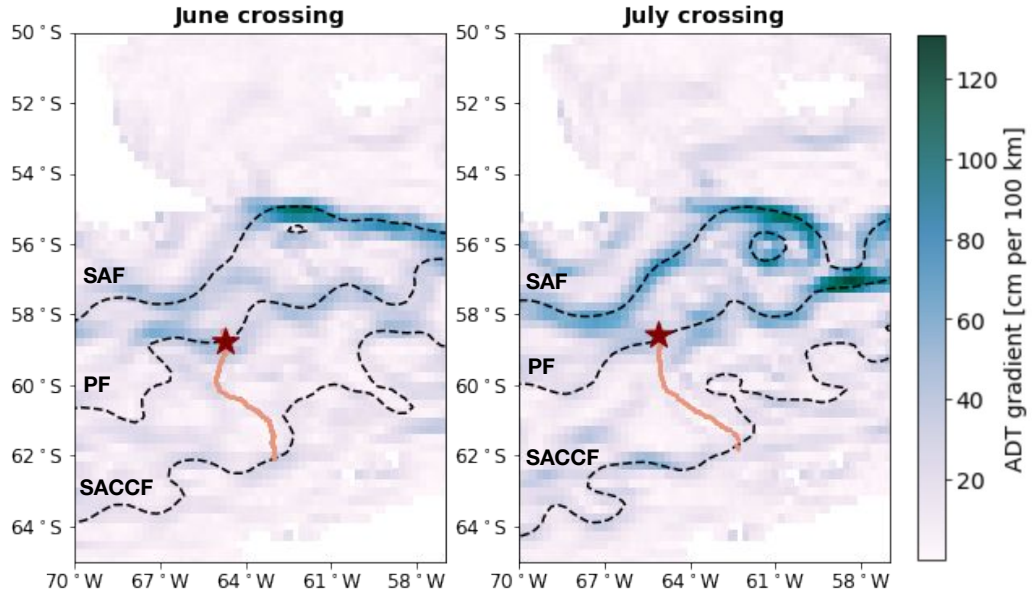

Figure B.2: Glider track with various definitions of the Polar Front.

Data from (a) June and (b) July. Gradient of Absolute Dynamic Topography [ADT] on the date of the PF crossing is shown in color with ADT definitions of the major fronts of the ACC by Kim and Orsi, 2014 in black dashed contours. Glider transects are shown in light red with the location of the PF crossing based on hydrographic definitions by Orsi et al., 1995 at the red star. SACCF = South ACC Front. PF = Polar Front. SAF = Subantarctic Front.

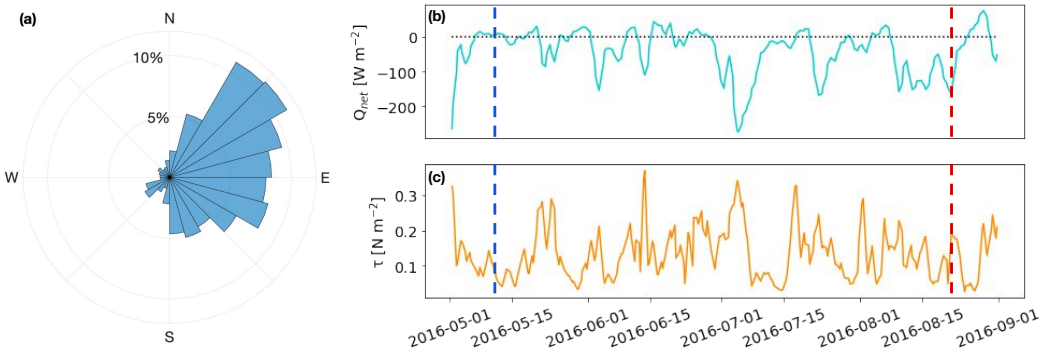

Figure B.3: Surface forcing over Drake Passage from ERA5 reanalysis.

Drake Passage is taken as the box bounded by 55 °S, 65 °S and 60 °W, 70 °W. (a) Histogram of wind directions. The winds are primarily westerly and south-westerly, as is typical of Drake Passage. (b) Surface heat flux, with the diurnal cycle removed. The dotted black line denotes zero surface heat flux. (c) 10-meter wind stress. In (b) and (c), the dashed blue and red lines indicate the start and end, respectively, of the glider deployment.

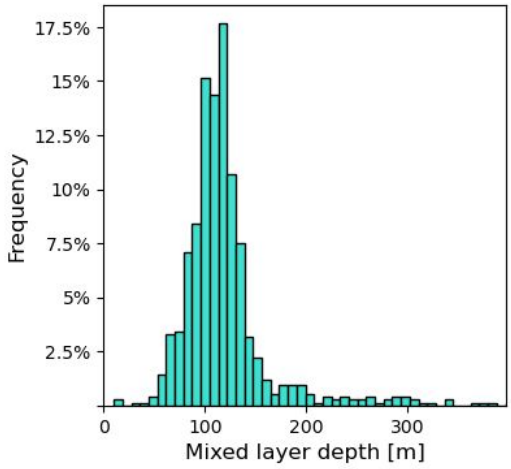

Figure B.4: Histogram of mixed layer depths from glider data.

Mixed layer depth is defined using the criterion of $\Delta\sigma_0 = 0.125$ kg m^{-3} from the surface (Monterey and Levitus, 1997).

Appendix C

STATE OF GENDER EQUITY AND OPTION CULTURE IN ESE AND GPS

C.1 Letter to ESE Faculty, January 2021

To the Caltech ESE faculty,

We are writing this letter to bring to your attention several interconnected problems that we find ourselves facing as graduate students in the ESE option at Caltech. We invite you to reach out to us to discuss the contents of this letter in further detail.

1. The Caltech ESE option has failed to **recruit and retain** female faculty, leaving us far behind our peer institutions in terms of gender representation. The authors of this letter are aware of at least two female faculty who have left the option since 2006. As a result of this failure in recruitment and retention, students and postdoctoral scholars in ESE are left with extremely few, if any, female role models in their field at Caltech. We often end up searching for female mentors outside of ESE or even outside of Caltech, a burden that our male colleagues do not need to carry. In addition, a lack of easily accessible role models leads to heavily male-dominated qualifying exam and thesis committees and does not reflect the true diversity of the field of environmental science as a whole. All members of the option are harmed by this male-dominated culture as the lack of diversity does not teach students how to successfully collaborate with diverse colleagues, including their female peers.

2. Over the last several years, female graduate students in ESE, alongside other minoritized graduate students, have taken on the majority of the **emotional labor** necessary to sustain the option. Community outreach, support of first- and second-year students, and group logistical planning are examples of activities that are unnecessary to successfully earn a PhD, yet necessary for the functioning of the option, and that have fallen primarily to female graduate students. The undervaluing and lack of recognition of these activities leads to higher rates of burnout and a reduced amount of time and energy for research and career advancement activities.

With the announcement of the open tenure-track faculty position in GPS on December 11, 2020, we believe rapid attention is needed to address the concerns we have about gender representation in the ESE option. The authors feel the current status quo is unsustainable and that continuing to recruit female-identifying graduate students to Caltech ESE is not in the best interest of the potential students. Potential students have also recognized the problematic situation with regard to gender representation in Caltech ESE, and we would not be surprised if several excellent candidates have chosen not to apply or not to matriculate due to a lack of female representation at the faculty level. We have identified several requests below that we believe would be excellent first steps for the option to take in order to recognize and begin responding to the multitude of challenges ESE faces with regard to gender equity.

We furthermore offer our suggestions on how to best ensure faculty hiring is transparent and includes important student input. We recognize that rapid changes in faculty composition are challenging at best. Therefore, we include several suggestions on how the option can help female-identifying students in the short term, while longer term changes are being enacted. Finally, we suggest ways the ESE option on the whole can enhance its culture around inclusivity for women.

Disclaimer: We recognize that we are speaking from our own identities, which do not all span many other axes of diversity. We strongly suggest the readers of this letter consider how our suggestions can be applied to advance the representation of other minoritized identities in science. Such identities include race, ethnicity, sexual orientation, disability, immigration status, first-generation student status, and others. We urge the readers to speak to members of those identities to identify solutions to the unique situations of these groups.

We use an inclusive definition of "women" that includes trans women, gender queer, and non binary people.

Requests:

Revamp the faculty hiring process to include student input and increased transparency The faculty hiring process at Caltech is infamously opaque to students. Given that in several years, those of us continuing in academia hope to go through faculty hiring processes for ourselves, it seems in the best interest of the option and the division to involve its students in the hiring process in order to offer us the best knowledge and insight into the process. We therefore suggest several updates to

the faculty hiring process to align with hiring practices at peer institutions such as MIT EAPS and Stanford ESS. Given our limited understanding of the process as it currently stands, we recognize that several of our suggestions may already be in place. We believe that many of these adaptations will assist ESE in considering, interviewing, and hiring more women and minoritized individuals.

Graduate school is a stage at which students form their ideas of how they operate as scientists. Students look to faculty as examples of how one can be a scientist and as role models, both in terms of research and non-academic life. Having a more diverse faculty would give us broader set role models to emulate, which is crucial for forming well-rounded scientists and people.

1. Advertise the position broadly and advertise the shortlist internally. Advertising to societies for underrepresented minorities and women external to Caltech is necessary to break out of the traditional Ivy+ pipelines (Clauset et al., 2015). In addition, it is vital for members of the ESE community to know which seminars are "job talks" so that students and postdocs can provide meaningful and structured feedback on the candidates.

2. Aim for gender parity on the shortlist. Women are not underrepresented at the graduate level in the environmental sciences. Ensuring that the shortlist of potential hires includes a gender balance is a first step to increasing representation.

3. Incorporate students, particularly underrepresented students, onto search committees. Students will soon be going through the job search process themselves and would benefit from serving on hiring committees in an advisory role, if not as voting members. The role of the students should be to assess the advising and mentoring abilities of the candidates as well as to potentially organize a guest lecture or mock class during which the candidate could present their teaching style.

Temporary solutions Because we understand that faculty hiring is a long-term plan and gender parity in the option at the faculty level is not an attainable goal even in the next decade, we have a number of requests and recommendations for shorter-term plans. These range from increasing visibility of non-faculty women in the option to simply acknowledging the lack of female faculty and the extra burden this places on female students.

Include a statement on the website if certain faculty are unable to take students so prospective students can make an informed decision. Currently, the ESE option website does not make clear which faculty are presently active at Caltech. Given the dearth of female faculty, a reduction of one active member is a proportionally large reduction in the total female representation in the option, and this information is currently kept from prospective applicants. Applicants to ESE deserve to have accurate information about the makeup of the option before they decide to apply. Currently the job of informing prospective students about the reality of the makeup of the option falls to current graduate students, often during prospective student visit weekend. While the option works to increase its representation of female faculty, honesty and transparency about the current situation is necessary in order to make sure potential students are able to make an informed decision.

Ensure that women are at the forefront of the ESE first-year graduate learning experience. Currently, the required classes for ESE first years are taught solely by male faculty. In fact, it is possible and common to complete the entire ESE curriculum without engaging with a female head instructor. To assist in helping students engage with potential female mentors (Drury et al., 2011), we suggest the option take advantage of our close connection to JPL as well as the wealth of expertise present in the ESE postdoctoral scholar population by inviting guest speakers, and particularly female-identifying speakers, to teach classes. This allows students to engage with members of the extended academic community, gives interested postdocs and scientists the opportunity to practice teaching, and also partially addresses the gender imbalance of instructors.

Reconsider the qualifying exam. Of the 16 qualifying exams that were taken by ESE students in the last two years, 15 had all-male committees. It is extremely concerning that students who are entering the most important examination of their graduate school career may not see themselves reflected in the composition of the committee. Literature in the STEM Education field as well as the personal experiences of female students in ESE emphasizes that exclusively male groups can make settings unwelcoming and emphasize the disparity in access to role models for female participants. Feeling like you have to represent not only your science but also your gender and potentially other minoritized aspects of your identity is a difficult barrier to overcome, particularly in the example of quals, where there is a very definitive power imbalance between the student and the faculty committee.

Revamping the qualifying exam process is complex and requires strategic consid-

eration. While we have many ideas and suggestions, it is the job of the option and division to develop an exam that is equitable to all takers. We highly recommend consultation with the Caltech Center for Inclusion and Diversity (CCID) and Center for Teaching, Learning, and Outreach (CTLO) in such a process.

Present solutions for how students can increase the diversity of their TAC. The suggested makeup of a GPS Thesis Advisory Committee (TAC) is 4 faculty members, at least 3 of whom must be Caltech faculty. In order to reach this requirement using faculty in the ESE option, which most ESE students do, almost all committees have at least 3 white male faculty. While students can use their fourth spot to bring in a researcher from another institution, this presents a limitation to many students and cannot bring the committee to gender parity. While it is possible to bring in more than one external member (for a total of more than four members), this option is mostly unknown. Therefore, we suggest this be explicitly written down and explained to students in the second year as they are forming their TACs.

Option culture Finally, to make the option more welcoming to minoritized students and faculty alike, and increase retention of these valuable members of our community, we have three proposals for how to improve the culture of the option.

Implement mandatory implicit bias and bystander intervention training for the full option. While faculty are required to have workplace harassment training annually, graduate students are not. In order to make ESE's position on sexual harassment clear, we suggest that the full option or groups within the option have mandatory implicit bias and bystander intervention trainings at regular intervals. The Caltech Title IX and Equity Office offers trainings that can be adapted to an individual lab group's needs, including trainings specific to office, laboratory, or field work. While trainings are just a first step towards recognizing implicit sexism and other forms of discrimination in academia, we believe making such trainings an integral part of the option will open the conversation and allow everyone to be aware of their reporting options as well as what is and is not appropriate in a workplace environment.

Recognize and validate emotional labor. There are many activities that are necessary for a department to function at its highest level but that are not necessary for earning a degree, such as community outreach, support of younger students, and group logistical planning (Group, 2017). The majority of this work in the ESE option, particularly in informal mentoring of first- and second-year students, has fallen to female graduate students, and we urge the faculty to recognize this disparity. This

has become particularly true in the time of the pandemic, when barriers to informal conversations are higher than ever.

We suggest that a more organized strategy for informal mentorship is required. The initiation of the "first year buddies" program at the division level by the Academic Committee is a good start. We suggest this program be further supported and potentially implemented in research groups as well. Recognition of emotional labor by the faculty puts value on the related actions. Actively making mentorship an encouraged and celebrated act of service at the research group level and option level encourages those who are not socially primed to step into such positions to pursue these activities.

Acknowledge the ongoing problem of gender representation with words and actions. We request that the option faculty formally acknowledge the insufficient female representation at the highest echelon of the option as a problem and publicly put forward and follow an actionable plan for the option to address this problem. Just as we must plan our experiments before we run them, we must have a plan for how to determine if our actions are successful and how to adapt if not. Running on good faith alone, while utopic, is not sustainable. In addition, hiring a single female faculty, while a first step, will not solve the majority of the challenges we have outlined above. We hope the suggestions offered in this letter give a good starting place for such an action plan.

In the past, the authors of this letter have felt that our requests for acknowledgement and action have been underappreciated by several members of the ESE faculty. We plan to continue engaging in this discussion and we urge the readers of this letter to reach out to their female colleagues at Caltech and other institutions to consider further steps that can be taken to address our concerns. This letter comes as an invitation to start an open dialogue with us and we look forward to continuing this conversation with you.

Respectfully,
Lily Dove, ESE G3
Clare Singer, ESE G3
Sara Murphy, ESE G3

Supported by:
Polina Khapikova, ESE G2 Krystal Vasquez, CCE G6 Jordan Benjamin, ESE G2

Katrina Hui, ESE G5 James Mullahoo, ESE G1 Costa Christopoulos, ESE G2 Ruth Moorman, ESE G1 Reina Buenconsejo, CCE G3 Ignacio Lopez Gomez, ESE G3 Henry Peterson, ESE G2 Sophia Charan, CCE G5 Sam Zhang, ESE G3 Yue Bai, ESE G1 Dave Bonan, ESE G2 Haakon Ludvig Langeland Ervik, ESE G1 Ryan Ward, ESE G2 Scott Conn, ESE G1 Preston Cosslett Kemeny, Geochemistry G5 Daniela Osorio Rodriguez, Geobiology G4 Ren Marquez, Geochemistry G3 Holly Barnhart, Geochemistry G2 Harrison Parker, ESE G5 Shirui Peng, ESE G2 Emily de Jong, MCE G2 Hannah Allen, CCE G7 Newton Nguyen, ESE G4 Ariana Tribby, CCE G4 Ana Lobo, PS G6 Jacqueline Dowling, CCE G4

C.2 Letter to ESE Faculty, February 2022

To the ESE faculty:

Here, we are continuing the conversation regarding issues in the ESE option. We look forward to discussing this topic with you further at the ESE Town Hall on March 11, 2022.

We recognize this year has been uncertain and harsh for everyone in our option; the pandemic has made doing science at our normal pace difficult and has also made personal challenges even more burdensome. However, we urge you to consider how the continuing uneven spread of invisible work* and unmet promises regarding change in option culture have been additional challenges for some members of our community (Berhe et al., 2022; King and Frederickson, 2021). In order for students to be successful in ESE, it is necessary for the option to reflect on issues of mentorship and the uneven spread of invisible work, which are multi-faceted concerns that we outline below.

*We are defining invisible work as activities that are necessary for a department to function at its highest level but that are not necessary for earning a degree or advancing your career, such as mentoring and support of younger students, discussing issues of diversity, community outreach, and group logistical planning.

Faculty hiring

We are cognizant that building a representative faculty will take time and we are grateful for the steps the option has taken to center female-identifying candidates and candidates of color in the current ESE faculty search. In addition, we are grateful for the enhancement of transparency in the hiring process, including widely advertising the position, making the shortlist publicly available, holding student coffee hours and meals with the candidates, and providing a mechanism for student feedback.

Recruitment is only one part of the equation of building a representative department; we are mindful that it will take active steps to retain these candidates, provided one is hired (Ranganathan et al., 2021). Given ESE's current faculty makeup, we are concerned that this new faculty member could experience tokenism and be asked to shoulder a large load of invisible work, particularly mentorship. As we brought up in our letter last year, the distribution of invisible work in our option is not spread evenly; any issues currently faced by students in the option may be exacerbated for a new faculty member because they will lack the peer network that we rely on. The option must focus on building an inclusive space where everyone feels welcome, including but not limited to the excellent candidates on the shortlist. This work is vital for faculty and student retention.

Distribution of invisible mentorship work

To state it explicitly, there are many unassigned and unpaid tasks that are important for our option to function in the most efficient and inclusive manner possible. This invisible work is done by minoritized groups in science in order to increase inclusivity and broaden access to success in academia (Guarino and Borden, 2017; Posselt et al., 2017; Reid, 2021); in short, it is a form of mentorship. This work can take many forms, including, but not limited to, leading discussions about Diversity, Equity, and Inclusion (DEI), doing internal and external outreach, informally and formally mentoring younger students, and running updated group websites (Peña et al., 2022). Specifically, we do this work because we see it as vital for the retention and success of students in ESE, ourselves included. Therefore, we cannot always be the ones doing it.

One fear we have, stated earlier, is that this invisible work will disproportionately burden whichever of the candidates ESE hires in the ongoing search. We feel there is a need for the option to take ownership of these responsibilities and create more official structures so that the work can be shared more evenly and people doing this work can receive adequate credit and/or compensation for it. We recognize that as a small option, there will always be ways in which people need to step up to help the option and lab groups function. Societally, women are more likely to serve in caregiving roles and this pattern extends to academia, with women more likely to "care for the academic family" (Jimenez et al., 2019). This is happening in our option. It is the job of the option to proactively recognize and combat this discrepancy to help its members be successful scientists.

As stated in your previous letter (February 9, 2021), one way to combat these

gaps in support is to develop "more formal approach[es] that will transfer more of the burden to the faculty and encourage broader participation of the senior ESE students." We understand the GPS Academic Committee has been working to develop more formal guidelines; we look forward to learning more, but have not yet seen this output. There are wide discrepancies between ESE faculty about what constitutes mentorship and in the cases where students are not receiving the mentorship they need, the burden continues to fall on a small group of more senior students and postdocs, including ourselves. It is important to note that every student requires different kinds of mentorship to excel (Harding-DeKam et al., 2012). To best support students, mentorship needs to be an active process in which both parties (mentor and mentee) are engaged. The current status of mentoring in our option goes beyond individual faculty having individual mentorship styles; there are ESE students who are actively falling through the cracks.

One step to begin addressing this challenge in our option is for each ESE lab group to develop a Code of Conduct that makes explicit the values, expectations, and procedures of the group. The Wennberg lab has an excellent Code of Conduct that can be used as an example for other ESE lab groups. In addition, Individual Development Plans (IDPs) may be a structured way to guide a conversation between students and faculty members about expectations, goals, and accomplishments. Creating and regularly updating Codes of Conduct is additionally a way to begin addressing the invisible work issue presented above and clarifying expectations for the group.

Every faculty member in our option has aspects of their mentorship that can be improved. We urge each of you to self-reflect and have candid conversations with your group members about what aspects of your mentorship do and do not work to prepare, support, and boost the confidence of your advisees. It is also useful to reflect on these topics with others, including peers or support systems available at Caltech.

Qualifying Exams as an example of failures in mentoring

One place in which the discrepancy in mentorship is abundantly clear is the qualifying exam. We focus on women in this discussion because there is not sufficient statistical power from these data given the small numbers of students in our division with other identities marginalized in science. Data from 71 current GPS graduate students and recent alumni show that women have less positive experiences with their first year and the qualifying exam process. Specifically, looking at questions

related to mentorship (how prepared, supported, and confident students felt), there is an imbalance between the male and female survey respondents regardless of exam outcome (Figure C.1) In addition, this insufficient support for female students is correlated with higher failure rates. Data illustrates that women in GPS are statistically significantly more likely to fail their qualifying exam than their male peers (Figure C.2). We see this as one example of a failure of mentorship in the division. While we do not believe anyone is actively seeking to fail women in the qualifying exam, we believe the division, including ESE, often fails to provide successful mentorship to minoritized groups in science (including women) and these gaps are shown in this data. These are the gaps we are attempting to fill with invisible work.

We hope ESE can be a leader in approaching this reality head-on and redesigning the qualifying exam and its mentorship practices to result in an equitable learning experience for its students. We highly recommend consultation with the Caltech Center for Inclusion and Diversity (CCID), Equity and Title IX Office, and Center for Teaching, Learning, and Outreach (CTLO) in such a process.

While our previous conversations on these issues have led to several proposed solutions, we feel that there has often been a lack of follow-through on these conversations. We are grateful for the steps that the faculty have taken thus far: bystander training for lab groups, increased community building events, student representation at faculty meetings, and transparency in the hiring process. However, when we look back on your response from February 2021, there are many commitments that have been forgotten. We hope that, in our ongoing conversations, we can discuss mechanisms for accountability that ensure that these conversations occur more than once a year and commitments to action do not fall through the cracks.

Sincerely,
Lily Dove, ESE G4
Sara Murphy, ESE G4
Clare Singer, ESE G4

Supported by:
Polina Khapikova, ESE G3 Harrison Parker, ESE G6 Liyin He, ESE G6 Henry Peterson, ESE G3 Scott Conn, ESE G2 James Mullahoo, ESE G2 Luna Bai, ESE G2 Newton Nguyen, ESE G5 Haroula Baliaka, ESE G1 Dave Bonan, ESE G3 Benjamin Schulze, ESE G4 Reina Buenconsejo, CCE G4 Haakon Ludvig Langeland Ervik, ESE G2 Holly Barnhart, Geochemistry G3 Rui Cheng, ESE G5 Ronak Patel, ESE

G1 Ruth Moorman, ESE G2 Ryan Ward, ESE G3

Disclaimer: We use an inclusive definition of "women" that includes trans women, gender queer people, and non-binary people. We recognize that we are speaking from our own identities and experiences, which are not universal. We encourage the faculty to consider how the issues discussed here may affect students of a variety of marginalized identities in science.

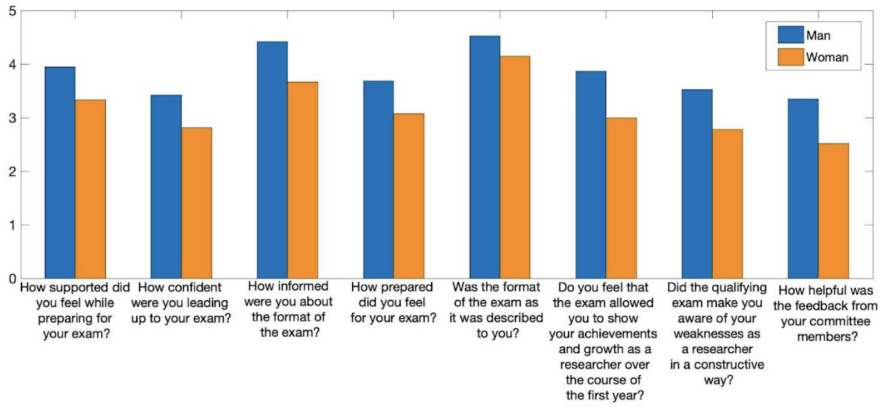

Figure C.1: Results from student survey on qualifying exam experience.

Data from 71 current GPS graduate students and recent alumni. Results are broken down by gender, man (blue) and woman (orange). Questions were asked on a scale of 1 ("strongly disagree") to 5 ("strongly agree"). Non-binary was an available option for gender but there were not enough respondents who chose this option to present anonymized statistics.

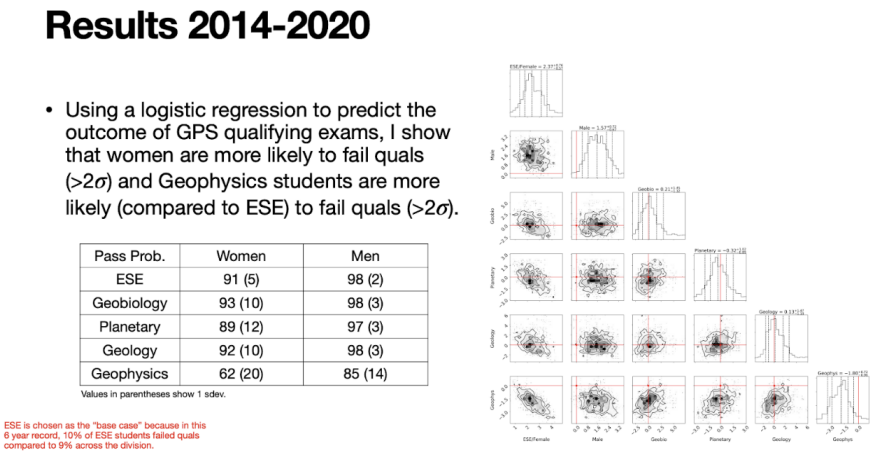

Figure C.2: Statistical analysis of qualifying exam outcomes.

Data from GPS qualifying exam outcomes from 2014-2020. This dataset did not offer non-binary as a gender option.

C.3 Letter to Qualifying Exam Core Committee, August 2022

Dear Mike,

CC: Qualifying exam core committee and GPS Division leadership

We are writing to you in your position as chair of the GPS qualifying exam core committee to present three requests from the student body.

We, the authors of this letter, presented concerning findings to the GPS DEI committee, the GPS qualifying exam core committee, and the GPS academic committee during summer 2021. A full timeline of our communication is below. As we showed, there are serious issues with the qualifying exam in its current format. These issues include, but are not limited to:

1. Wide disparities across peoples' first year and exam experiences, with the widest *identifiable* disparities between men and women.
2. A culture of disrespect among some faculty towards students taking their exam (e.g. falling asleep, arriving late/leaving early, on cell phone during exam, etc).
3. Exam takers receiving little actionable feedback from their committee members.

These findings are based on an anonymized survey taken in summer 2021 by 71 current GPS graduate students and recent alumni. **Perhaps most alarming, a quantitative consideration of the pass rates across GPS split by a gender binary shows that female students in GPS are 2.6x (2σ confidence level) more likely to fail their exam than their male counterparts.** As a result of small numbers, we were not able to anonymously break down the data to look quantitatively at other aspects of identity spanning gender diversity, race, ethnicity, first-generation status, disability, etc.

At the GPS Town Hall on Tuesday, May 31, 2022, it was announced to the Division that the core committee is in charge of reconsidering the qualifying exam process. However, details about this process as well as the extent of student input were opaque and have not been made clear since. As a result, we are writing to ask for three things:

1. Officially announce over email the formation, membership, and mission of the qualifying exam core committee with regard to reconsidering and redesigning

the GPS qualifying exam. In this email, present a timeline of the goals of the committee, including when students will be consulted, when changes to the exam will be announced and implemented, and when such changes will be assessed and modified, if necessary.

2. Consult with post-quals graduate students about the current challenges presented by the exam as well as proposed changes. This can take the form of individual interviews, focus groups, surveys, or other format(s) the committee finds useful.

3. Present regular updates from the committee to the Division and create a mechanism for feedback from the Division to the committee. As the DEI committee has done, this can take the format of posting meeting agendas and minutes and having a portal for comments, with the option for anonymity. Another idea is to have quarterly meetings to present progress and listen to feedback.

We look forward to your reply.

Thank you,
Lily Dove, ESE G5
Sara Murphy, ESE G5
Clare Singer, ESE G5

Cosigners:
Henry Peterson, ESE G4 Aida Behmard, PS G6 John Naviaux, ESE Alumni Harrison Parker, ESE G7 Voon Hui Lai, Geophysics Alumni Ojashvi Rautela, Geophysics G4 Haakon Ludvig Langeland Ervik, ESE G3 Mike Greklek-McKeon, PS G4 Dan Johnson, Geochemistry Alumni Oliver Stephenson, Geophysics G7 Emma Sofia Sosa, Geology G6 Dustin Morris, Geology G6 Celeste Labedz, Geophysics Alumni Carl Swindle, Geology G5 Dana Anderson, PS Alumni Alexandra Atlee Phillips, Geochemistry Alumna Ana Lobo, Planetary Alum Oliver Wilner, Geology G3 Scott Conn, ESE G3 Tobias Köhne, Geophysics G5 Yue Bai, ESE G3 Renée Zurui Wang, Geochemistry G6 James Mullahoo, ESE G3 Zachary Erickson, ESE Alum Giuliana Viglione, ESE Alum Holly Barnhart, Geochemistry G4 Ben Thyer, Geology G3 Tina Seeger, Geology G3 Jocelyn Reahl, Geology G3 Sihe Chen, PS G3 Hannah Dion-Kirschner, Geobiology G4 Vasilije Dobrosavljevic, Geophysics Alumnus

Ellen Robo, Geophysics Alum Yi Zhang, ESE G5 Shreyas Vissapragada, PS Alum Hannah Way, Geobiology G3 Julie Inglis, Planetary Sciences G3 Ren Marquez, Geochemistry G5 Polina Khapikova, ESE G4 Calvin Rusley, Geobiology G3 Dave Bonan, ESE G4 Nicole Wallack, PS Alum Korbinian Thalhammer, Geochemistry G3

BIBLIOGRAPHY

Abernathey, R. P., Cerovecki, I., Holland, P. R., Newsom, E., Mazloff, M. R., & Talley, L. D. (2016). Water-mass transformation by sea ice in the upper branch of the southern ocean overturning. *Nature Geoscience*, *9*(8), 596–601. https://doi.org/10.1038/ngeo2749

Abernathey, R. P., & Cessi, P. (2014). Topographic enhancement of eddy efficiency in baroclinic equilibration. *Journal of Physical Oceanography*, *44*(8), 2107–2126. https://doi.org/10.1175/JPO-D-14-0014.1

Abernathey, R. P., & Ferreira, D. (2015). Southern ocean isopycnal mixing and ventilation changes driven by winds. *Geophysical Research Letters*, *42*(23), 10, 357–10, 365. https://doi.org/https://doi.org/10.1002/2015GL066238

Abernathey, R. P., Ferreira, D., & Klocker, A. (2013). Diagnostics of isopycnal mixing in a circumpolar channel. *Ocean Modelling*, *72*, 1–16. https://doi.org/10.1016/j.ocemod.2013.07.004

Adams, K. A., Hosegood, P., Taylor, J. R., Sallée, J.-B., Bachman, S., Torres, R., & Stamper, M. (2017). Frontal circulation and submesoscale variability during the formation of a southern ocean mesoscale eddy. *Journal of Physical Oceanography*, *47*(7), 1737–1753. https://doi.org/10.1175/JPO-D-16-0266.1

Archer, M., Schaeffer, A., Keating, S., Roughan, M., Holmes, R., & Siegelman, L. (2020). Observations of submesoscale variability and frontal subduction within the mesoscale eddy field of the tasman sea. *Journal of Physical Oceanography*, *50*(5), 1509–1529. https://doi.org/10.1175/JPO-D-19-0131.1

Bachman, S. D., & Klocker, A. (2020). Interaction of jets and submesoscale dynamics leads to rapid ocean ventilation [Publisher: American Meteorological Society]. *Journal of Physical Oceanography*, *50*(10), 2873–2883. https://doi.org/10.1175/JPO-D-20-0117.1

Bachman, S. D., Taylor, J. R., Adams, K. A., & Hosegood, P. J. (2017). Mesoscale and submesoscale effects on mixed layer depth in the southern ocean. *Journal of Physical Oceanography*, *47*(9), 2173–2188. https://doi.org/10.1175/JPO-D-17-0034.1

Bakker, D. C. E., Pfeil, B., Landa, C. S., Metzl, N., O'Brien, K. M., Olsen, A., Smith, K., Cosca, C., Harasawa, S., Jones, S. D., Nakaoka, S.-i., Nojiri, Y., Schuster, U., Steinhoff, T., Sweeney, C., Takahashi, T., Tilbrook, B., Wada, C., Wanninkhof, R., ... Xu, S. (2016). A multi-decade record of high-quality fCO_2 data in version 3 of the surface ocean CO_2 atlas (SOCAT). *Earth System Science Data*, *8*(2), 383–413. https://doi.org/10.5194/essd-8-383-2016

Balwada, D., LaCasce, J. H., Speer, K. G., & Ferrari, R. (2021). Relative dispersion in the antarctic circumpolar current. *Journal of Physical Oceanography*, *51*(2), 553–574. https://doi.org/10.1175/JPO-D-19-0243.1

Balwada, D., Smith, K. S., & Abernathey, R. P. (2018). Submesoscale vertical velocities enhance tracer subduction in an idealized antarctic circumpolar current. *Geophysical Research Letters*, *45*(18), 9790–9802. https://doi.org/10.1029/2018GL079244

Balwada, D., Speer, K. G., LaCasce, J. H., Owens, W. B., Marshall, J., & Ferrari, R. (2016). Circulation and stirring in the southeast pacific ocean and the scotia sea sectors of the antarctic circumpolar current. *Journal of Physical Oceanography*, *46*(7), 2005–2027. https://doi.org/10.1175/JPO-D-15-0207.1

Balwada, D., Xiao, Q., Smith, K. S., Abernathey, R. P., & Gray, A. R. (2021). Vertical fluxes conditioned on vorticity and strain reveal submesoscale ventilation. *Journal of Physical Oceanography*, *51*(9), 2883–2901. https://doi.org/10.1175/JPO-D-21-0016.1

Barthel, A., Hogg, A. M., Waterman, S., & Keating, S. (2017). Jet–topography interactions affect energy pathways to the deep southern ocean. *Journal of Physical Oceanography*, *47*(7), 1799–1816. https://doi.org/10.1175/JPO-D-16-0220.1

Berhe, A. A., Barnes, R. T., Hastings, M. G., Mattheis, A., Schneider, B., Williams, B. M., & Marín-Spiotta, E. (2022). Scientists from historically excluded groups face a hostile obstacle course. *Nature Geoscience*, *15*(1), 2–4. https://doi.org/10.1038/s41561-021-00868-0

Bianchi, D., Weber, T. S., Kiko, R., & Deutsch, C. (2018). Global niche of marine anaerobic metabolisms expanded by particle microenvironments. *Nature Geoscience*, *11*(4), 263–268. https://doi.org/10.1038/s41561-018-0081-0

Bischoff, T., & Thompson, A. F. (2014). Configuration of a southern ocean storm track. *Journal of Physical Oceanography*, *44*(12), 3072–3078. https://doi.org/10.1175/JPO-D-14-0062.1

Boccaletti, G., Ferrari, R., & Fox-Kemper, B. (2007). Mixed layer instabilities and restratification. *Journal of Physical Oceanography*, *37*(9), 2228–2250. https://doi.org/10.1175/JPO3101.1

Bol, R., Henson, S. A., Rumyantseva, A., & Briggs, N. (2018). High-frequency variability of small-particle carbon export flux in the northeast atlantic. *Global Biogeochemical Cycles*, *32*(12), 1803–1814. https://doi.org/10.1029/2018GB005963

Bourgeois, T., Goris, N., Schwinger, J., & Tjiputra, J. F. (2022). Stratification constrains future heat and carbon uptake in the southern ocean between 30°s and 55°s. *Nature Communications*, *13*(1), 340. https://doi.org/10.1038/s41467-022-27979-5

Boyd, P. W., Claustre, H., Lévy, M., Siegel, D. A., & Weber, T. (2019). Multi-faceted particle pumps drive carbon sequestration in the ocean. *Nature*, *568*(7752), 327. https://doi.org/10.1038/s41586-019-1098-2

Boyer, T. P., Antonov, J. I., Baranova, O. K., Garcia, H. E., Johnson, D. R., Mishonov, A. V., O'Brien, T. D., Seidov, D., Smolyar, I. (, Zweng, M. M., Paver, C. R., Locarnini, R. A., Reagan, J. R., Coleman, C., & Grodsky, A. (2013). World ocean database 2013. https://doi.org/10.7289/V5NZ85MT

Brady, R. X., Maltrud, M. E., Wolfram, P. J., Drake, H. F., & Lovenduski, N. S. (2021). The influence of ocean topography on the upwelling of carbon in the southern ocean. *Geophysical Research Letters*, *48*(19), e2021GL095088. https://doi.org/10.1029/2021GL095088

Brannigan, L. (2016). Intense submesoscale upwelling in anticyclonic eddies. *Geophysical Research Letters*, *43*(7), 3360–3369. https://doi.org/10.1002/2016GL067926

Briggs, N., Dall'Olmo, G., & Claustre, H. (2020). Major role of particle fragmentation in regulating biological sequestration of CO2 by the oceans. *Science*, *367*(6479), 791–793. https://doi.org/10.1126/science.aay1790

Briggs, N., Perry, M. J., Cetinić, I., Lee, C., D'Asaro, E., Gray, A. M., & Rehm, E. (2011). High-resolution observations of aggregate flux during a sub-polar north atlantic spring bloom. *Deep Sea Research Part I: Oceanographic Research Papers*, *58*(10), 1031–1039. https://doi.org/10.1016/j.dsr.2011.07.007

Buckingham, C. E., Lucas, N. S., Belcher, S. E., Rippeth, T. P., Grant, A. L. M., Le Sommer, J., Ajayi, A. O., & Naveira Garabato, A. C. (2019). The contribution of surface and submesoscale processes to turbulence in the open ocean surface boundary layer. *Journal of Advances in Modeling Earth Systems*, *11*(12), 4066–4094. https://doi.org/10.1029/2019MS001801

Buesseler, K. O., & Boyd, P. W. (2009). Shedding light on processes that control particle export and flux attenuation in the twilight zone of the open ocean. *Limnology and Oceanography*, *54*(4), 1210–1232. https://doi.org/10.4319/lo.2009.54.4.1210

Bushinsky, S. M., Gray, A. R., Johnson, K. S., & Sarmiento, J. L. (2017). Oxygen in the southern ocean from argo floats: Determination of processes driving air-sea fluxes. *Journal of Geophysical Research: Oceans*, *122*(11), 8661–8682. https://doi.org/10.1002/2017JC012923

Chapman, C. C., Hogg, A. M., Kiss, A. E., & Rintoul, S. R. (2015). The dynamics of southern ocean storm tracks. *Journal of Physical Oceanography*, *45*(3), 884–903. https://doi.org/10.1175/JPO-D-14-0075.1

Chapman, C. C., Lea, M.-A., Meyer, A., Sallée, J.-B., & Hindell, M. (2020). Defining southern ocean fronts and their influence on biological and physical processes in a changing climate. *Nature Climate Change*, *10*(3), 209–219. https://doi.org/10.1038/s41558-020-0705-4

Chelton, D. B., deSzoeke, R. A., Schlax, M. G., Naggar, K. E., & Siwertz, N. (1998). Geographical variability of the first baroclinic rossby radius of deformation. *Journal of Physical Oceanography*, *28*(3), 433–460. https://doi.org/10.1175/1520-0485(1998)028<0433:GVOTFB>2.0.CO;2

Clauset, A., Arbesman, S., & Larremore, D. B. (2015). Systematic inequality and hierarchy in faculty hiring networks. *Science Advances*, *1*(1), e1400005. https://doi.org/10.1126/sciadv.1400005

Claustre, H., Johnson, K. S., & Takeshita, Y. (2020). Observing the global ocean with biogeochemical-argo. *Annual Review of Marine Science*, *12*(1), 23–48. https://doi.org/10.1146/annurev-marine-010419-010956

Close, S. E., Naveira Garabato, A. C. N., McDonagh, E. L., King, B. A., Biuw, M., & Boehme, L. (2013). Control of mode and intermediate water mass properties in drake passage by the amundsen sea low. *Journal of Climate*, *26*(14), 5102–5123. https://doi.org/10.1175/JCLI-D-12-00346.1

Dall'Olmo, G., Dingle, J., Polimene, L., Brewin, R. J. W., & Claustre, H. (2016). Substantial energy input to the mesopelagic ecosystem from the seasonal mixed-layer pump. *Nature Geoscience*, *9*(11), 820–823. https://doi.org/10.1038/ngeo2818

de Baar, H. J. W., de Jong, J. T. M., Nolting, R. F., Timmermans, K. R., van Leeuwe, M. A., Bathmann, U., Rutgers van der Loeff, M., & Sildam, J. (1999). Low dissolved fe and the absence of diatom blooms in remote pacific waters of the southern ocean. *Marine Chemistry*, *66*(1), 1–34. https://doi.org/10.1016/S0304-4203(99)00022-5

Dever, M., Nicholson, D., Omand, M. M., & Mahadevan, A. (2021). Size-differentiated export flux in different dynamical regimes in the ocean. *Global Biogeochemical Cycles*, *35*(3), e2020GB006764. https://doi.org/https://doi.org/10.1029/2020GB006764

DeVries, T., Holzer, M., & Primeau, F. (2017). Recent increase in oceanic carbon uptake driven by weaker upper-ocean overturning. *Nature*, *542*(7640), 215–218. https://doi.org/10.1038/nature21068

Dong, S., Sprintall, J., Gille, S. T., & Talley, L. (2008). Southern ocean mixed-layer depth from argo float profiles. *Journal of Geophysical Research: Oceans*, *113*. https://doi.org/https://doi.org/10.1029/2006JC004051

Dove, L. A., Balwada, D., Thompson, A. F., & Gray, A. R. (2022). Enhanced ventilation in energetic regions of the antarctic circumpolar current. *Geophysical Research Letters*, *49*(13), e2021GL097574. https://doi.org/10.1029/2021GL097574

Dove, L. A., Thompson, A. F., Balwada, D., & Gray, A. R. (2021). Observational evidence of ventilation hotspots in the southern ocean. *Journal of Geophysical Research: Oceans*, *126*(7), e2021JC017178. https://doi.org/10.1029/2021JC017178

Dove, L. A., Viglione, G. A., Thompson, A. F., Flexas, M. M., Cason, T. R., & Sprintall, J. (2023). Controls on wintertime ventilation in southern drake passage. *Geophysical Research Letters*, *50*(5), e2022GL102550. https://doi.org/10.1029/2022GL102550

d'Ovidio, F., Fernández, V., Hernández-García, E., & López, C. (2004). Mixing structures in the mediterranean sea from finite-size lyapunov exponents. *Geophysical Research Letters*, *31*(17). https://doi.org/https://doi.org/10.1029/2004GL020328

d'Ovidio, F., Monte, S. D., Alvain, S., Dandonneau, Y., & Lévy, M. (2010). Fluid dynamical niches of phytoplankton types. *Proceedings of the National Academy of Sciences*, *107*(43), 18366–18370. https://doi.org/10.1073/pnas.1004620107

Drury, B. J., Siy, J. O., & Cheryan, S. (2011). When do female role models benefit women? the importance of differentiating recruitment from retention in STEM. *Psychological Inquiry*, *22*(4), 265–269. https://doi.org/10.1080/1047840X.2011.620935

Dufour, C. O., Griffies, S. M., de Souza, G. F., Frenger, I., Morrison, A. K., Palter, J. B., Sarmiento, J. L., Galbraith, E. D., Dunne, J. P., Anderson, W. G., & Slater, R. D. (2015). Role of mesoscale eddies in cross-frontal transport of heat and biogeochemical tracers in the southern ocean. *Journal of Physical Oceanography*, *45*(12), 3057–3081. https://doi.org/10.1175/JPO-D-14-0240.1

du Plessis, M. D., Swart, S., Ansorge, I. J., & Mahadevan, A. (2017). Submesoscale processes promote seasonal restratification in the subantarctic ocean. *Journal of Geophysical Research: Oceans*, *122*(4), 2960–2975. https://doi.org/10.1002/2016JC012494

du Plessis, M. D., Swart, S., Ansorge, I. J., Mahadevan, A., & Thompson, A. F. (2019). Southern ocean seasonal restratification delayed by submesoscale wind–front interactions. *Journal of Physical Oceanography*, *49*(4), 1035–1053. https://doi.org/10.1175/JPO-D-18-0136.1

Eriksen, C., Osse, T., Light, R., Wen, T., Lehman, T., Sabin, P., Ballard, J., & Chiodi, A. (2001). Seaglider: A long-range autonomous underwater vehicle for oceanographic research. *IEEE Journal of Oceanic Engineering*, *26*(4), 424–436. https://doi.org/10.1109/48.972073

Fay, A. R., Lovenduski, N. S., McKinley, G. A., Munro, D. R., Sweeney, C., Gray, A. R., Landschützer, P., Stephens, B. B., Takahashi, T., & Williams, N. (2018). Utilizing the drake passage time-series to understand variability and

change in subpolar southern ocean pCO_2. *Biogeosciences*, *15*(12), 3841–3855. https://doi.org/10.5194/bg-15-3841-2018

Ferrari, R., Jansen, M. F., Adkins, J. F., Burke, A., Stewart, A. L., & Thompson, A. F. (2014). Antarctic sea ice control on ocean circulation in present and glacial climates. *Proceedings of the National Academy of Sciences*, *111*(24), 8753–8758. https://doi.org/10.1073/pnas.1323922111

Ferrari, R., & Nikurashin, M. (2010). Suppression of eddy diffusivity across jets in the southern ocean. *Journal of Physical Oceanography*, *40*(7), 1501–1519. https://doi.org/10.1175/2010JPO4278.1

Firing, Y. L., Chereskin, T. K., & Mazloff, M. R. (2011). Vertical structure and transport of the antarctic circumpolar current in drake passage from direct velocity observations. *Journal of Geophysical Research: Oceans*, *116*. https://doi.org/10.1029/2011JC006999

Follows, M. J., Ito, T., & Dutkiewicz, S. (2006). On the solution of the carbonate chemistry system in ocean biogeochemistry models. *Ocean Modelling*, *12*(3), 290–301. https://doi.org/10.1016/j.ocemod.2005.05.004

Foppert, A., Donohue, K. A., & Watts, D. R. (2016). The polar front in drake passage: A composite-mean stream-coordinate view. *Journal of Geophysical Research: Oceans*, *121*(3), 1771–1788. https://doi.org/10.1002/2015JC011333

Freeman, N. M., & Lovenduski, N. S. (2016). Mapping the antarctic polar front: Weekly realizations from 2002 to 2014. *Earth System Science Data*, *8*(1), 191–198. https://doi.org/10.5194/essd-8-191-2016

Freeman, N. M., Lovenduski, N. S., Munro, D. R., Krumhardt, K. M., Lindsay, K., Long, M. C., & Maclennan, M. (2018). The variable and changing southern ocean silicate front: Insights from the CESM large ensemble. *Global Biogeochemical Cycles*, *32*(5), 752–768. https://doi.org/10.1029/2017GB005816

Freilich, M. A., & Mahadevan, A. (2019). Decomposition of vertical velocity for nutrient transport in the upper ocean [Publisher: American Meteorological Society]. *Journal of Physical Oceanography*, *49*(6), 1561–1575. https://doi.org/10.1175/JPO-D-19-0002.1

Freilich, M. A., & Mahadevan, A. (2021). Coherent pathways for subduction from the surface mixed layer at ocean fronts. *Journal of Geophysical Research: Oceans*, *126*(5), e2020JC017042. https://doi.org/10.1029/2020JC017042

Friedlingstein, P., O'Sullivan, M., Jones, M. W., Andrew, R. M., Gregor, L., Hauck, J., Le Quéré, C., Luijkx, I. T., Olsen, A., Peters, G. P., Peters, W., Pongratz, J., Schwingshackl, C., Sitch, S., Canadell, J. G., Ciais, P., Jackson, R. B., Alin, S. R., Alkama, R., ... Zheng, B. (2022). Global carbon budget 2022. *Earth System Science Data*, *14*(11), 4811–4900. https://doi.org/10.5194/essd-14-4811-2022

Frölicher, T. L., Sarmiento, J. L., Paynter, D. J., Dunne, J. P., Krasting, J. P., & Winton, M. (2015). Dominance of the southern ocean in anthropogenic carbon and heat uptake in CMIP5 models. *Journal of Climate*, *28*(2), 862–886. https://doi.org/10.1175/JCLI-D-14-00117.1

Giddy, I., Swart, S., du Plessis, M. D., Thompson, A. F., & Nicholson, S.-A. (2021). Stirring of sea-ice meltwater enhances submesoscale fronts in the southern ocean. *Journal of Geophysical Research: Oceans*, *126*(4), e2020JC016814. https://doi.org/https://doi.org/10.1029/2020JC016814

Gille, S. T., & Kelly, K. A. (1996). Scales of spatial and temporal variability in the southern ocean. *Journal of Geophysical Research: Oceans*, *101*, 8759–8773. https://doi.org/10.1029/96JC00203

Gille, S. T., Sheen, K. L., Swart, S., & Thompson, A. F. (2022, January 1). Chapter 12 - mixing in the southern ocean. In M. Meredith & A. C. Naveira Garabato (Eds.), *Ocean mixing* (pp. 301–327). Elsevier. Retrieved December 1, 2022, from https://www.sciencedirect.com/science/article/pii/B9780128215128000190

Gray, A. R., Johnson, K. S., Bushinsky, S. M., Riser, S. C., Russell, J. L., Talley, L. D., Wanninkhof, R., Williams, N. L., & Sarmiento, J. L. (2018). Autonomous biogeochemical floats detect significant carbon dioxide outgassing in the high-latitude southern ocean. *Geophysical Research Letters*, *45*(17), 9049–9057. https://doi.org/10.1029/2018GL078013

Gregor, L., Ryan-Keogh, T. J., Nicholson, S.-A., du Plessis, M. D., Giddy, I., & Swart, S. (2019). GliderTools: A python toolbox for processing underwater glider data. *Frontiers in Marine Science*, *6*. https://doi.org/10.3389/fmars.2019.00738

Group, S. S. F. N. R. I. (2017). The burden of invisible work in academia: Social inequalities and time use in five university departments. *Humboldt Journal of Social Relations*, *39*, 228–245. Retrieved April 14, 2023, from https://www.jstor.org/stable/90007882

Gruber, N., Gloor, M., Mikaloff Fletcher, S. E., Doney, S. C., Dutkiewicz, S., Follows, M. J., Gerber, M., Jacobson, A. R., Joos, F., Lindsay, K., Menemenlis, D., Mouchet, A., Müller, S. A., Sarmiento, J. L., & Takahashi, T. (2009). Oceanic sources, sinks, and transport of atmospheric CO2. *Global Biogeochemical Cycles*, *23*(1). https://doi.org/10.1029/2008GB003349

Gruber, N., Landschützer, P., & Lovenduski, N. S. (2019). The variable southern ocean carbon sink. *Annual Review of Marine Science*, *11*(1), 159–186. https://doi.org/10.1146/annurev-marine-121916-063407

Guarino, C. M., & Borden, V. M. H. (2017). Faculty service loads and gender: Are women taking care of the academic family? *Research in Higher Education*, *58*(6), 672–694. https://doi.org/10.1007/s11162-017-9454-2

Haëntjens, N., Boss, E., & Talley, L. D. (2017). Revisiting ocean color algorithms for chlorophyll a and particulate organic carbon in the southern ocean using biogeochemical floats. *Journal of Geophysical Research: Oceans*, *122*(8), 6583–6593. https://doi.org/https://doi.org/10.1002/2017JC012844

Harding-DeKam, J. L., Hamilton, B., & Loyd, S. (2012). The hidden curriculum of doctoral advising. *NACADA Journal*, *32*(2), 5–16. https://doi.org/10.12930/0271-9517-32.2.5

Haumann, F. A., Gruber, N., & Münnich, M. (2020). Sea-ice induced southern ocean subsurface warming and surface cooling in a warming climate. *AGU Advances*, *1*(2), e2019AV000132. https://doi.org/10.1029/2019AV000132

Hennon, T. D., Riser, S. C., & Mecking, S. (2016). Profiling float-based observations of net respiration beneath the mixed layer. *Global Biogeochemical Cycles*, *30*(6), 920–932. https://doi.org/10.1002/2016GB005380

Hersbach, H., Bell, B., Berrisford, P., Hirahara, S., Horányi, A., Muñoz-Sabater, J., Nicolas, J., Peubey, C., Radu, R., Schepers, D., Simmons, A., Soci, C., Abdalla, S., Abellan, X., Balsamo, G., Bechtold, P., Biavati, G., Bidlot, J., Bonavita, M., ... Thépaut, J.-N. (2020). The ERA5 global reanalysis. *Quarterly Journal of the Royal Meteorological Society*, *146*(730), 1999–2049. https://doi.org/10.1002/qj.3803

Heywood, K. J., Schmidtko, S., Heuzé, C., Kaiser, J., Jickells, T. D., Queste, B. Y., Stevens, D. P., Wadley, M., Thompson, A. F., Fielding, S., Guihen, D., Creed, E., Ridley, J. K., & Smith, W. (2014). Ocean processes at the antarctic continental slope. *Philosophical Transactions of the Royal Society A: Mathematical, Physical and Engineering Sciences*, *372*(2019), 20130047. https://doi.org/10.1098/rsta.2013.0047

Ito, T., Follows, M. J., & Boyle, E. A. (2004). Is AOU a good measure of respiration in the oceans? *Geophysical Research Letters*, *31*(17). https://doi.org/10.1029/2004GL020900

Jackett, D. R., & McDougall, T. J. (1997). A neutral density variable for the world's oceans. *Journal of Physical Oceanography*, *27*(2), 237–263. https://doi.org/10.1175/1520-0485(1997)027<0237:ANDVFT>2.0.CO;2

Jiang, C., Gille, S. T., Sprintall, J., & Sweeney, C. (2014). Drake passage oceanic pCO2: Evaluating CMIP5 coupled carbon–climate models using in situ observations. *Journal of Climate*, *27*(1), 76–100. https://doi.org/10.1175/JCLI-D-12-00571.1

Jimenez, M. F., Laverty, T. M., Bombaci, S. P., Wilkins, K., Bennett, D. E., & Pejchar, L. (2019). Underrepresented faculty play a disproportionate role in advancing diversity and inclusion. *Nature Ecology & Evolution*, *3*(7), 1030–1033. https://doi.org/10.1038/s41559-019-0911-5

Johnson, K. S., Coletti, L. J., Jannasch, H. W., Sakamoto, C. M., Swift, D. D., & Riser, S. C. (2013). Long-term nitrate measurements in the ocean using the in situ ultraviolet spectrophotometer: Sensor integration into the APEX profiling float. *Journal of Atmospheric and Oceanic Technology*, *30*(8), 1854–1866. https://doi.org/10.1175/JTECH-D-12-00221.1

Johnson, K. S., Jannasch, H. W., Coletti, L. J., Elrod, V. A., Martz, T. R., Takeshita, Y., Carlson, R. J., & Connery, J. G. (2016). Deep-sea DuraFET: A pressure tolerant pH sensor designed for global sensor networks. *Analytical Chemistry*, *88*(6), 3249–3256. https://doi.org/10.1021/acs.analchem.5b04653

Johnson, K. S., Plant, J. N., Coletti, L. J., Jannasch, H. W., Sakamoto, C. M., Riser, S. C., Swift, D. D., Williams, N. L., Boss, E., Haëntjens, N., Talley, L. D., & Sarmiento, J. L. (2017). Biogeochemical sensor performance in the SOCCOM profiling float array. *Journal of Geophysical Research: Oceans*, *122*(8), 6416–6436. https://doi.org/10.1002/2017JC012838

Johnson, K. S., Plant, J. N., Riser, S. C., & Gilbert, D. (2015). Air oxygen calibration of oxygen optodes on a profiling float array. *Journal of Atmospheric and Oceanic Technology*, *32*(11), 2160–2172. https://doi.org/10.1175/JTECH-D-15-0101.1

Jones, D. C., Ito, T., Takano, Y., & Hsu, W.-C. (2014). Spatial and seasonal variability of the air-sea equilibration timescale of carbon dioxide. *Global Biogeochemical Cycles*, *28*(11), 1163–1178. https://doi.org/10.1002/2014GB004813

Joyce, T. M., Zenk, W., & Toole, J. M. (1978). The anatomy of the antarctic polar front in the drake passage. *Journal of Geophysical Research: Oceans*, *83*, 6093–6113. https://doi.org/https://doi.org/10.1029/JC083iC12p06093

Kim, Y. S., & Orsi, A. H. (2014). On the variability of antarctic circumpolar current fronts inferred from 1992–2011 altimetry. *Journal of Physical Oceanography*, *44*(12), 3054–3071. https://doi.org/10.1175/JPO-D-13-0217.1

King, M. M., & Frederickson, M. E. (2021). The pandemic penalty: The gendered effects of COVID-19 on scientific productivity. *Socius*, *7*, 23780231211006977. https://doi.org/10.1177/23780231211006977

Klein, P., & Lapeyre, G. (2009). The oceanic vertical pump induced by mesoscale and submesoscale turbulence. *Annual Review of Marine Science*, *1*(1), 351–375. https://doi.org/10.1146/annurev.marine.010908.163704

Klocker, A. (2018). Opening the window to the southern ocean: The role of jet dynamics. *Science Advances*, *4*(10), eaao4719. https://doi.org/10.1126/sciadv.aao4719

Klocker, A., Ferrari, R., & LaCasce, J. H. (2012). Estimating suppression of eddy mixing by mean flows. *Journal of Physical Oceanography*, *42*(9), 1566–1576. https://doi.org/10.1175/JPO-D-11-0205.1

Kostadinov, T. S., Siegel, D. A., & Maritorena, S. (2009). Retrieval of the particle size distribution from satellite ocean color observations. *Journal of Geophysical Research: Oceans*, *114*. https://doi.org/10.1029/2009JC005303

Landschützer, P., Gruber, N., & Bakker, D. C. E. (2016). Decadal variations and trends of the global ocean carbon sink. *Global Biogeochemical Cycles*, *30*(10), 1396–1417. https://doi.org/https://doi.org/10.1002/2015GB005359

Landschützer, P., Gruber, N., Haumann, F. A., Rödenbeck, C., Bakker, D. C. E., Heuven, S. v., Hoppema, M., Metzl, N., Sweeney, C., Takahashi, T., Tilbrook, B., & Wanninkhof, R. (2015). The reinvigoration of the southern ocean carbon sink. *Science*, *349*(6253), 1221–1224. https://doi.org/10.1126/science.aab2620

Langlais, C., Lenton, A., Matear, R., Monselesan, D., Legresy, B., Cougnon, E., & Rintoul, S. R. (2017). Stationary rossby waves dominate subduction of anthropogenic carbon in the southern ocean. *Scientific Reports*, *7*(1), 17076. https://doi.org/10.1038/s41598-017-17292-3

Le Quéré, C., Rödenbeck, C., Buitenhuis, E. T., Conway, T. J., Langenfelds, R., Gomez, A., Labuschagne, C., Ramonet, M., Nakazawa, T., Metzl, N., Gillett, N., & Heimann, M. (2007). Saturation of the southern ocean CO2 sink due to recent climate change. *Science*. Retrieved September 8, 2021, from https://www.science.org/doi/abs/10.1126/science.1136188

Lévy, M., Ferrari, R., Franks, P. J. S., Martin, A. P., & Rivière, P. (2012). Bringing physics to life at the submesoscale. *Geophysical Research Letters*, *39*(14). https://doi.org/10.1029/2012GL052756

Lévy, M., Franks, P. J. S., & Smith, K. S. (2018). The role of submesoscale currents in structuring marine ecosystems. *Nature Communications*, *9*(1), 4758. https://doi.org/10.1038/s41467-018-07059-3

Lévy, M., Labeyrie, L. D., Karleskind, P., Resplandy, L., Éthé, C., & Pinsard, F. (2013). Physical pathways for carbon transfers between the surface mixed layer and the ocean interior. *Global Biogeochemical Cycles*, *27*(4), 1001–1012. https://doi.org/10.1002/gbc.20092

Llort, J., Langlais, C., Matear, R., Moreau, S., Lenton, A., & Strutton, P. G. (2018). Evaluating southern ocean carbon eddy-pump from biogeochemical-argo floats. *Journal of Geophysical Research: Oceans*, *123*(2), 971–984. https://doi.org/10.1002/2017JC012861

Loisel, H., Nicolas, J.-M., Sciandra, A., Stramski, D., & Poteau, A. (2006). Spectral dependency of optical backscattering by marine particles from satellite remote sensing of the global ocean. *Journal of Geophysical Research: Oceans*, *111*. https://doi.org/10.1029/2005JC003367

Long, M. C., Stephens, B. B., McKain, K., Sweeney, C., Keeling, R. F., Kort, E. A., Morgan, E. J., Bent, J. D., Chandra, N., Chevallier, F., Commane, R., Daube, B. C., Krummel, P. B., Loh, Z., Luijkx, I. T., Munro, D., Patra, P., Peters, W., Ramonet, M., ... Wofsy, S. C. (2021). Strong southern ocean carbon uptake evident in airborne observations. *Science*, *374*(6572), 1275–1280. https://doi.org/10.1126/science.abi4355

Lovenduski, N. S., Gruber, N., & Doney, S. C. (2008). Toward a mechanistic understanding of the decadal trends in the southern ocean carbon sink. *Global Biogeochemical Cycles*, *22*(3). https://doi.org/https://doi.org/10.1029/2007GB003139

Lu, J., & Speer, K. G. (2010). Topography, jets, and eddy mixing in the southern ocean. *Journal of Marine Research*, *68*(3), 479–502. https://doi.org/10.1357/002224010794657227

Lu, J., Wang, F., Liu, H., & Lin, P. (2016). Stationary mesoscale eddies, upgradient eddy fluxes, and the anisotropy of eddy diffusivity. *Geophysical Research Letters*, *43*(2), 743–751. https://doi.org/https://doi.org/10.1002/2015GL067384

MacCready, P., & Rhines, P. B. (2001). Meridional transport across a zonal channel: Topographic localization. *Journal of Physical Oceanography*, *31*(6), 1427–1439. https://doi.org/10.1175/1520-0485(2001)031<1427:MTAAZC>2.0.CO;2

Mahadevan, A. (2016). The impact of submesoscale physics on primary productivity of plankton. *Annual Review of Marine Science*, *8*(1), 161–184. https://doi.org/10.1146/annurev-marine-010814-015912

Mahadevan, A., Pascual, A., Rudnick, D. L., Ruiz, S., Tintoré, J., & D'Asaro, E. (2020). Coherent pathways for vertical transport from the surface ocean to interior. *Bulletin of the American Meteorological Society*, *101*(11), E1996–E2004. https://doi.org/10.1175/BAMS-D-19-0305.1

Mahadevan, A., & Tandon, A. (2006). An analysis of mechanisms for submesoscale vertical motion at ocean fronts. *Ocean Modelling*, *14*(3), 241–256. https://doi.org/10.1016/j.ocemod.2006.05.006

Marshall, J., & Speer, K. G. (2012). Closure of the meridional overturning circulation through southern ocean upwelling. *Nature Geoscience*, *5*(3), 171–180. https://doi.org/10.1038/ngeo1391

Mazloff, M. R., Cornuelle, B. D., Gille, S. T., & Verdy, A. (2018). Correlation lengths for estimating the large-scale carbon and heat content of the southern ocean. *Journal of Geophysical Research: Oceans*, *123*(2), 883–901. https://doi.org/https://doi.org/10.1002/2017JC013408

McDougall, T. J., & Barker, P. M. (2011). Getting started with TEOS-10 and the gibbs seawater (GSW) oceanographic toolbox. *SCOR/IAPSO WG*, *127*, 1–28.

McWilliams, J. C. (2016). Submesoscale currents in the ocean. *Proceedings of the Royal Society A: Mathematical, Physical and Engineering Sciences*, *472*(2189), 20160117. https://doi.org/10.1098/rspa.2016.0117

Meredith, M. P., Schofield, O., Newman, L., Urban, E., & Sparrow, M. (2013). The vision for a southern ocean observing system. *Current Opinion in Environmental Sustainability*, *5*(3), 306–313. https://doi.org/10.1016/j.cosust.2013.03.002

Meredith, M. P., Woodworth, P. L., Chereskin, T. K., Marshall, D. P., Allison, L. C., Bigg, G. R., Donohue, K., Heywood, K. J., Hughes, C. W., Hibbert, A., Hogg, A. M., Johnson, H. L., Jullion, L., King, B. A., Leach, H., Lenn, Y.-D., Morales Maqueda, M. A., Munday, D. R., Naveira Garabato, A. C., ... Sprintall, J. (2011). Sustained monitoring of the southern ocean at drake passage: Past achievements and future priorities. *Reviews of Geophysics*, *49*(4). https://doi.org/10.1029/2010RG000348

Montégut, C. d. B., Madec, G., Fischer, A. S., Lazar, A., & Iudicone, D. (2004). Mixed layer depth over the global ocean: An examination of profile data and a profile-based climatology. *Journal of Geophysical Research: Oceans*, *109*. https://doi.org/10.1029/2004JC002378

Monterey, G., & Levitus, S. (1997). Seasonal variability of mixed layer depth for the world ocean. *NOAA Atlas NESDIS 14*, 1–101.

Morrison, A. K., Waugh, D. W., Hogg, A. M., Jones, D. C., & Abernathey, R. P. (2022). Ventilation of the southern ocean pycnocline. *Annual Review of Marine Science*, *14*(1), null. https://doi.org/10.1146/annurev-marine-010419-011012

Naveira Garabato, A. C., Ferrari, R., & Polzin, K. L. (2011). Eddy stirring in the southern ocean. *Journal of Geophysical Research: Oceans*, *116*. https://doi.org/10.1029/2010JC006818

Naveira Garabato, A. C., Jullion, L., Stevens, D. P., Heywood, K. J., & King, B. A. (2009). Variability of subantarctic mode water and antarctic intermediate water in the drake passage during the late-twentieth and early-twenty-first centuries. *Journal of Climate*, *22*(13), 3661–3688. https://doi.org/10.1175/2009JCLI2621.1

Omand, M. M., D'Asaro, E. A., Lee, C. M., Perry, M. J., Briggs, N., Cetinić, I., & Mahadevan, A. (2015). Eddy-driven subduction exports particulate organic carbon from the spring bloom. *Science*, *348*(6231), 222–225. https://doi.org/10.1126/science.1260062

Orsi, A. H., Whitworth, T., & Nowlin, W. D. (1995). On the meridional extent and fronts of the antarctic circumpolar current. *Deep Sea Research Part I: Oceanographic Research Papers*, *42*(5), 641–673. https://doi.org/10.1016/0967-0637(95)00021-W

Palevsky, H. I., Quay, P. D., Lockwood, D. E., & Nicholson, D. P. (2016). The annual cycle of gross primary production, net community production, and export efficiency across the north pacific ocean. *Global Biogeochemical Cycles*, *30*(2), 361–380. https://doi.org/10.1002/2015GB005318

Pauthenet, E., Roquet, F., Madec, G., Guinet, C., Hindell, M., McMahon, C. R., Harcourt, R., & Nerini, D. (2018). Seasonal meandering of the polar front upstream of the kerguelen plateau. *Geophysical Research Letters*, *45*(18), 9774–9781. https://doi.org/10.1029/2018GL079614

Pellichero, V., Sallée, J.-B., Chapman, C. C., & Downes, S. M. (2018). The southern ocean meridional overturning in the sea-ice sector is driven by freshwater fluxes. *Nature Communications*, *9*(1), 1789. https://doi.org/10.1038/s41467-018-04101-2

Pellichero, V., Sallée, J.-B., Schmidtko, S., Roquet, F., & Charrassin, J.-B. (2017). The ocean mixed layer under southern ocean sea-ice: Seasonal cycle and forcing. *Journal of Geophysical Research: Oceans*, *122*(2), 1608–1633. https://doi.org/10.1002/2016JC011970

Peña, C., Ruedas-Gracia, N., Cohen, J. R., Tran, N., & Stratton, M. B. (2022). Ten simple rules for successfully supporting first-generation/low-income (FLI) students in STEM. *PLOS Computational Biology*, *18*(10), e1010499. https://doi.org/10.1371/journal.pcbi.1010499

Peters, W., Jacobson, A. R., Sweeney, C., Andrews, A. E., Conway, T. J., Masarie, K., Miller, J. B., Bruhwiler, L. M. P., Pétron, G., Hirsch, A. I., Worthy, D. E. J., van der Werf, G. R., Randerson, J. T., Wennberg, P. O., Krol, M. C., & Tans, P. P. (2007). An atmospheric perspective on north american carbon dioxide exchange: CarbonTracker. *Proceedings of the National Academy of Sciences*, *104*(48), 18925–18930. https://doi.org/10.1073/pnas.0708986104

Pollard, R. T., & Read, J. F. (2001). Circulation pathways and transports of the southern ocean in the vicinity of the southwest indian ridge. *Journal of Geophysical Research: Oceans*, *106*, 2881–2898. https://doi.org/https://doi.org/10.1029/2000JC900090

Posselt, J., Reyes, K. A., Slay, K. E., Kamimura, A., & Porter, K. B. (2017). Equity efforts as boundary work: How symbolic and social boundaries shape access and inclusion in graduate education. *Teachers College Record*, *119*(10), 1–38. https://doi.org/10.1177/016146811711901003

Prend, C. J., Gray, A. R., Talley, L. D., Gille, S. T., Haumann, F. A., Johnson, K. S., Riser, S. C., Rosso, I., Sauvé, J., & Sarmiento, J. L. (2022). Indo-pacific sector dominates southern ocean carbon outgassing. *Global Biogeochemical Cycles*, *36*(7), e2021GB007226. https://doi.org/10.1029/2021GB007226

Qu, L., Thomas, L. N., Wienkers, A. F., Hetland, R. D., Kobashi, D., Taylor, J. R., Hsu, F. H. W., MacKinnon, J. A., Shearman, R. K., & Nash, J. D. (2022). Rapid vertical exchange at fronts in the northern gulf of mexico. *Nature*

Communications, *13*(1), 5624. https://doi.org/10.1038/s41467-022-33251-7

Ranganathan, M., Lalk, E., Freese, L. M., Freilich, M. A., Wilcots, J., Duffy, M. L., & Shivamoggi, R. (2021). Trends in the representation of women among US geoscience faculty from 1999 to 2020: The long road toward gender parity. *AGU Advances*, *2*(3), e2021AV000436. https://doi.org/10.1029/2021AV000436

Reid, R. A. (2021). Retaining women faculty: The problem of invisible labor. *PS: Political Science & Politics*, *54*(3), 504–506. https://doi.org/10.1017/S1049096521000056

Rintoul, S. R. (2018). The global influence of localized dynamics in the southern ocean. *Nature*, *558*(7709), 209–218. https://doi.org/10.1038/s41586-018-0182-3

Rintoul, S. R., Meredith, M. P., Schofield, O., & Newman, L. (2012). The southern ocean observing system. *Oceanography*, *25*(3), 68–69. https://doi.org/10.5670/oceanog.2012.76

Rintoul, S. R., & Naveira Garabato, A. C. (2013). Chapter 18 - dynamics of the southern ocean circulation (G. Siedler, S. M. Griffies, J. Gould, & J. A. Church, Eds.). *103*, 471–492. https://doi.org/10.1016/B978-0-12-391851-2.00018-0

Riser, S. C., Freeland, H. J., Roemmich, D., Wijffels, S., Troisi, A., Belbéoch, M., Gilbert, D., Xu, J., Pouliquen, S., Thresher, A., Le Traon, P.-Y., Maze, G., Klein, B., Ravichandran, M., Grant, F., Poulain, P.-M., Suga, T., Lim, B., Sterl, A., ... Jayne, S. R. (2016). Fifteen years of ocean observations with the global argo array. *Nature Climate Change*, *6*(2), 145–153. https://doi.org/10.1038/nclimate2872

Riser, S. C., Swift, D., & Drucker, R. (2018). Profiling floats in SOCCOM: Technical capabilities for studying the southern ocean. *Journal of Geophysical Research: Oceans*, *123*(6), 4055–4073. https://doi.org/10.1002/2017JC013419

Roach, C. J., Balwada, D., & Speer, K. G. (2016). Horizontal mixing in the southern ocean from argo float trajectories. *Journal of Geophysical Research: Oceans*, *121*(8), 5570–5586. https://doi.org/https://doi.org/10.1002/2015JC011440

Roemmich, D., & Gilson, J. (2009). The 2004–2008 mean and annual cycle of temperature, salinity, and steric height in the global ocean from the argo program. *Progress in Oceanography*, *82*(2), 81–100. https://doi.org/10.1016/j.pocean.2009.03.004

Roemmich, D., Johnson, G. C., Riser, S., Davis, R., Gilson, J., Owens, W. B., Garzoli, S. L., Schmid, C., & Ignaszewski, M. (2009). The argo program: Observing the global ocean with profiling floats. *Oceanography*, *22*(2), 34–43. Retrieved August 31, 2021, from https://www.jstor.org/stable/24860957

Rosso, I., Hogg, A. M., Kiss, A. E., & Gayen, B. (2015). Topographic influence on submesoscale dynamics in the southern ocean. *Geophysical Research Letters*, *42*(4), 1139–1147. https://doi.org/10.1002/2014GL062720

Rosso, I., Hogg, A. M., Strutton, P. G., Kiss, A. E., Matear, R., Klocker, A., & van Sebille, E. (2014). Vertical transport in the ocean due to sub-mesoscale structures: Impacts in the kerguelen region. *Ocean Modelling*, *80*, 10–23. https://doi.org/10.1016/j.ocemod.2014.05.001

Rousseaux, C. S., & Gregg, W. W. (2014). Interannual variation in phytoplankton primary production at a global scale. *Remote Sensing*, *6*(1), 1–19. https://doi.org/10.3390/rs6010001

Rudnick, D. L., & Cole, S. T. (2011). On sampling the ocean using underwater gliders. *Journal of Geophysical Research: Oceans*, *116*. https://doi.org/10.1029/2010JC006849

Rudnick, D. L., Davis, R. E., Eriksen, C. C., Fratantoni, D. M., & Perry, M. J. (2004). Underwater gliders for ocean research. *Marine Technology Society Journal*, *38*(2), 73–84. https://doi.org/10.4031/002533204787522703

Ruiz, S., Claret, M., Pascual, A., Olita, A., Troupin, C., Capet, A., Tovar-Sánchez, A., Allen, J., Poulain, P.-M., Tintoré, J., & Mahadevan, A. (2019). Effects of oceanic mesoscale and submesoscale frontal processes on the vertical transport of phytoplankton. *Journal of Geophysical Research: Oceans*, *124*(8), 5999–6014. https://doi.org/10.1029/2019JC015034

Ruiz, S., Pascual, A., Garau, B., Pujol, I., & Tintoré, J. (2009). Vertical motion in the upper ocean from glider and altimetry data. *Geophysical Research Letters*, *36*(14). https://doi.org/10.1029/2009GL038569

Sallée, J.-B., Matear, R. J., Rintoul, S. R., & Lenton, A. (2012). Localized subduction of anthropogenic carbon dioxide in the southern hemisphere oceans. *Nature Geoscience*, *5*(8), 579–584. https://doi.org/10.1038/ngeo1523

Sallée, J.-B., Speer, K. G., Rintoul, S. R., & Wijffels, S. (2010). Southern ocean thermocline ventilation. *Journal of Physical Oceanography*, *40*(3), 509–529. https://doi.org/10.1175/2009JPO4291.1

Sarmiento, J. L., Gruber, N., Brzezinski, M. A., & Dunne, J. P. (2004). High-latitude controls of thermocline nutrients and low latitude biological productivity. *Nature*, *427*(6969), 56–60. https://doi.org/10.1038/nature02127

Schlitzer, R. (2002). Carbon export fluxes in the southern ocean: Results from inverse modeling and comparison with satellite-based estimates. *Deep Sea Research Part II: Topical Studies in Oceanography*, *49*(9), 1623–1644. https://doi.org/10.1016/S0967-0645(02)00004-8

Sejr, M., Krause-Jensen, D., Rysgaard, S., Sørensen, L., Christensen, P., & Glud, R. (2011). Air—sea flux of CO2 in arctic coastal waters influenced by glacial melt water and sea ice. *Tellus B: Chemical and Physical Meteorology*, *63*(5), 815–822. https://doi.org/10.1111/j.1600-0889.2011.00540.x

Shadwick, E. H., Trull, T. W., Tilbrook, B., Sutton, A. J., Schulz, E., & Sabine, C. L. (2015). Seasonality of biological and physical controls on surface ocean CO2 from hourly observations at the southern ocean time series site south of australia. *Global Biogeochemical Cycles*, *29*(2), 223–238. https://doi.org/10.1002/2014GB004906

Siegel, D. A., DeVries, T., Cetinić, I., & Bisson, K. M. (2023). Quantifying the ocean's biological pump and its carbon cycle impacts on global scales. *Annual Review of Marine Science*, *15*(1), null. https://doi.org/10.1146/annurev-marine-040722-115226

Siegelman, L. (2020). Energetic submesoscale dynamics in the ocean interior. *Journal of Physical Oceanography*, *50*(3), 727–749. https://doi.org/10.1175/JPO-D-19-0253.1

Siegelman, L., Klein, P., Rivière, P., Thompson, A. F., Torres, H. S., Flexas, M., & Menemenlis, D. (2020). Enhanced upward heat transport at deep submesoscale ocean fronts. *Nature Geoscience*, *13*(1), 50–55. https://doi.org/10.1038/s41561-019-0489-1

Siegelman, L., O'Toole, M., Flexas, M., Rivière, P., & Klein, P. (2019). Submesoscale ocean fronts act as biological hotspot for southern elephant seal. *Scientific Reports*, *9*(1), 1–13. https://doi.org/10.1038/s41598-019-42117-w

Simoes-Sousa, I. T., Tandon, A., Pereira, F., Lazaneo, C. Z., & Mahadevan, A. (2022). Mixed layer eddies supply nutrients to enhance the spring phytoplankton bloom. *Frontiers in Marine Science*, *9*. https://doi.org/10.3389/fmars.2022.825027

Smith, K. S., & Ferrari, R. (2009). The production and dissipation of compensated thermohaline variance by mesoscale stirring. *Journal of Physical Oceanography*, *39*(10), 2477–2501. https://doi.org/10.1175/2009JPO4103.1

Sokolov, S., & Rintoul, S. R. (2007). Multiple jets of the antarctic circumpolar current south of australia. *Journal of Physical Oceanography*, *37*(5), 1394–1412. https://doi.org/10.1175/JPO3111.1

Sokolov, S., & Rintoul, S. R. (2009). Circumpolar structure and distribution of the antarctic circumpolar current fronts: 1. mean circumpolar paths. *Journal of Geophysical Research: Oceans*, *114*. https://doi.org/https://doi.org/10.1029/2008JC005108

Speer, K. G., Guilyardi, E., & Madec, G. (2000). Southern ocean transformation in a coupled model with and without eddy mass fluxes. *Tellus A*, *52*(5), 554–565. https://doi.org/10.1034/j.1600-0870.2000.01060.x

Sprintall, J. (2003). Seasonal to interannual upper-ocean variability in the drake passage. *Journal of Marine Research*, *61*(1), 27–57. https://doi.org/10.1357/002224003321586408

Sprintall, J. (2008). Long-term trends and interannual variability of temperature in drake passage. *Progress in Oceanography*, *77*(4), 316–330. https://doi.org/10.1016/j.pocean.2006.06.004

Stephenson Jr., G. R., Gille, S. T., & Sprintall, J. (2012). Seasonal variability of upper ocean heat content in drake passage. *Journal of Geophysical Research: Oceans*, *117*. https://doi.org/10.1029/2011JC007772

Stewart, K. D., & Haine, T. W. N. (2016). Thermobaricity in the transition zones between alpha and beta oceans. *Journal of Physical Oceanography*, *46*(6), 1805–1821. https://doi.org/10.1175/JPO-D-16-0017.1

Stukel, M. R., Aluwihare, L. I., Barbeau, K. A., Chekalyuk, A. M., Goericke, R., Miller, A. J., Ohman, M. D., Ruacho, A., Song, H., Stephens, B. M., & Landry, M. R. (2017). Mesoscale ocean fronts enhance carbon export due to gravitational sinking and subduction. *Proceedings of the National Academy of Sciences*, *114*(6), 1252–1257. https://doi.org/10.1073/pnas.1609435114

Stukel, M. R., & Ducklow, H. W. (2017). Stirring up the biological pump: Vertical mixing and carbon export in the southern ocean [Publisher: John Wiley & Sons, Ltd]. *Global Biogeochemical Cycles*, *31*(9), 1420–1434. https://doi.org/10.1002/2017GB005652

Su, Z., Torres, H., Klein, P., Thompson, A. F., Siegelman, L., Wang, J., Menemenlis, D., & Hill, C. (2020). High-frequency submesoscale motions enhance the upward vertical heat transport in the global ocean. *Journal of Geophysical Research: Oceans*, *125*(9), e2020JC016544. https://doi.org/10.1029/2020JC016544

Su, Z., Wang, J., Klein, P., Thompson, A. F., & Menemenlis, D. (2018). Ocean submesoscales as a key component of the global heat budget. *Nature Communications*, *9*(1), 775. https://doi.org/10.1038/s41467-018-02983-w

Sutton, A. J., Williams, N. L., & Tilbrook, B. (2021). Constraining southern ocean CO2 flux uncertainty using uncrewed surface vehicle observations. *Geophysical Research Letters*, *48*(3), e2020GL091748. https://doi.org/https://doi.org/10.1029/2020GL091748

Swart, S., du Plessis, M. D., Thompson, A. F., Biddle, L. C., Giddy, I., Linders, T., Mohrmann, M., & Nicholson, S.-A. (2020). Submesoscale fronts in the antarctic marginal ice zone and their response to wind forcing. *Geophysical Research Letters*, *47*(6), e2019GL086649. https://doi.org/https://doi.org/10.1029/2019GL086649

Takahashi, T., Sutherland, S. C., Wanninkhof, R., Sweeney, C., Feely, R. A., Chipman, D. W., Hales, B., Friederich, G., Chavez, F., Sabine, C., Watson, A., Bakker, D. C. E., Schuster, U., Metzl, N., Yoshikawa-Inoue, H., Ishii, M., Midorikawa, T., Nojiri, Y., Körtzinger, A., . . . de Baar, H. J. W. (2009). Climatological mean and decadal change in surface ocean pCO2, and net sea–air CO2 flux over the global oceans. *Deep Sea Research Part II: Topical Studies in Oceanography*, *56*(8), 554–577. https://doi.org/10.1016/j.dsr2.2008.12.009

Takahashi, T., Sweeney, C., Hales, B., Chipman, D. W., Newberger, T., Goddard, J. G., Iannuzzi, R. A., & Sutherland, S. C. (2012). The changing carbon cycle in the southern ocean. *Oceanography*, *25*(3), 26–37. https://doi.org/10.5670/oceanog.2012.71

Talley, L. D. (2013). Closure of the global overturning circulation through the indian, pacific, and southern oceans: Schematics and transports. *Oceanography*, *26*(1), 80–97. https://doi.org/10.5670/oceanog.2013.07

Tamsitt, V., Drake, H. F., Morrison, A. K., Talley, L. D., Dufour, C. O., Gray, A. R., Griffies, S. M., Mazloff, M. R., Sarmiento, J. L., Wang, J., & Weijer, W. (2017). Spiraling pathways of global deep waters to the surface of the southern ocean. *Nature Communications*, *8*(1), 1–10. https://doi.org/10.1038/s41467-017-00197-0

Tamsitt, V., Talley, L. D., Mazloff, M. R., & Cerovečki, I. (2016). Zonal variations in the southern ocean heat budget. *Journal of Climate*, *29*(18), 6563–6579. https://doi.org/10.1175/JCLI-D-15-0630.1

Taylor, J. R. (2018). Accumulation and subduction of buoyant material at submesoscale fronts. *Journal of Physical Oceanography*, *48*(6), 1233–1241. https://doi.org/10.1175/JPO-D-17-0269.1

Taylor, J. R., & Thompson, A. F. (2023). Submesoscale dynamics in the upper ocean. *Annual Review of Fluid Mechanics*, *55*(1), null. https://doi.org/10.1146/annurev-fluid-031422-095147

Tengberg, A., Hovdenes, J., Andersson, H. J., Brocandel, O., Diaz, R., Hebert, D., Arnerich, T., Huber, C., Körtzinger, A., Khripounoff, A., Rey, F., Rönning, C., Schimanski, J., Sommer, S., & Stangelmayer, A. (2006). Evaluation of a lifetime-based optode to measure oxygen in aquatic systems. *Limnology and Oceanography: Methods*, *4*(2), 7–17. https://doi.org/https://doi.org/10.4319/lom.2006.4.7

Thomas, L. N., & Lee, C. M. (2005). Intensification of ocean fronts by downfront winds. *Journal of Physical Oceanography*, *35*(6), 1086–1102. https://doi.org/10.1175/JPO2737.1

Thomas, L. N., Tandon, A., & Mahadevan, A. (2008). Submesoscale processes and dynamics. *Washington DC American Geophysical Union Geophysical Monograph Series*, *177*, 17–38. https://doi.org/10.1029/177GM04

Thompson, A. F., Lazar, A., Buckingham, C., Naveira Garabato, A. C., Damerell, G. M., & Heywood, K. J. (2016). Open-ocean submesoscale motions: A full seasonal cycle of mixed layer instabilities from gliders. *Journal of Physical Oceanography*, *46*(4), 1285–1307. https://doi.org/10.1175/JPO-D-15-0170.1

Thompson, A. F., & Naveira Garabato, A. C. (2014). Equilibration of the antarctic circumpolar current by standing meanders. *Journal of Physical Oceanography*, *44*(7), 1811–1828. https://doi.org/10.1175/JPO-D-13-0163.1

Thompson, A. F., & Sallée, J.-B. (2012). Jets and topography: Jet transitions and the impact on transport in the antarctic circumpolar current. *Journal of Physical Oceanography*, *42*(6), 956–972. https://doi.org/10.1175/JPO-D-11-0135.1

Trull, T. W., Jansen, P., Schulz, E., Weeding, B., Davies, D. M., & Bray, S. G. (2019). Autonomous multi-trophic observations of productivity and export at the australian southern ocean time series (SOTS) reveal sequential mechanisms of physical-biological coupling. *Frontiers in Marine Science*, *6*. https://doi.org/10.3389/fmars.2019.00525

Uchida, T., Balwada, D., Abernathey, R. P., McKinley, G., Smith, S., & Lévy, M. (2019). The contribution of submesoscale over mesoscale eddy iron transport in the open southern ocean. *Journal of Advances in Modeling Earth Systems*, *11*(12), 3934–3958. https://doi.org/10.1029/2019MS001805

Uchida, T., Balwada, D., P. Abernathey, R. P., A. McKinley, G., K. Smith, S., & Lévy, M. (2020). Vertical eddy iron fluxes support primary production in the open southern ocean. *Nature Communications*, *11*(1), 1125. https://doi.org/10.1038/s41467-020-14955-0

Vaillancourt, R. D., Brown, C. W., Guillard, R. R. L., & Balch, W. M. (2004). Light backscattering properties of marine phytoplankton: Relationships to cell size, chemical composition and taxonomy. *Journal of Plankton Research*, *26*(2), 191–212. https://doi.org/10.1093/plankt/fbh012

Verdy, A., & Mazloff, M. R. (2017). A data assimilating model for estimating southern ocean biogeochemistry. *Journal of Geophysical Research: Oceans*, *122*(9), 6968–6988. https://doi.org/10.1002/2016JC012650

Viglione, G. A., & Thompson, A. F. (2016). Lagrangian pathways of upwelling in the southern ocean. *Journal of Geophysical Research: Oceans*, *121*(8), 6295–6309. https://doi.org/https://doi.org/10.1002/2016JC011773

Viglione, G. A., Thompson, A. F., Flexas, M. M., Sprintall, J., & Swart, S. (2018). Abrupt transitions in submesoscale structure in southern drake passage: Glider observations and model results. *Journal of Physical Oceanography*, *48*(9), 2011–2027. https://doi.org/10.1175/JPO-D-17-0192.1

Villermaux, E. (2019). Mixing versus stirring. *Annual Review of Fluid Mechanics*, *51*(1), 245–273. https://doi.org/10.1146/annurev-fluid-010518-040306

Wanninkhof, R. (1992). Relationship between wind speed and gas exchange over the ocean. *Journal of Geophysical Research: Oceans*, *97*, 7373–7382. https://doi.org/10.1029/92JC00188

Wei, Y., Gille, S. T., Mazloff, M. R., Tamsitt, V., Swart, S., Chen, D., & Newman, L. (2020). Optimizing mooring placement to constrain southern ocean air–sea fluxes. *Journal of Atmospheric and Oceanic Technology*, *37*(8), 1365–1385. https://doi.org/10.1175/JTECH-D-19-0203.1

Witter, D. L., & Chelton, D. B. (1998). Eddy–mean flow interaction in zonal oceanic jet flow along zonal ridge topography. *Journal of Physical Oceanography*, *28*(10), 2019–2039. https://doi.org/10.1175/1520-0485(1998)028<2019:EMFIIZ>2.0.CO;2

Youngs, M. K., Thompson, A. F., Lazar, A., & Richards, K. J. (2017). ACC meanders, energy transfer, and mixed barotropic–baroclinic instability. *Journal of Physical Oceanography*, *47*(6), 1291–1305. https://doi.org/10.1175/JPO-D-16-0160.1

Yung, C. K., Morrison, A. K., & Hogg, A. M. (2022). Topographic hotspots of southern ocean eddy upwelling. *Frontiers in Marine Science*, *9*. https://doi.org/10.3389/fmars.2022.855785

Zhang, X., Hu, L., & He, M.-X. (2009). Scattering by pure seawater: Effect of salinity. *Optics Express*, *17*(7), 5698–5710. https://doi.org/10.1364/OE.17.005698

Zhang, Y., Chambers, D., & Liang, X. (2021). Regional trends in southern ocean eddy kinetic energy. *Journal of Geophysical Research: Oceans*, *126*(6), e2020JC016973. https://doi.org/10.1029/2020JC016973